VOLUME 37 JUNE 1959 NUMBER 6

Canadian Journal of Physics

Editor: H. E. DUCKWORTH

Associate Editors:

L. G. ELLIOTT, *Atomic Energy of Canada, Ltd., Chalk River*
J. S. FOSTER, *McGill University*
G. HERZBERG, *National Research Council of Canada*
L. LEPRINCE-RINGUET, *Ecole Polytechnique, Paris*
B. W. SARGENT, *Queen's University*
G. M. VOLKOFF, *University of British Columbia*
W. H. WATSON, *University of Toronto*
G. A. WOONTON, *McGill University*

Published by THE NATIONAL RESEARCH COUNCIL

OTTAWA CANADA

CANADIAN JOURNAL OF PHYSICS

Under the authority of the Chairman of the Committee of the Privy Council on Scientific and Industrial Research, the National Research Council issues THE CANADIAN JOURNAL OF PHYSICS and five other journals devoted to the publication, in English or French, of the results of original scientific research. Matters of general policy concerning these journals are the responsibility of a joint Editorial Board consisting of: members representing the National Research Council of Canada; the Editors of the Journals; and members representing the Royal Society of Canada and four other scientific societies.

EDITORIAL BOARD

Representatives of the National Research Council

I. McT. Cowan, *University of British Columbia*
A. Gauthier, *University of Montreal*
H. G. Thode (Chairman), *McMaster University*
D. L. Thomson, *McGill University*

Editors of the Journals

D. L. Bailey, *University of Toronto*
T. W. M. Cameron, *Macdonald College*
H. E. Duckworth, *McMaster University*
K. A. C. Elliott, *Montreal Neurological Institute*
Léo Marion, *National Research Council*
R. G. E. Murray, *University of Western Ontario*

Representatives of Societies

D. L. Bailey, *University of Toronto*
Royal Society of Canada
T. W. M. Cameron, *Macdonald College*
Royal Society of Canada
H. E. Duckworth, *McMaster University*
Royal Society of Canada
Canadian Association of Physicists
K. A. C. Elliott, *Montreal Neurological Institute*
Canadian Physiological Society
P. R. Gendron, *University of Ottawa*
Chemical Institute of Canada
R. G. E. Murray, *University of Western Ontario*
Canadian Society of Microbiologists
T. Thorvaldson, *University of Saskatchewan*
Royal Society of Canada

Ex officio

Léo Marion (Editor-in-Chief), *National Research Council*
J. B. Marshall (Administration and Awards), *National Research Council*

Manuscripts for publication should be submitted to Dr. H. E. Duckworth, Editor, Canadian Journal of Physics, Hamilton College, McMaster University, Hamilton, Ontario.
For instructions on preparation of copy, see **NOTES TO CONTRIBUTORS** (back cover).

Proof, correspondence concerning proof, and orders for reprints should be sent to the Manager, Editorial Office (Research Journals), Division of Administration and Awards, National Research Council, Ottawa 2, Canada.

Subscriptions, renewals, requests for single or back numbers, and all remittances should be sent to Division of Administration and Awards, National Research Council, Ottawa 2, Canada. Remittances should be made payable to the Receiver General of Canada, credit National Research Council.

The journals published, frequency of publication, and prices are:

Canadian Journal of Biochemistry and Physiology	Monthly	$9.00 a year
Canadian Journal of Botany	Bimonthly	$6.00 a year
Canadian Journal of Chemistry	Monthly	$12.00 a year
Canadian Journal of Microbiology	Bimonthly	$6.00 a year
Canadian Journal of Physics	Monthly	$9.00 a year
Canadian Journal of Zoology	Bimonthly	$5.00 a year

The price of regular single numbers of all journals is $2.00.

Canadian Journal of Physics

Issued by THE NATIONAL RESEARCH COUNCIL OF CANADA

VOLUME 37 JUNE 1959 NUMBER 6

MEASUREMENTS WITH A WHOLE BODY COUNTER[1]

K. G. MCNEILL AND R. M. GREEN

ABSTRACT

An account is given of work on the measurement of the gamma radioactivity of humans. A steel room has been constructed, in which this gamma activity may be measured to a statistical accuracy of a few per cent in 30 minutes using a 5-in. NaI crystal as detector. The average potassium content of thirty 19-year-old males living in Ontario has been found to be 0.21$_2$% of body weight, and the average Cs/K ratio 51 $\mu\mu$c/g K.

INTRODUCTION

The increase in radioactivity of the world due to nuclear weapon tests, the subsequent ingestion of this activity by humans, and its possible effects on human health have in recent years increased the interest in measurements of the current radioactivity of the body and other biological material (Burch and Spiers 1953; Reines *et al.* 1953; Mayneord *et al.* 1958).

The gamma activity of the normal human body is largely due to K^{40}, a naturally occurring isotope of potassium, and to Cs^{137} from nuclear fallout; 1.46-Mev gamma rays are emitted in 11% of the K^{40} disintegrations, and the potassium of a typical adult emits 500 gamma rays of this energy per second. Cs^{137} decays to Ba^{137} with a half-life of 27 years; 92% of these disintegrations are to the isomeric state of Ba^{137} which quickly (2.6 minutes) de-excites with emission of a 0.66-Mev gamma ray. At the present time the gamma activity from this source is of the same order as that from K^{40} in the body.

Extensive measurements of gamma activity from the body have been made by the Argonne National Laboratories group (e.g. Miller and Marinelli 1956), at other places in the United States (e.g. Anderson *et al.* 1957) and in Britain (Burch and Spiers 1953), but so far no extensive investigation has been reported on similar work in Canada. Results for different latitudes are, however, of value owing to the geographical variation of fallout (Libby 1958). At the University of Toronto apparatus has been built which enables the gamma activity of a person to be determined in a relatively short time. The purpose of this paper is to report on this measurement equipment and to give some of the results so far obtained on the activity of persons in Ontario.

[1]Manuscript received February 25, 1959.
Contribution from the Department of Physics, University of Toronto, Toronto, Ontario.

THE DETECTION APPARATUS

In order to measure the low level of activity from the body it is necessary to reduce other sources of radiation to as great an extent as possible, for otherwise background from cosmic rays, local gamma emitters, and airborne contamination will swamp the body activity. For example, using a 5-in. NaI crystal the maximum count in the photopeak of the K^{40} spectrum of a normal subject in our standard geometry is only 1/20th of the 1.46-Mev background count with no shielding. In the building of radiation shielding, we have followed very closely the work and designs of the Argonne National Laboratories group (Miller *et al.* 1956). A steel room has been constructed with internal dimensions 5 ft×6 ft×7 ft 4 in., and with 8 in. thick walls, floor, and ceiling. The total weight of the room is 50 tons. For convenience in handling during construction, the steel used is in the form of $\frac{1}{4}$-in. thick plates, which have dimensions ranging from 10 in. to 24 in. wide and from 4 ft 6 in. to 8 ft 9 in. long. The skeleton of the room is of steel girders and angle iron. The door, which weighs 3 tons, has such a width that when open a space of 17 inches is available for entrance into the room.

For detecting gamma radiation, sodium iodide crystals are used. During the initial stages of background measurements a $1\frac{3}{4}$-in. diameter × 2-in. crystal was employed, but when the background had been sufficiently attenuated by the increase in the thickness of the steel walls, a change was made to a 5-in. diameter × 4-in. crystal. The latter was made from especially potassium free iodide, and was mounted in an electrolytic copper can. The normal glass window was replaced by a quartz one. These changes, made by the Harshaw Chemical Company, served to reduce the inherent radioactivity of the crystal assembly. Du Mont 6292 and 6364 photomultiplier tubes are used, and the pulses from these fed by conventional electronics to a Radiation Instrument Development Laboratories 100-channel pulse height analyzer, model 3300.

For body activity measurements, subjects are seated in a reclining chair made of angle iron and canvas webbing, which was found to have no appreciable activity. The crystal is hung above the subject's abdomen in a standard position with respect to the chair, following the results of experiments made by the Argonne group (Miller 1956).

The whole steel room is enveloped in a plastic bag to help to exclude dust-borne activity. Filtered air is blown into the room from the main laboratory, the air of which is itself conditioned and filtered.

BACKGROUND MEASUREMENTS

In order that information could be obtained on the attenuation of the background by the steel walls of the counting room, measurements were taken with the 2-in. crystal, and, latterly, with the 5-in. crystal, as the wall thickness was increased. One such measurement was taken for every 1 inch of steel added to the walls. The results are illustrated in Table I. It was found that although the attenuation was approximately exponential for the first few inches, the addition of the seventh and eighth inches of steel made

only a small difference to the background count. This is because at this thickness the main contributions to the background are from sources in the crystal assembly and shielding itself.

TABLE I

Attenuation ratios

Inches of steel	No. of counts/minute in 2-in. NaI corresponding to:		University of Toronto attenuation ratio	
	$E_\gamma > 0.2$ Mev	$E_\gamma > 0.51$ Mev	$E_\gamma > 0.2$ Mev	$E_\gamma > 0.51$ Mev
0	2,980	952	1.0	1.0
1		454		0.48
2		234		0.25
3	286	130	0.096	0.137
4	169	76	0.057	0.080
5	114	58	0.038	0.061
6	86	47	0.029	0.049
7	82	45	0.028	0.047
8	81	45	0.027	0.046

Peaks in the background spectrum obtained with no steel shielding may all be ascribed to gamma rays from RaC, except for the K^{40} peak at 1.46 Mev. With maximum shielding, the most obvious peak is at 1.46 Mev, but there are also peaks at 0.72 Mev and at about 0.5 Mev. This latter peak was found in the gamma spectra of samples of steel, and is due to the fission products Ru^{106} and Ru^{103}. This element is siderophilic (Beamish 1958) and it is presumably fission product ruthenium in the shielding steel that is the cause of the 0.5-Mev peak. The peak at 0.72 Mev is ascribed to the fission products Zr^{95}–Nb^{95} present in dust. As was expected (Miller and Steingraber 1957), a subsidiary experiment showed that three-quarters of the residual K^{40} activity comes from the potassium in the glass of the photomultiplier.

With the 8-in. steel shielding, the total background in the energy range 200 kev $\rightarrow$ 2.0 Mev is 470 c.p.m., and in the range 1 $\rightarrow$ 2 Mev is 66 c.p.m.

CALIBRATION OF THE APPARATUS

The primary purpose of the apparatus is to measure the gamma radioactivity of the human body. In order that a particular count in the detector might be related to a definite amount of radioactivity in the body, it was necessary to calibrate the apparatus using known amounts of radioactive substance. The isotope K^{42} was used for this work, for not only will it be distributed in the body with the normal potassium content, but also it emits a gamma line of 1.53 Mev, very similar in energy to that from K^{40}.

Solutions of $K^{42}Cl$ containing standard activities were obtained from Abbott Pharmaceuticals of Oak Ridge. These were administered orally to five subjects who had weights varying from 134 to 200 lb, and the apparent activity of these subjects was followed for 2 days. At the end of this time it is to be expected (Rapoport 1959) that, to a sufficiently high degree of accuracy, the K^{42} will be distributed throughout the body. This expectation was confirmed

by the fact that the K^{42} count, after correction for radioactive decay and biological elimination, remained approximately constant after 24 hours.

Two methods of calibrating the detectors were used. The first method used a known mass of ordinary KCl as the standard of radioactivity. Measurements were made with equal activities of $K^{42}Cl$ in the five subjects and in water solution in a vessel at a standard distance from the crystal. Then measurements were made with ordinary KCl solution in the same jar at the standard distance. Intercomparison of these three measurements with the activity due to normal K in the body gives the mass of ordinary K in the body. Corrections had to be made for biological excretion of K^{42}, measured to be 1% every 10 hours, and for the different self-absorptions of the dilute $K^{42}Cl$ solution and for the concentrated ordinary KCl solution. This latter correction was found experimentally by the use of solutions of different strength. Measurements were taken of the count obtained from solutions containing 750 g, 500 g, and 250 g of KCl dissolved in water to give in each case 4 liters of solution. From the results an extrapolation was made to infinite dilution. It was found, for example, that with the 750-g sample, the self-absorption correction was 5%. Confidence in the experimental extrapolation was reinforced by the good agreement with theoretical calculations of the expected correction.

The second method made use of the Abbott Pharmaceutical standardization of the K^{42}. Knowing the amount of K^{42} in the body at any time (after nuclear decay and biological excretion correction), and the corresponding K^{42} photopeak count, the value of A in the relationship count $= A \times$ activity can be found. A is mainly a geometric term with corrections which are functions of photon energy, the variations of which with energy may be found by subsidiary experiments with different sources. This method, however, depends on a knowledge of the decay schemes of both K^{42} and K^{40}, and in both cases the percentage of disintegrations which lead to gamma emission is not absolutely known. Strominger, Hollander, and Seaborg (1958) quote a figure of 18% for the fraction of K^{42} disintegrations that give 1.53-Mev gamma rays. Using values quoted by these same reviewers, the post-1954 figures for the specific beta activity of normal K give an average of 28.6 β/sec g, and the average of post-1947 results on the γ/β ratio is 0.12. In our calculations, we have accepted an average figure of 3.43 γ/sec g K. In addition to decay scheme uncertainties, the final result using this method involves the calibration errors of the K^{42} ($\pm 4\%$).

In fact the calculated results based on the two methods only differed by 4%, which is within the accuracy of the experiments, and as a result in all subsequent calculations the average of the two methods was used.

RESULTS

The spectra of 30 male first-year premedical students (average weight 158 lb) at the University of Toronto were measured, and a typical graph of the spectrum of one of them is shown in Fig. 1. The spectrum shows peaks at 1.46 Mev and 0.66 Mev, corresponding to K^{40} and Cs^{137} respectively. This

spectrum is the result of 30 minutes running time on the student, with the subtraction of 30 minutes background. Typically such a run gave a count in the K^{40} photopeak of 1200 counts, after the subtraction of a background of 780 counts. The statistical error on any individual count is 4%.

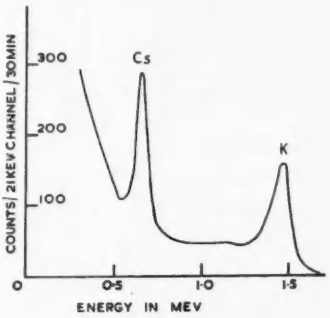

FIG. 1. The spectrum of a subject with no radioactive history; 30-minute run minus background. This subject is calculated to have a body content of 141 g of K and a Cs/K ratio of 50 $\mu\mu$c/g K.

In none of the 30 subjects was there evidence for any appreciable activity other than that due to K^{40} and Cs^{137}.

Using the calibration obtained as outlined above, the K contents of the students were obtained. The average figure obtained is that $(0.21_2 \pm 0.013)\%$ of the body weight is potassium, the error being based on uncertainties in calibration, geometric errors, etc. As expected, the individual potassium body contents show a biological variation, the graph of (number of subjects with a given K percentage) vs. (K percentage) being a Gaussian whose mean is 0.21_2 and whose standard deviation is 0.023, both figures being percentages by weight of potassium in the body.

Consideration of the spectrum of K^{42} in the body enables the Compton spectrum due to K^{40} in a normal body to be calculated. Subtraction of this K^{40} Compton spectrum from the normal body spectrum leaves at 0.66 Mev a photopeak due to Cs^{137}, and from this the Cs photopeak count may be obtained. Using the calibration, and a knowledge from theory and subsidiary experiments of the variation with photon energy of (i) the self-absorption of the body and of material between it and the crystal (ii) the capture cross section of NaI, and (iii) the probability of a count appearing in the photopeak of the energy spectrum, the activity corresponding to this Cs photopeak count may be obtained.

The results show a much greater spread than do the K content measurements. The average Cs^{137} activity in the 30 students tested was (December, 1958) 7.8 mμc, or, comparing the potassium and cesium contents, 51 $\mu\mu$c/g K. The spread of individual activities is shown in Table II, which also gives the average liquid milk drunk by the persons in each group.

TABLE II
Cesium/potassium ratios

Cs/K, $\mu\mu$c/g K	No. in group	Average daily milk intake of group, imperial pints
<40	7	1.3
40–59	14	2.1
60–79	8	2.1
>80	1	3.5

DISCUSSION

The result for the total potassium content of the body, $0.21_2\%$ of the total body weight, is in very good agreement with other determinations of this quantity made on subjects from other countries by different research teams (Burch and Spiers 1953; Miller and Marinelli 1956; Shohl 1939). This agreement gives confidence in the results for the cesium content of the 30 subjects. As stated in the introduction, it might be expected that there is a latitude variation in the Cs/K ratio. Toronto (44° N.) results should not be expected to vary greatly from results obtained at Chicago (42° N.). In fact the average of 13 persons there in June, 1957, was 35 $\mu\mu$c/g K (Miller and Marinelli 1957). It will be seen that the Toronto figures are 40% higher than the 1957 Chicago results, but this is perhaps not unexpected owing to the rather large number of nuclear bomb tests during the summer of 1958.*

From the table, it will be seen that there is here evidence for a correlation of the Cs^{137} content of the body and milk intake, as has been previously suggested (Miller and Marinelli 1957). It is of interest to note that (i) the person with the lowest Cs/K ratio drank no milk, and (ii) the Cs/K ratio for a sample of powdered milk produced in Ontario was measured to be 31 $\mu\mu$c/g K (McNeill and Trojan 1959).

It is proposed to follow up this work by testing the same group of students at intervals for the next few years so that any change in the activity of this control group may be noted.

ACKNOWLEDGMENTS

This work has been made possible by a National Health Grant from the Ontario Department of Health and the Department of Health and Welfare, Ottawa. Our thanks are also due to Dr. W. H. Watson and Dr. H. E. Johns of the University of Toronto and to Drs. J. C. Rose and L. Marinelli of the Argonne National Laboratory for many helpful discussions, and to the workshop staff of the Department of Physics of the University of Toronto who, under the direction of Mr. B. Clark, erected the steel room.

*NOTE ADDED IN PROOF: Since the writing of this paper, we have received ANL 5919, in which C. E. Miller and L. D. Marinelli state that the July 1958 Cs/k ratio for Chicago residents is 52 $\mu\mu$c/g K, in good agreement with our figure.

REFERENCES

ANDERSON, E. C., SCHUCH, R. L., FISHER, W. R., and LANGHAM, W. 1957. Science, **125**, 1273.
BEAMISH, F. E. 1958. Private communication.
BURCH, P. R. J. and SPIERS, F. W. 1953. Nature, **172**, 519.
LIBBY, W. F. 1958. Proc. Natl. Acad. Sci. **44**, 800.
MAYNEORD, W. V., ANDERSON, W., BENTLEY, R. E., BURTON, L. K., CROOKHALL, J. O., and TROTT, N. G. 1958. Nature, **182**, 1473.
McNEILL, K. G. and TROJAN, O. 1959. Private communication.
MILLER, C. E. 1956. Argonne National Laboratory ANL 5596, p. 26.
MILLER, C. E. and MARINELLI, L. 1956. Radiology, **66**, 104.
——— 1957. Argonne National Laboratory ANL 5755, p. 47.
MILLER, C. E., MARINELLI, L. D., ROWLAND, R. E., and ROSE, J. E. 1956. Nucleonics, **14** (4), 40.
MILLER, C. E. and STEINGRABER, O. J. 1957. Argonne National Laboratory ANL 5679, p. 32.
RAPOPORT, A. 1959. Private communication.
REINES, F., SCHUCH, R. L., COWAN, C. L., HARRISON, F. B., ANDERSON, E. C., and HAYES, F. N. 1953. Nature, **172**, 521.
SHOHL, A. T. 1939. Mineral metabolism (Reinhold Publishing Corp., New York).
STROMINGER, D., HOLLANDER, J. M., and SEABORG, G. T. 1958. Revs. Modern Phys., **30**, 585.

POLARIZATION OF RADAR ECHOES FROM AURORA[1]

A. KAVADAS AND D. G. GLASS

ABSTRACT

Auroral radar echoes at very high frequency received at antennas sensitive to linearly polarized components in directions symmetrical to the plane of polarization of the vertically polarized transmitted wave and the ground plane indicate that the received wave, in addition to an unpolarized component, contains a linear component of polarization tilted in the general direction of the earth's magnetic field lines.

INTRODUCTION

Radar echoes from aurora when observed at frequencies in the lower part of the very high frequency band are often found to exhibit interesting polarization effects. In some cases the received signal is found to be equally strong on two orthogonally polarized antennas, one of which has the polarization of the transmitting antenna. Such echoes are said to be depolarized and the degree of depolarization for various circumstances has been investigated by several workers (Harang and Landmark 1953, 1954; McNamara and Currie 1954). The most complete study seems to be that of McNamara and Currie (1954), who found that at 56 Mc/sec an appreciable number of echoes showed some or complete depolarization. They also found that when the transmitted wave was horizontally polarized the ratio of the horizontal component to the vertical component of the received wave was a function of range. Echoes less depolarized were more frequently observed at ranges of 500 to 900 km, a region of the sky where the direction of the incident wave and the direction of the earth's magnetic field were almost perpendicular. Most of the workers found that the degree of depolarization decreased with increasing frequency.

The force of the earth's magnetic field may influence the polarization of the aurorally reflected signals either by means of Faraday rotation or indirectly by providing an axis of symmetry of the reflecting clouds of ionization. The clouds can be visualized as elongated along the lines of force of the magnetic field, and under certain circumstances this may lead to a backscatter cross section for the clouds, either singly or collectively, which may vary with the plane of polarization.

This paper concerns an investigation of the polarization of aurorally reflected signals which had as its main objective the discovery of any effects which are related to the earth's magnetic field.

EXPERIMENTAL

If the change in the state of polarization of the incident wave is associated with the angle between the plane of polarization of the incident wave and

[1]Manuscript received January 19, 1959.
Contribution from the Institute of Upper Atmospheric Physics, University of Saskatchewan, Saskatoon, Saskatchewan. Work was performed under Defence Research Board of Canada, Contract Nos. PG 69-613013 and PG 69-813002.

the direction of the earth's magnetic field, the received wave may behave in a way which depends on whether the echo originates to the east or to the west of the observer's magnetic meridian. Consider an observer located near the receiving antennas; to such an observer the lines of force of the earth's magnetic field will appear to be vertical when viewed along the magnetic meridian, but they will diverge almost symmetrically, making an angle with the vertical along eastward or westward directions. The reflected waves from these directions might then contain linearly polarized components tilted away from the vertical.

In order to detect such components, receiving antennas sensitive to linearly polarized waves in directions $+45°$ and $-45°$ from the vertical were selected. These were a pair of two identical dipoles crossed at their centers and mounted in the form of an X.

At the low frequencies employed ground reflections are almost inevitable. It was, therefore, important that the two dipoles were equally affected by these reflections. The X antenna satisfied this condition by having its two elements symmetrically located with respect to the ground plane. This property of symmetry is demonstrated in Fig. 1(*a*). The electric vectors associated with the wave received at y, x are proportional to the sum and difference of the same two quantities, the vertical and horizontal component of the received wave, v and h respectively.

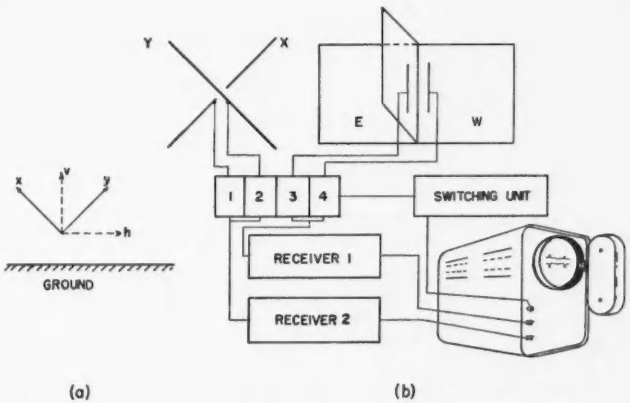

FIG. 1. (*a*) Symmetry properties of X antenna. (*b*) Experimental arrangement.

No transmitting equipment was installed. The presence of an I.G.Y. auroral radar (McNamara 1958), located in the vicinity, provided a vertically polarized transmitted wave at the frequency of 48.2 Mc/sec.

The complete experimental arrangement is shown in Fig. 1(*b*). Signals from the receiving dipoles y and x were alternately displayed on the two halves of the upper trace of a dual beam oscilloscope. On the lower trace of the same oscilloscope the signals from the two antennas, marked E and W

in Fig. 1(*b*), were similarly displayed. These two antennas were vertical dipoles with corner reflectors, directed in an eastward and westward direction respectively, and indicated whether the signal was received from the western or the eastern part of the sky. In order to distinguish the traces corresponding to the two corner reflector antennas E and W, an identifying pulse appeared on the western corner reflector trace. Both traces were locked together by means of a synchronizing circuit contained in the switching unit, so that the order of appearance of the signals could not change by mistriggerings or other interference. Range markers were displayed at 100-km intervals and the complete display was sampled by a 16-mm movie camera at a rate of 2.75 frames per minute. The exposure time was 1.8 seconds per frame. Samples of these films may be seen in Fig. 2.

Because cross talk between the two dipoles would tend to reduce the difference in intensity between the signals received at the two antennas, particular attention was paid to the signal rejection between the antennas. The cross talk was kept at all times lower than -22 db.

The signals from the dipoles y and x were fed to the inputs 1 and 2 by low-loss coaxial cables (Fig. 1(*b*)) and the impedances were matched at the inputs of the two radio-frequency grounded grid amplifiers 1 and 2, instead of at the antennas, in order to minimize instabilities that could result from varying outdoor weather conditions.

The switching amplifiers 1 and 2 were constructed with identical characteristics, their "on" times being those for which the grids were at ground potential. Both amplifiers 1 and 2 have a common output connected to "receiver 2" (Fig. 1(*b*)). The measured cross talk between these amplifiers was -48 db.

Variations in the characteristics of amplifiers 1 and 2, due to aging of tubes or other factors, were checked continuously by means of a short vertical antenna that was placed in front of the X antenna at a distance sufficient to prevent interference with the receiving antenna field. A delayed pulse was impressed on this antenna; this pulse could be used for quick calibrations of the receiving equipment and a continuous check on the performance of the system. Due to its location with respect to the E, W antennas, this antenna could only be seen by the western corner reflector and thus it also supplied the identifying pulse.

OPERATIONAL DETAILS AND OBSERVATIONS

The receiving equipment was operated as continuously as possible for a period of approximately 2.5 months (March 4 to May 18, 1958) during the night hours. The number of daytime echoes was too small to warrant an attempt to record them.

The plane of the receiving antennas could be rotated about a vertical axis enabling recordings to be made with the antenna facing east, northeast, north, and northwest. The results were tabulated with reference to antenna position. Of the 513 usable samples obtained, only 24 were received from the northwestern direction. Severe local interference was mainly responsible for the lack of usable echoes from that direction.

PLATE I

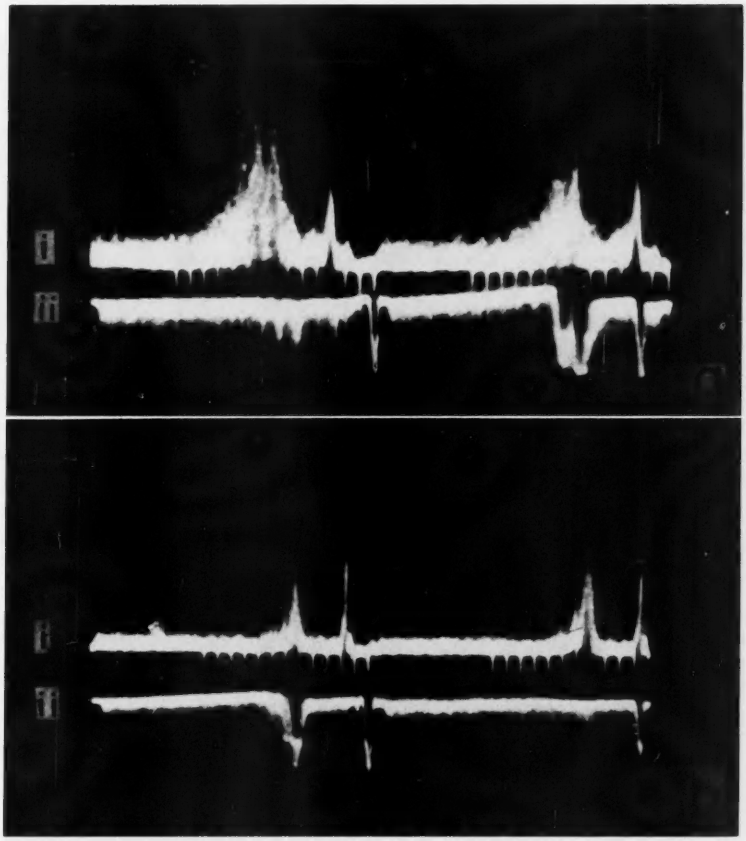

FIG. 2. Some typical radar echo samples: (*a*) echo from the west, $y < x$; (*b*) echo from the east, $y > x$.

(*a*, i), (*b*, i): signals from the x dipole appear on the left-half trace signals, from the y dipole on the right-half.

(*a*, ii), (*b*, ii): signals from the E antenna appear on the left-half trace signals, from the W antenna on the right-half.

The received signal intensities at the antennas y and x, denoted by y and x for the remainder of this paper, were divided into the following three classes for each position of the antenna:

(i) samples for which $y > x$ indicating a linear component of polarization tilted in the general direction of the y dipole;

(ii) samples for which $y = x$ indicating a vertically or horizontally polarized wave but also a circularly or randomly polarized wave;

(iii) samples for which $y < x$ indicating again a linear component of polarization tilted in the general direction of the x dipole.

Figure 3 shows a histogram of frequency of occurrence of samples with $y > x$ and $y < x$ against antenna position. For $y > x$, the number of samples is largest when the antenna faces in an easterly direction. The number decreases as the antenna is rotated towards the west. The converse is true for echoes with $y < x$. Because the receiving antenna could not be rotated until it faced west, the dotted class interval at the end of the histograms of Fig. 3 represents the number of samples with $y > x$ and $y < x$ for echoes received from directions west of the magnetic meridian but with the antenna facing north.

Figure 4 shows a similar plot but for echoes with $y = x$. The last interval in this histogram was again obtained from the north position of the antenna. This curve shows a maximum for echoes from the north.

Figure 5 shows a plot of all echoes with $y > x$ and $y < x$, obtained when the antenna was directed towards north. The direction of arrival of the echoes

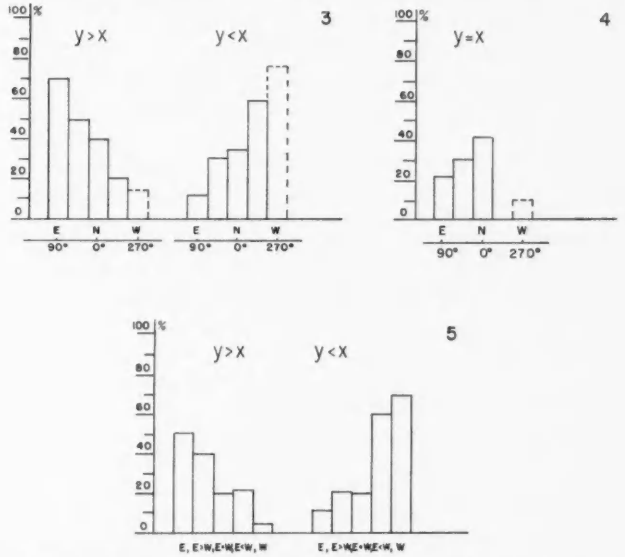

FIG. 3. Percentage echo occurrence plotted against position of antenna: (*a*) echoes with $y > x$; (*b*) echoes with $y < x$.

FIG. 4. Percentage of echoes of equal intensity on both dipoles ($y = x$) plotted against antenna position.

FIG. 5. Percentage echo occurrence plotted against azimuthal direction of echo arrival.

is indicated by the presence of the signal in either the E corner reflector for echoes arriving from the east, or the W corner reflector for echoes arriving from the west. Five points were obtained for this curve:

(i) echo only on the trace corresponding to the eastern corner reflector, denoted by E;

(ii) echo on both the eastern and western corner reflectors, denoted by $E = W$, $E > W$, $E < W$;

(iii) echo only on the western corner reflector, denoted by W. This histogram appears to be quite similar to that obtained in Fig. 4.

The histograms in Fig. 3 to Fig. 5 indicate that the receiving equipment detects a linear component of polarization tilted away from the vertical and in the same direction as the general direction of the lines of the earth's magnetic field. The information obtained by this method of observation cannot provide the exact direction of the plane of polarization of the reflected wave. Therefore, it is not possible to say whether the direction of polarization of the received wave is exactly that of the magnetic lines of force.

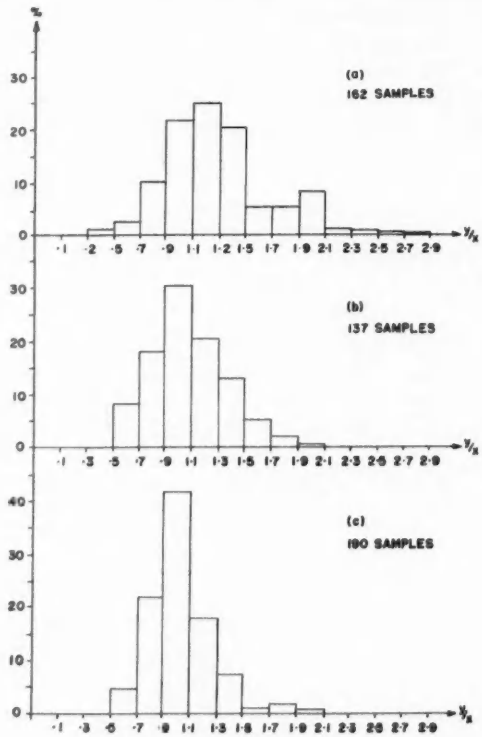

FIG. 6. Ratios of intensities y/x plotted against frequency of occurrence for three position of the antenna: (*a*) antenna facing toward the east; (*b*) antenna facing toward the northeast; (*c*) antenna facing toward the north.

It is possible to find an additional relation between the direction of the magnetic lines and the direction of the plane of polarization of the received wave. The magnetic lines diverge more rapidly for directions well removed from the magnetic meridian than they do for directions near the magnetic meridian. If the ratio y/x is plotted against frequency of occurrence, the resulting curves should show greater dispersion for echoes received when the antenna faces toward the east rather than when it faces north.

This effect may be seen in the histograms of Fig. 6 (*a*), (*b*), and (*c*). Since the number of samples was different for each case, the histograms have been normalized by expressing occurrences as percentage of the total number of samples received from the east; it is interesting to note that the histogram of Fig. 6(*a*) peaks in the interval 1.1–1.3. The displacement of the maximum with increasing azimuthal angle is also suggestive of the greater tilt in the average linear component of polarization for echoes arriving from that direction.

As mentioned before the number of echoes obtained from the west does not allow their statistical treatment and, therefore, no such curves have been plotted.

It has been reported by Harang and Landmark (1954) that sharp echoes tend to retain the plane of polarization of the transmitted wave while diffuse echoes become depolarized. Most of the received echoes during the present investigation could not be separated into diffuse and discrete echoes with certainty and no attempt was made to treat them separately.

CONCLUSIONS AND DISCUSSION

The results obtained indicate that for a large number of echoes the plane of polarization of the transmitted wave is not maintained upon reflection. The work of Harang and Landmark (1953, 1954) and McNamara and Currie (1954) has already shown that the reflected wave tends to be randomly polarized. In addition, the reflected wave is found to contain a linear component of polarization other than the vertical. This component appears to be tilted in the same general direction as the earth's magnetic lines of force.

This finding does not exclude the presence of other components. It should be noted that even if the reflected wave is linearly polarized, the received wave will, in general, be elliptically polarized as a result of ground reflections. Therefore, the presence of circular components in addition to the linear components is almost certain. This is not true if the reflected wave retains its plane of polarization (vertical).

In all positions of the receiving antenna signals $y = x$ have been obtained. These may be due to (i) a completely unpolarized signal, (ii) a vertically or horizontally polarized signal, and (iii) a circularly polarized signal. The experimental arrangement used does not distinguish between these cases. It is interesting to note, however, that in all antenna positions in Fig. 6 (*a*), (*b*), and (*c*) the frequency of occurrence of ratios y/x lying between 0.9 and 1.1 is quite large. This suggests that not all echoes contain a tilted component of linear polarization, and that a large number of them fall into one or other of the groups (i), (ii), and (iii) mentioned above.

The general change in the state of polarization of the incident wave may be attributed to any one of several factors and possibly to a combination of these factors.

A plane polarized wave, scattered by an assembly of isotropic or non-isotropic scatterers, may, under certain conditions, change its plane of polarization. In addition, unpolarized components should be expected in the scattered wave, though the depolarizing mechanisms may be different for the two types of scatterers.

Multiple scattering within the assembly, though a second-order effect, will tend to depolarize the incident wave whether the scatterers are isotropic or anisotropic and the degree of depolarization will depend on the spacing between scatterers. Alternatively, if the scatterers have a sufficient electron density, they may be asymmetrical to the frequency used and if the degree of anisotropy varies randomly from scatterer to scatterer, an appreciable part of the incident wave will become depolarized. The percentage of the received signal that becomes unpolarized depends on the randomness of the degree of anisotropy within the assembly. In addition to the depolarizing effects which can be associated with the target, scatter from ground irregularities or objects near the antenna that may contribute to the depolarization of the wave should not be overlooked, although it cannot account for complete depolarization.

The unpolarized components along with the circular components that result from direct ground reflections will tend to reduce the difference in intensity between the signals received at the two antennas y and x. Thus the actual tilt in the plane of polarization of the received wave will be masked to a certain extent. The clustering of the ratios y/x around the value 1 in Fig. 6 may be attributed to this effect.

Faraday rotation, a basically different mechanism, may also contribute to the change in the state of polarization of the incident wave, whenever the ionic concentration of the echoing region attains sufficiently high densities. This effect, however, is not a likely cause for the rotation of the plane of polarization of the reflected wave. The echoes originate in regions where the magnetic lines are almost perpendicular to the propagation vector of the wave and so the Faraday rotation should be correspondingly slight. Even if such an effect were present, the received wave would exhibit linear components of polarization in random orientations depending on the depth and degree of ionization penetrated by the incident wave. Therefore, one may conclude that any residual Faraday rotation that exists cannot account for the observed tilt in the plane of polarization of the incident wave.

As mentioned previously the incident wave may be cross-polarized by assemblies of scatterers, some of which are sufficiently elongated along the earth's magnetic field lines to be non-isotropic to the incident wave. Such scatterers would have different reflectivities for polarizations parallel to and perpendicular to their axes of symmetry. The non-isotropic reflectivity of these scatterers may change during the lifetime of the scatterer to the extent that it may even become isotropic. Since the scatterers may be formed at

different times and places within the assembly, the values of their anisotropic reflectivities would be expected to fluctuate about a mean, making possible all the observed values of y/x in Fig. 6.

An attractive alternative to this consideration (Forsyth 1958) may be that the tilt in the plane of polarization of the incident wave could result from multiple scattering, by scatterers which are elongated along the lines of force of the earth's magnetic field, but are sufficiently large to exhibit individual backscattering cross sections which are independent of the radio wave polarization. Such scatterers will tend to radiate secondary waves with electric vectors on a plane parallel to the magnetic lines. Successive scatterings of such waves will result in the enhancement of a component with the electric vector parallel to the earth's magnetic lines. In addition, this mechanism will provide an abundance of randomly polarized components consistent with the multitude of ratios $y/x = 1$ for all positions of the antenna.

ACKNOWLEDGMENTS

The authors are indebted both to Dr. B. W. Currie and to Dr. P. A. Forsyth for many helpful discussions and suggestions.

REFERENCES

FORSYTH, P. A. 1958. Private communication.
HARANG, L. and LANDMARK, B. 1953. Nature, **171**, 1017.
——— 1954. J. Atmospheric and Terrest. Phys. **4**, 322.
MCNAMARA, A. G. 1958. Can. J. Phys. **36**, 1.
MCNAMARA, A. G. and CURRIE, B. W. 1954. Nature, **174**, 1153.

THE CALCULATION OF THE ELECTRIC POTENTIAL AND THE CAPACITY OF A TORE BY MEANS OF TOROIDAL FUNCTIONS[1]

S. C. Loh[2]

ABSTRACT

Expressions in terms of toroidal functions for the electric potential and the capacity of a tore with respect to infinity are derived. Some numerical calculations of the potential are presented for tores of different sizes in order to illustrate the derived results.

The electric capacity of a tore is also calculated and the numerical results are compared with those of a sphere of radius a.

INTRODUCTION

The electric potential and the capacity of a tore with respect to infinity are usually calculated approximately, assuming that the diameter of the conductor is small compared with that of the tore. The exact solution of the problem has been treated by Hicks (1881) and Dyson (1893). The latter expressed the potential of an anchor ring of circular cross section in terms of an infinite series.

In the present paper, expressions for the potential and the capacity of a tore are derived by means of toroidal functions. Some calculations of the potential and the capacity are presented for tores of different size in order to illustrate the derived results.

ELECTRIC POTENTIAL OF A TORE

The potential ϕ of an electrostatic field always satisfies the differential equation known as Laplace's equation. The general solution of Laplace's equation in toroidal co-ordinates is given by Carter and Loh (1958) as follows:

$$(1) \qquad \phi = \sqrt{(\cosh u - \cos v)} \sum_{n=0}^{\infty} \{a_n p_n(u) + b_n q_n(u)\} \cos(nv + \alpha_n)$$

where α_n, a_n, and b_n are arbitrary constants,

$p_n(u)$ and $q_n(u)$ are known as "toroidal functions" of the first and second kinds, respectively.

The toroidal co-ordinates, u, v, w, are related to the well-known Cartesian co-ordinates, x, y, z, by the following expressions:

$$(2) \qquad \begin{cases} x = \dfrac{a \sinh u \cos w}{\cosh u - \cos v} \\ y = \dfrac{a \sinh u \sin w}{\cosh u - \cos v} \\ z = \dfrac{a \sin v}{\cosh u - \cos v} \end{cases}$$

[1]Manuscript received March 3, 1959.
Contribution from the Radio and Electrical Engineering Division, National Research Council, Ottawa, Canada.
Issued as N.R.C. No. 5191.

[2]National Research Council Postdoctorate Fellow.

When the central plane is a plane of symmetry, $\alpha_n = 0$; therefore using eq. (1), the potential (with respect to infinity) outside a charged tore is given by:

$$\phi = \sqrt{(\cosh u - \cos v)} \sum_{n=0}^{\infty} \{a_n p_n(u) + b_n q_n(u)\} \cos nv.$$

The constants a_n and b_n must be so chosen as to make $\phi = V$ on the tore (where $u = u_1$, shown in Fig. 1), and $\phi = 0$ at infinity; thus

$$b_n = 0, \tag{3}$$

and

$$V = \sqrt{(\cosh u_1 - \cos v)} \sum_{n=0}^{\infty} a_n p_n(u_1) \cos nv. \tag{4}$$

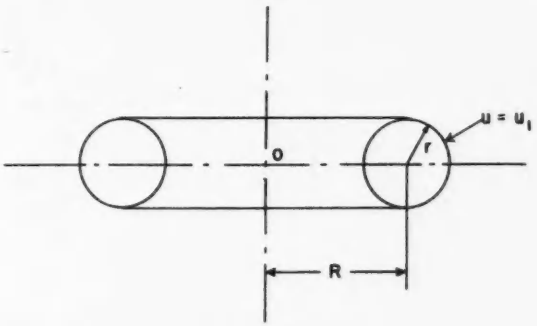

FIG. 1. The tore.

In order to determine the arbitrary constant a_n, we multiply both sides of eq. (4) by $\cos nv\, dv$ and integrate from 0 to 2π. Equation (4) yields to

$$\frac{\pi}{2} a_n p_n(u_1) = \delta_n \int_0^{\pi} \frac{V \cos nv}{\sqrt{(\cosh u_1 - \cos v)}}\, dv \tag{5}$$

where $\delta_n = 1$ when $n \geqslant 1$, but $\delta_0 = \frac{1}{2}$.

The integral may be evaluated readily by using the following identity:

$$\int_0^{\pi} \frac{\cos nv\, dv}{\sqrt{(\cosh u - \cos v)}} = \sqrt{2}\, q_n(u). \tag{6}$$

Substituting eq. (6) into eq. (5), we obtain

$$a_n = \frac{2\sqrt{2}V}{\pi} \delta_n \frac{q_n(u_1)}{p_n(u_1)}. \tag{7}$$

Hence the general expression for the electric potential at any point (u, v) outside the tore $(u = u_1)$ having a constant voltage V is

$$\phi = V \sqrt{(\cosh u - \cos v)} \frac{2\sqrt{2}}{\pi} \sum_{n=0}^{\infty} \delta_n \frac{q_n(u_1)}{p_n(u_1)} p_n(u) \cos nv. \tag{8}$$

The potential outside a tore given by eq. (8) is calculated and plotted in Fig. 2.

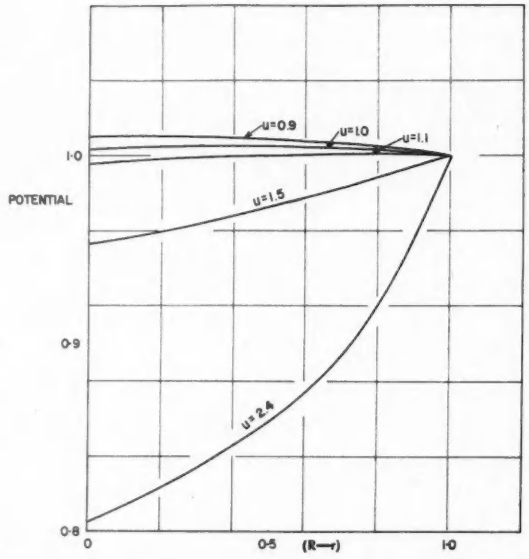

FIG. 2. Potential outside the tore on the plane $v = \pi$.

The above expression for the potential of a tore at any external point is identical with that given by Hicks (1881). This problem was also investigated by Dyson (1893) with a different approach, and his results were expressed as an infinite series.

THE ELECTRIC CAPACITY OF A TORE

In order to determine the capacity of a tore, it is necessary to take the surface integral of $(1/v)\epsilon(\partial\phi/\partial\eta)$ over it.

Let C be the capacity of the tore with respect to infinity,

$$(9)\quad C = \frac{\epsilon}{v}\int_0^{2\pi} 2\pi p \frac{\partial\eta}{\partial v}\cdot\frac{\partial\phi}{\partial u}\cdot\frac{\partial u}{\partial\eta}\,dv$$

$$= 4\sqrt{2}\,\epsilon\, a \sinh u \sum_{n=0}^{\infty} \delta_n \frac{1}{\cosh u - \cos v}\left\{\frac{\sinh u}{2\sqrt{(\cosh u-\cos v)}}\,p_n(u)\right.$$

$$\left. +\sqrt{(\cosh u-\cos v)}\,\frac{dp_n}{du}\right\}\frac{q_n(u_1)}{p_n(u_1)}\cos nv\,dv.$$

Putting

$$(10)\qquad \frac{dp_n}{du} = \frac{2n+1}{2\sinh u}\,(p_{n+1} - \cosh u\, p_n),$$

and simplifying the expression, eq. (9) becomes

$$C = 16\,a\epsilon \sum_{n=0}^{\infty} \delta_n \left\{ \frac{2n+1}{2} \left[C' p_n q_n - p_n q_{n+1} + p_{n+1} q_n - C' p_n q_n \right] \frac{q_{n1}}{p_{n1}} \right\} \tag{11}$$

where C' denotes cosh u.

To evaluate eq. (11), we shall employ the following identity:

$$p_{n+1} q_n - p_n q_{n+1} = \frac{2}{2n+1}. \tag{12}$$

Then substituting eq. (12) into eq. (11) yields

$$C = 16\,a\epsilon \sum_{n=0}^{\infty} \delta_n \frac{q_n(u_1)}{p_n(u_1)}. \tag{13}$$

It may be interesting to compare the capacity of a tore with that of a sphere having radius a. The capacity of a sphere carrying a total charge Q uniformly distributed is well known and can be expressed as

$$C_s = 4\pi\epsilon a. \tag{14}$$

Hence the ratio is

$$\frac{4}{\pi} \sum_{n=0}^{\infty} \delta_n \frac{q_n(u_1)}{p_n(u_1)}. \tag{15}$$

The ratio given by eq. (15) is plotted in Fig. 3. Instead of using u as an in-

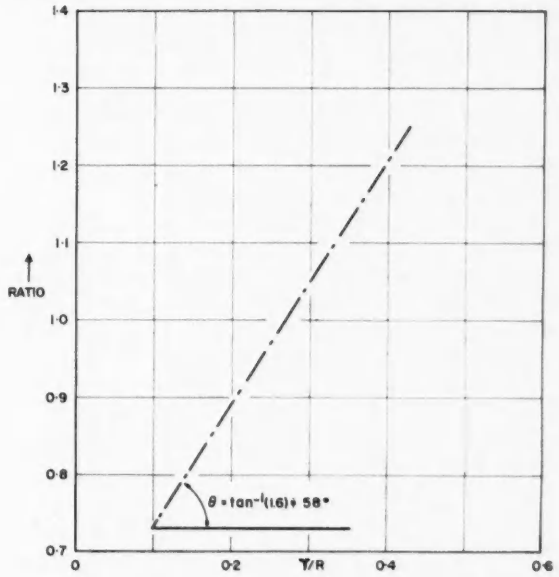

FIG. 3. Capacity of the tore/capacity of the sphere.

dependent variable, the dimension ratio r/R (see Fig. 1) has been employed. The relation between u and r/R is

$$u = \text{arc sech } (r/R). \tag{16}$$

The capacity of a "ring without hole" with respect to infinity has recently been calculated by Bouwkamp (1955), using the method of images. He expressed the capacity in terms of the ratio (volume/surface area of the ring).

CONCLUSIONS

Expressions for the potential and the capacity of a tore with respect to infinity have been derived. The potential distribution in the plane $v = \pi$ has been shown (in Fig. 2) to be mainly determined by the size of the tore. For tores $0.9 \leqslant u \leqslant 1.1$; that is, the diameter of the conductor is large compared with that of the tore, the potential in the plane $v = \pi$ is nearly constant.

The capacity of a tore is directly proportional to that of a sphere, and this may be seen in Fig. 3.

ACKNOWLEDGMENT

The author wishes to thank the National Research Council of Canada for the award of a Postdoctorate Fellowship.

REFERENCES

BOUWKAMP, C. J. A simple method of calculating electrostatic capacity, Institute of Engineering Research, University of California, Los Angeles, California (unpublished).
CARTER, G. W. and LOH, S. C. 1958. Proc. Inst. Elec. Engrs. C, **105**, 13.
DYSON, F. W. 1893. Phil. Trans. Roy. Soc. London A, **184**, 43, 96.
HICKS, W. H. 1881. Phil. Trans. Roy. Soc. London, **31**, 609.

HIGH RESOLUTION RAMAN SPECTROSCOPY OF GASES

XII. ROTATIONAL SPECTRA OF C_2H_4 AND C_2D_4 AND THE STRUCTURE OF THE ETHYLENE MOLECULE[1]

J. M. DOWLING[2] AND B. P. STOICHEFF

ABSTRACT

The pure rotational Raman spectra of C_2H_4 and C_2D_4 were photographed in the second order of a 21-ft grating. The resolution achieved was such that several lines due to single transitions were observed (and identified) in the spectra of both molecules. An analysis of these lines based on the non-rigid asymmetric top yielded the following rotational constants for the ground states:

C_2H_4: $A_0 = 4.828 \pm 0.009$, $B_0 = 1.0012 \pm 0.0009$, $C_0 = 0.8282 \pm 0.0004$ cm^{-1};
C_2D_4: $A_0 = 2.432 \pm 0.008$, $B_0 = 0.7369 \pm 0.0012$, $C_0 = 0.5630 \pm 0.0006$ cm^{-1}.

The structural parameters obtained from these constants are r_0(C=C) = 1.339 $\pm$0.002 Å, r_0(C—H) = 1.086 $\pm$0.003 Å, and $\angle$H—C—H = 117°34′$\pm$30′. These values are in agreement with the recent preliminary results of the electron diffraction data. There is also agreement between the above values and those obtained from a recent study of the rotation–vibration spectra of C_2H_4 and C_2D_4, although the agreement between the ground state rotational constants is not as satisfactory.

A. INTRODUCTION

The unique importance of the molecular structure of ethylene for valence theory has made this molecule a favorite for spectroscopic studies at high resolution. One of the first was the study of the pure rotational Raman spectrum by Lewis and Houston (1933). They observed a number of S branch lines ($\Delta J = 2$, $\Delta K = 0$) which were interpreted in terms of a near-symmetric top molecule. In 1939, a study of the photographic infrared spectrum was made by Thompson (1939). Later, Gallaway and Barker (1942) investigated the infrared spectra of both C_2H_4 and C_2D_4. They noted an irregularity in intensity of the rotational lines, but the analysis was again based on the symmetric top. It is this study which has led to the much quoted parameters r(C=C) = 1.353 Å, r(C—H) = 1.071 Å, and $\angle$HCH = 120°, for the structure of the ethylene molecule.

The pure rotational Raman spectrum was reinvestigated by Romanko, Feldman, Stansbury, and McKellar (1954) at much higher dispersion than that used by Lewis and Houston. In addition to the "symmetric" top R and S branches they also observed another series of lines (called the S' branch) which was due to "asymmetric" top transitions. This was the first report of the departure of the spectrum from that of a symmetric top molecule and encouraged the study of the ethylene spectrum at even higher resolution.

While the present investigation was in progress, Allen and Plyler (1958) reported their results of a study of the infrared spectra of C_2H_4 and C_2D_4.

[1]Manuscript received March 4, 1959.
Contribution from the Division of Pure Physics, National Research Council, Ottawa, Canada.
Issued as N.R.C. No. 5199.
[2]National Research Council Postdoctorate Fellow 1957–1959.

They observed an alternation in intensity of the $K_a = 0$ and $K_a = 1$ lines of the parallel bands studied, thus confirming the planar symmetrical structure of ethylene (point group V_h). Their analysis of these two parallel bands (up to $J \leqslant 10$) yielded the following structure: r(C=C) = 1.337 Å, r(C–H) = 1.086 Å, and $\angle$H—C—H = 117°22′. These values differ significantly from the earlier values quoted above, but are essentially the same as those reported by Bartell and Bonham (1957) from the preliminary results of electron diffraction data, namely r(C=C) = 1.334 Å, r(C—H) = 1.085 Å, and $\angle$H—C—H = 116°.

The present paper is a report of the analysis of the rotational Raman spectra of C_2H_4 and C_2D_4 photographed with a 21-ft grating. The resolution achieved was high enough to warrant analysis based on the non-rigid asymmetric top. Since this is the first time that such an analysis has been carried out for a Raman spectrum, a fairly detailed account will be given, including a review of the theory of the asymmetric top energy levels.

In earlier papers of this series many examples of the pure rotational spectra of linear and symmetric top molecules were shown. All of the spectra were simple in appearance; the lines were evenly spaced and had a regular intensity distribution. The rotational numbering was unambiguous and the analysis straightforward. In general, this simplicity is also found in many of the *rotation–vibration* bands of linear and symmetric top molecules.

On the other hand, the rotational spectra of asymmetric top molecules exhibit such a complex appearance (and the spectra of C_2H_4 and C_2D_4 are no exceptions) that the identification of rotational lines is not evident, and in general one must resort to other means of analysis. In principle the usual procedure is very simple, but in practice it may be tedious and time-consuming. The starting point is a calculation of the spectrum with assumed rotational constants. The calculated spectrum is then compared with the observed spectrum and the deviations noted. The rotational constants are modified until the agreement between the calculated and observed spectra is considered satisfactory.

Under favorable circumstances, particularly when the spectrum is observed at high resolution, the above procedure may lead to the identification of individual rotational lines, that is, lines due to single transitions. These can then be used to determine the rotational constants explicitly. Such a procedure is customary in the analysis of the microwave spectra of asymmetric tops. Fortunately, several lines in the Raman spectra of C_2H_4 and C_2D_4 reported here were identified as single transitions and, as shown below, their analysis has led to the evaluation of the rotational constants of these molecules.

B. EXPERIMENTAL DATA

The apparatus, including the mirror-type Raman tube, mercury lamps, and 21-ft grating spectrograph, has been described in the first paper of this series (Stoicheff 1954). As in the earlier work, the present Raman spectra were excited by the Hg 4358 line and photographed with a reciprocal linear dispersion of 6.75 cm^{-1}/mm on Kodak 103*a*0 photographic plates. Slit widths

FIG. 1. The pure rotational Raman spectra (Stokes branches) of ethylene, C_2H_4, and ethylene-d_4, C_2D_4. The spectrum of C_2D_4 was obtained with a cylindrical lens placed in the spectrograph in front of the photographic plate.

of 0.02 and 0.03 mm were used. Second- and third-order iron lines excited in a hollow cathode provided standards of wavelength.

In preliminary experiments, it was found that the rotational lines of C_2H_4 were somewhat broadened by gas pressures of 1 atmosphere. Sharper lines were obtained at a pressure of $\frac{1}{2}$ atmosphere resulting in considerably better resolution of the spectrum. The final photographs of the C_2H_4 and C_2D_4 spectra were therefore taken at this pressure. Five photographs of each spectrum were obtained with exposure times ranging from 1 to 24 hours. Several photographs of higher density were obtained with a cylindrical lens placed in front of the photographic plate.

Examples of the pure rotational spectra of C_2H_4 and C_2D_4, showing the Stokes branches, are reproduced in Fig. 1. Also, a microphotometer trace of part of the C_2H_4 spectrum is shown in Fig. 2. The most prominent feature in the spectra of both molecules is the irregularity in line spacing and in intensity distribution. Of course, this irregularity is to be expected for the rotational spectra of asymmetric top molecules and is therefore an obvious confirmation of the asymmetric top structure of ethylene.

The Raman displacements of the C_2H_4 rotational lines are listed in Table I and those of C_2D_4 in Table II. The values are averages of the Stokes and anti-Stokes lines measured on five plates. Sharp lines of medium or higher intensity have an accuracy of $\pm 0.03\ cm^{-1}$ and the remainder have an accuracy of about $\pm 0.06\ cm^{-1}$. These errors are based on the internal consistency amongst the five plates for each molecule.

One of the problems presented by the irregular spacing of the rotational lines was the difficulty in recognizing grating ghosts particularly in the region of the exciting line. For this purpose a thorough study of the ghost positions and intensities in the region of $\lambda 4358$ Å was carried out. Several photographs were obtained using one of the lamps as a source and accurate measurements of ghost positions were made as in the case of the Raman spectra. A direct comparison of the Raman spectra and ghost plates led to the elimination of some lines and to the identification of others as blends with grating ghosts. Of the latter group, those which fell within $\pm 0.2\ cm^{-1}$ of a ghost and appeared to have a higher intensity than that expected for the ghost alone were retained up to the final stages of analysis. In Tables I and II only those blended lines for which an assignment could be made were included (in parentheses).

C. REVIEW OF THEORY

1. Rotational Energy Levels

The rotation energy levels of a prolate symmetric top ($B = C$) are given by

$$F(J, K) = BJ(J+1)+(A-B)K^2 \tag{1}$$

in the usual notation (Mulliken 1955). J can take the values $0, 1, 2, \ldots$ and for each J there are $J+1$ sublevels with K values $0, 1, 2, \ldots J$. Each sublevel with $K \neq 0$ is doubly degenerate. For only a "slight" deviation from the symmetric top, K remains a "good" quantum number and the energy levels can be represented by eq. (1) but with B replaced by $\frac{1}{2}(B+C)$. Indeed, this

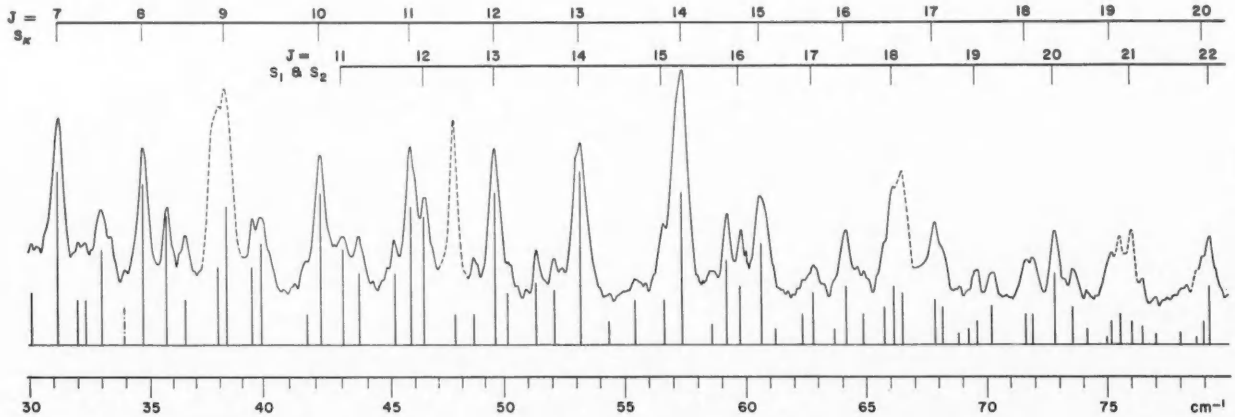

FIG. 2. A microphotometer trace of the pure rotational Raman spectrum of ethylene from 30 to 80 cm^{-1} and the calculated spectrum assuming a resolution of 0.25 cm^{-1}. (Portion of the spectrum shown as dashed lines indicate overlapping by grating ghosts. The line designated — · — · — is assigned as a transition for which $\Delta K_a = 2$.) The series designated S_K and S_1, S_2 are essentially the spectrum observed by Romanko *et al.* (1954) at lower resolution.

TABLE I

The pure rotational Raman spectrum of ethylene

$\Delta\nu$ obs.	Transition	$\Delta\nu$ calc	I^a
(9.606)[b]	$S_2(1)$	9.576	778
	$R_2(9)$	9.567	21
	$R_3(10)$	9.615	16
	$R_3(11)$	9.540	12
(10.508)	$R_4(5)$	10.752	270
10.986	$R_6(5)$	11.001	467
	$R_7(5)$	10.996	540
	$R_8(5)$	10.996	1259
	$R_K(5)$		
(11.249)	$R_1(4)$	11.281	120
	$R_2(5)$	11.343	631
	$R_3(5)$	11.015	467
(12.173)	$S_2(2)$	12.186	819
(12.325)	$R_4(6)$	12.368	445
(12.811)	$S_1(2)$	12.721	2338
	$S_4(2)$	12.801	387
	$S_5(2)$	12.881	904
	$R_5(6)$	12.871	347
	$R_6(6)$	12.836	347
	$R_7(6)$	12.835	1042
	$R_8(6)$	12.834	447
	$R_K(6)$		
(13.682)	$S_3(2)$	13.396	819
	$R_3(6)$	13.455	191
	$R_4(7)$	13.869	138
(14.034)	$R_1(5)$	14.035	78
14.666	$R_5(7)$	14.744	260
	$R_6(7)$	14.665	260
	$R_7(7)$	14.675	353
	$R_8(7)$	14.675	824
	$R_K(7)$		
15.604	$S_2(3)$	15.651	798
	$R_3(7)$	15.694	323
	$R_4(8)$	15.229	238
(16.437)	$S_1(3)$	16.294	904
	$S_4(3)$	16.446	1233
	$S_5(3)$	16.618	528
	$S_6(3)$	16.494	214
	$S_7(3)$	16.498	214
	$R_1(6)$	16.948	54
	$R_4(9)$	16.426	77
	$R_5(8)$	16.640	196
	$R_6(8)$	16.480	196
	$R_7(8)$	16.520	642
	$R_8(8)$	16.518	275
	$R_K(8)$		
(17.410)	$S_3(3)$	17.205	798
	$R_4(10)$	17.446	135
(18.262)	$R_3(8)$	18.079	102
	$R_4(11)$	18.274	44
	$R_5(9)$	18.571	149
	$R_6(9)$	18.271	149
	$R_7(9)$	18.366	214
	$R_8(9)$	18.363	499
	$R_K(9)$		
(18.826)	$R_4(12)$	18.908	79
(19.139)	$S_2(4)$	19.105	763
	$R_4(13)$	19.350	26
(19.742)	$S_1(4)$	19.816	1943
	$R_4(14)$	19.607	47
	$R_4(15)$	19.690	16
	$R_4(16)$	19.611	29
(20.191)	$S_4(4)$	20.082	577
	$S_5(4)$	20.392	1346
	$S_6(4)$	20.170	338
	$S_7(4)$	20.179	338
	$S_8(4)$	20.153	123
	$S_9(4)$	20.154	288
	$R_1(7)$	20.011	38
	$R_3(9)$	20.625	177
	$R_5(10)$	20.555	114
	$R_6(10)$	20.028	114
	$R_7(10)$	20.223	388
	$R_8(10)$	20.210	166
	$R_K(10)$		
21.000	$S_3(4)$	20.999	763
21.966	$R_5(11)$	21.727	87
	$R_7(11)$	22.084	129
	$R_8(11)$	22.055	301
	$R_K(11)$		
22.529	$S_3(5)$	22.547	722
	$R_3(11)$	22.611	87
(23.162)	$S_1(5)$	23.285	773
	$R_1(8)$	23.216	28
	$R_2(10)$	23.342	58
23.801	$S_4(5)$	23.707	1365
	$S_6(5)$	23.851	399
	$S_7(5)$	23.872	399
	$S_8(5)$	23.827	499
	$S_9(5)$	23.830	214
	$S_{10}(5)$	23.830	72
	$S_{11}(5)$	23.830	72
	$R_7(12)$	23.957	234
	$R_8(12)$	23.898	100
	$R_K(12)$		
(24.605)	$S_5(5)$	24.774	722
	$S_6(5)$	24.208	585
	$R_3(12)$	24.759	67
25.627	$S_3(6)$	25.974	678
	$R_7(13)$	25.850	78
	$R_8(13)$	25.686	182
	$R_K(13)$		
26.695	$S_1(6)$	26.701	1672
	$R_1(9)$	26.552	21
	$R_3(11)$	26.235	103
27.476	$S_4(6)$	27.320	573
	$S_5(6)$	27.535	425
	$S_7(6)$	27.578	425
	$S_8(6)$	27.498	268
	$S_9(6)$	27.504	626
	$S_{10}(6)$	27.470	134
	$S_{11}(6)$	27.470	134
	$S_K(6)$		
	$R_3(13)$	27.027	52
	$R_5(14)$	27.549	61
	$R_K(14)$		
*28.058	$S_5(6)$	28.064	1336
(28.486)	$S_3(6)$	28.523	678
(29.284)	$S_3(7)$	29.388	632
	$R_3(12)$	29.296	34
	$R_K(15)$		
30.075	$S_1(7)$	30.069	663
	$R_1(10)$	29.996	16
31.107	$S_4(7)$	30.919	1278
	$S_6(7)$	31.222	428
	$S_7(7)$	31.302	428
	$S_8(7)$	31.176	689
	$S_9(7)$	31.183	295
	$S_{10}(7)$	31.150	175
	$S_{11}(7)$	31.150	175
	$R_K(16)$		
	$S_K(7)$		
31.922	$S_4(7)$	31.950	548
32.238	$S_3(7)$	32.239	632
32.917	$S_2(8)$	32.786	585
	$R_3(13)$	32.523	61
	$R_K(17)$		
33.381	$S_1(8)$	33.396	1422
	$R_1(11)$	33.533	12
33.975	$7_{17}\rightarrow 7_{18}$	33.980	
34.847	$S_4(8)$	34.501	516
	$S_5(8)$	34.909	416
	$S_7(8)$	35.049	416
	$S_8(8)$	34.862	304
	$S_9(8)$	34.871	710
	$S_{10}(8)$	34.829	198
	$S_{11}(8)$	34.829	198
	$R_K(17)$		
	$S_K(8)$		
35.869	$S_2(9)$	36.168	537
	$S_3(8)$	35.919	585
	$S_4(8)$	35.859	1204
	$R_3(14)$	35.900	20
36.690	$S_1(9)$	36.694	557
(38.070)	$S_4(9)$	38.065	1120
(38.531)	$S_6(9)$	38.595	396
	$S_7(9)$	38.824	396
	$S_8(9)$	38.555	702
	$S_9(9)$	38.568	301
	$S_{10}(9)$	38.508	207
	$S_{11}(9)$	38.508	207
	$S_K(9)$		
39.537	$S_2(10)$	39.539	480
	$S_3(9)$	39.555	537
	$R_3(15)$	39.420	36
39.940	$S_1(10)$	39.977	1181
	$S_3(9)$	39.772	480
*41.615	$S_4(10)$	41.613	441
42.207	$S_6(10)$	42.279	371
	$S_7(10)$	42.630	371
	$S_8(10)$	42.254	289
	$S_9(10)$	42.277	675
	$S_{10}(10)$	42.186	208
	$S_{11}(10)$	42.188	208
	$S_K(10)$		
43.056	$S_1(11)$	43.250	456
	$S_2(11)$	42.898	442
	$S_3(10)$	43.149	480
43.667	$S_4(10)$	43.679	1030
*45.139	$S_4(11)$	45.141	937
45.885	$S_6(11)$	45.948	342
	$S_8(11)$	45.961	634
	$S_9(11)$	45.995	272
	$S_{10}(11)$	45.877	201
	$S_{11}(11)$	45.876	201
	$S_K(11)$		

[a] Relative intensities were calculated from symmetric top matrix element with $B_0 = \frac{1}{3}(B_0+C_0)$.
[b] Parentheses enclose the $\Delta\nu$ values of lines blended with grating ghosts.
NOTE: Asterisks indicate the $\Delta\nu$ values of "single transitions" used for the explicit evaluation of the rotational constants.

TABLE I (*Concluded*)

The pure rotational Raman spectrum of ethylene

$\Delta\nu$ obs.	Transition	$\Delta\nu$ calc.	I^a
46.515	$S_1(12)$	46.526	952
	$S_2(12)$	46.248	396
	$S_3(11)$	46.682	442
	$S_7(11)$	46.477	342
(47.662)	$S_8(11)$	47.567	402
*48.635	$S_4(12)$	48.649	362
49.577	$S_1(13)$	49.804	362
	$S_2(13)$	49.588	351
	$S_6(12)$	49.617	311
	$S_8(12)$	49.633	251
	$S_9(12)$	49.728	586
	$S_{10}(12)$	49.574	190
	$S_{11}(12)$	49.571	190
	$S_K(12)$		
50.256	$S_3(12)$	50.157	396
	$S_7(12)$	50.364	311
*51.418	$S_5(12)$	51.429	845
*52.128	$S_4(13)$	52.132	754
[52.506][c]			
53.196	$S_1(14)$	53.083	744
	$S_2(14)$	52.921	310
	$S_3(13)$	53.574	352
	$S_6(13)$	53.273	280
	$S_8(13)$	53.383	534
	$S_9(13)$	53.479	229
	$S_{10}(13)$	53.270	176
	$S_{11}(13)$	53.272	176
	$S_K(13)$		
*54.287	$S_7(13)$	54.290	280
[54.775]			
55.386	$S_4(14)$	55.593	286
	$S_5(13)$	55.252	323
56.342	$S_1(15)$	56.371	278
	$S_2(15)$	56.248	271
56.919	$S_3(14)$	56.929	310
	$S_6(14)$	56.917	249
	$S_8(14)$	57.134	206
	$S_9(14)$	57.248	480
	$S_{10}(14)$	56.968	160
	$S_{11}(14)$	56.977	160
	$S_K(14)$		
*58.234	$S_7(14)$	58.246	249
58.989	$S_4(15)$	59.038	585
	$S_5(14)$	59.030	667
59.641	$S_1(16)$	59.660	562
	$S_2(16)$	59.570	235
60.555	$S_3(15)$	60.239	271
	$S_6(15)$	60.546	220
	$S_8(15)$	60.812	426
	$S_{10}(15)$	60.680	144
	$S_{11}(15)$	60.689	144
	$S_K(15)$		
61.070	$S_9(15)$	61.043	183
62.281	$S_4(16)$	62.463	218
	$S_7(15)$	62.226	220
62.834	$S_1(17)$	62.953	207
	$S_2(17)$	62.886	202
	$S_5(15)$	62.760	251
*63.521	$S_5(16)$	63.516	235
64.201	$S_6(16)$	64.154	192
	$S_8(16)$	64.527	160
	$S_{10}(16)$	64.399	127
	$S_{11}(16)$	64.518	127
	$S_K(16)$		
64.876	$S_9(16)$	64.872	374
65.870	$S_4(17)$	65.867	438
66.265	$S_1(18)$	66.248	411
	$S_2(18)$	66.199	172
	$S_7(16)$	66.215	192
(66.599)	$S_3(17)$	66.769	202
	$S_6(16)$	66.431	508
67.895	$S_6(17)$	67.742	166
	$S_K(17)$		
68.154	$S_8(17)$	68.242	325
	$S_{10}(17)$	68.120	111
	$S_{11}(17)$	68.150	111
68.710	$S_9(17)$	68.731	139
69.266	$S_4(18)$	69.257	160
69.495	$S_1(19)$	69.545	149
	$S_2(19)$	69.510	145
70.075	$S_3(18)$	70.005	172
	$S_8(17)$	70.045	188
	$S_7(17)$	70.197	166
71.398	$S_6(18)$	71.306	142
	$S_K(18)$		
71.804	$S_8(18)$	71.953	120
	$S_{10}(18)$	71.846	96
	$S_{11}(18)$	71.896	96
72.673	$S_1(20)$	72.845	290
	$S_2(20)$	72.820	121
	$S_4(19)$	72.626	316
	$S_9(18)$	72.627	279
73.562	$S_3(19)$	73.239	145
	$S_8(18)$	73.592	374
*74.155	$S_7(18)$	74.158	142
[74.988]	$S_6(19)$	74.851	120
75.215	$S_K(19)$		
(75.527)	$S_8(19)$	75.654	238
	$S_{10}(19)$	75.577	82
	$S_{11}(19)$	75.658	82
(76.105)	$S_1(21)$	76.142	103
	$S_2(21)$	76.125	101
	$S_4(20)$	75.990	113
76.561	$S_3(20)$	76.476	122
	$S_9(19)$	76.563	102
*77.051	$S_6(19)$	77.071	136
78.088	$S_7(19)$	78.084	120
(78.663)	$S_6(20)$	78.370	101
[79.026]	$S_K(20)$		
79.363	$S_1(22)$	79.443	198
	$S_2(22)$	79.430	83
	$S_3(21)$	79.718	101
	$S_4(21)$	79.339	220
	$S_5(20)$	79.342	86
	$S_{10}(20)$	79.312	70
	$S_{11}(20)$	79.438	70
*80.474	$S_6(20)$	80.486	265
	$S_9(20)$	80.537	200
81.379			
81.875	$S_6(21)$	81.865	84
	$S_7(20)$	81.968	101
82.817	$S_1(23)$	82.743	69
	$S_2(23)$	82.734	68
	$S_K(21)$		
	$S_3(22)$	82.968	83
	$S_4(22)$	82.668	78
	$S_5(21)$	83.012	167
	$S_{10}(21)$	83.048	58
	$S_{11}(21)$	83.236	58
83.869	$S_8(21)$	83.837	94
(84.484)	$S_9(21)$	84.542	72
*85.312	$S_8(22)$	85.335	70
86.015	$S_1(24)$	86.042	131
	$S_2(24)$	86.036	55
	$S_4(23)$	85.998	148
	$S_7(21)$	85.799	84
86.256	$S_3(23)$	86.226	68
	$S_K(22)$		
86.676	$S_8(22)$	86.667	59
	$S_{10}(22)$	86.787	49
*87.136	$S_8(22)$	87.131	181
	$S_{11}(22)$	87.055	49
[87.811]			
88.588	$S_6(23)$	88.782	57
	$S_9(22)$	88.568	139
89.399	$S_1(25)$	89.341	45
	$S_2(25)$	89.336	44
	$S_3(24)$	89.492	55
	$S_4(24)$	89.320	51
	$S_7(22)$	89.569	70
90.296	$S_8(23)$	90.380	64
	$S_8(23)$	90.301	114
	$S_{10}(23)$	90.529	40
	$S_K(23)$		
[90.905]	$S_{11}(23)$	90.921	40
92.628	$S_1(26)$	92.638	83
	$S_2(26)$	92.635	35
	$S_3(25)$	92.762	44
	$S_4(25)$	92.630	96
	$S_6(24)$	92.211	46
	$S_9(23)$	92.619	49
[93.266]	$S_7(23)$	93.280	57
93.622	$S_8(24)$	93.599	120
	$S_K(24)$		
93.954	$S_8(24)$	93.915	40
	$S_{10}(24)$	94.265	33
94.865	$S_{11}(24)$	94.803	33
95.920	$S_1(27)$	95.936	28
	$S_2(27)$	95.934	28
	$S_3(26)$	96.038	35
	$S_4(26)$	95.941	33
	$S_6(25)$	95.617	37
96.736	$S_8(25)$	96.798	41
	$S_7(24)$	96.920	46
	$S_9(24)$	96.653	92
97.556	$S_8(25)$	97.508	74
	$S_{10}(25)$	97.986	26
	$S_K(25)$		
99.139	$S_1(28)$		51
	$S_2(28)$		22
	$S_3(27)$	99.318	28
	$S_4(27)$	99.247	26
	$S_6(26)$	99.003	30
	$S_{11}(25)$	98.724	26
[100.042]	$S_8(26)$	99.987	77
100.542	$S_7(25)$	100.485	37
	$S_9(25)$	100.662	32
[100.962]	$S_8(26)$	101.076	25
	$S_K(26)$		
102.630	$S_1(29)$		17
	$S_2(29)$		17
	$S_3(28)$		22
	$S_4(28)$		20
	$S_6(27)$	102.371	23
	$S_{11}(26)$	102.672	21

[c]Square brackets enclose the $\Delta\nu$ values of weak lines whose measured positions may be in error by more than ± 0.06 cm^{-1}

TABLE II

The pure rotational Raman spectrum of ethylene-d_4[a]

$\Delta\nu$ obs.	Transition	$\Delta\nu$ calc.	I
13.107	$S_2(4)$	13.206	1581
	$R_1(6)$	13.106	115
	$R_7(9)$	13.208	565
	$R_8(9)$	13.119	847
	$R_9(9)$	13.110	730
	$R_{10}(9)$	13.108	730
(13.683)	$S_1(4)$	13.678	2562
	$R_8(9)$	13.961	366
	$R_8(10)$	13.539	287
	$R_8(18)$	13.954	48
14.364	$S_4(4)$	14.213	1233
	$S_6(4)$	14.391	760
	$S_7(4)$	14.435	760
	$S_8(4)$	14.369	298
	$S_9(4)$	14.370	447
	$R_2(8)$	14.503	233
	$R_6(11)$	14.279	227
	$R_6(17)$	14.460	59
	$R_7(10)$	14.611	674
	$R_8(10)$	14.418	449
	$R_9(10)$	14.444	596
	$R_{10}(10)$	14.437	596
(14.977)	$S_2(4)$	15.073	1581
	$S_6(4)$	14.833	1849
	$R_6(12)$	14.813	180
	$R_6(13)$	15.128	144
	$R_6(14)$	15.230	115
	$R_6(15)$	15.135	92
	$R_6(16)$	14.867	74
15.632	$S_1(5)$	15.953	1605
	$S_2(5)$	15.548	1515
	$R_1(7)$	15.518	83
	$R_5(10)$	15.786	287
	$R_5(11)$	15.684	540
	$R_9(11)$	15.787	484
	$R_{10}(11)$	15.769	484
(16.349)	$R_7(11)$	16.068	360
16.910	$S_4(5)$	16.742	1899
	$S_6(5)$	17.024	910
	$S_7(5)$	17.126	910
	$S_8(5)$	17.002	786
	$S_9(5)$	17.006	524
	$S_{10}(5)$	16.974	194
	$S_{11}(5)$	16.975	194
	$R_2(9)$	16.810	268
	$R_5(12)$	16.868	288
	$R_9(12)$	17.180	393
	$R_{10}(12)$	17.102	393
17.651	$S_2(6)$	17.869	1445
	$S_3(5)$	17.704	1515
	$S_5(5)$	17.685	1266
	$R_5(11)$	17.796	227
	$R_7(12)$	17.632	433
(18.241)	$S_1(6)$	18.188	2268
	$R_1(8)$	17.995	62
	$R_5(13)$	17.992	348
(18.811)	$R_3(14)$	18.984	187
	$R_9(13)$	18.515	319
	$R_{10}(13)$	18.431	319
(19.100)	$S_4(6)$	19.245	1258
	$R_2(10)$	19.255	139
	$R_7(13)$	19.283	232
(19.806)	$S_5(6)$	19.657	982
	$S_7(6)$	19.862	982
	$S_8(6)$	19.643	666
	$S_9(6)$	19.654	999
	$S_{10}(6)$	19.602	364
	$S_{11}(6)$	19.603	364
	$R_3(12)$	19.990	180
	$R_8(15)$	19.808	225
	$R_9(14)$	19.917	258
	$R_{10}(14)$	19.746	258
(20.417)	$S_1(7)$	20.407	1423
	$S_2(7)$	20.172	1371
	$S_3(6)$	20.269	1445
	$S_5(6)$	20.545	1887
	$R_1(9)$	20.502	47
	$R_3(16)$	20.428	121
20.866	$R_3(17)$	20.820	147
	$R_8(19)$	20.976	78
	$R_{10}(15)$	21.036	209
21.479	$S_4(7)$	21.720	1838
	$R_3(11)$	21.811	164
	$R_7(14)$	21.077	280
	$R_8(15)$	21.367	209
22.220	$S_6(7)$	22.283	1006
	$S_8(7)$	22.294	1120
	$S_9(7)$	22.318	747
	$S_{10}(7)$	22.238	484
	$S_{11}(7)$	22.240	484
	$R_3(13)$	22.362	144
	$R_{10}(16)$	22.281	170
22.597	$S_1(8)$	22.624	2003
	$S_2(8)$	22.461	1295
	$S_3(7)$	22.756	1371
	$S_7(7)$	22.651	1006
	$R_8(16)$	22.884	170
(23.186)	$S_5(7)$	23.384	1225
	$R_1(10)$	23.006	37
	$R_7(15)$	23.054	150
23.469	$R_{10}(17)$	23.452	137
(23.897)	$S_4(8)$	24.164	1178
(24.708)	$S_1(9)$	24.847	1249
	$S_2(9)$	24.738	1217
	$S_6(8)$	24.898	1001
	$S_7(8)$	24.953	785
	$S_{10}(8)$	24.882	559
	$S_{11}(8)$	24.885	559
	$R_3(12)$	24.453	86
	$R_8(14)$	24.897	115
	$R_9(17)$	24.498	137
	$R_{10}(18)$	24.503	111
25.240	$S_5(8)$	25.156	1295
	$S_7(8)$	25.500	1001
	$S_9(8)$	25.005	1177
	$R_1(11)$	25.483	29
	$R_7(16)$	25.226	182
*26.169	$S_5(8)$	26.180	1767
	$R_3(18)$	26.241	111
27.034	$S_1(10)$	27.077	1746
	$S_2(10)$	27.007	1137
	$S_4(9)$	26.578	1681
	$R_3(13)$	27.135	103
27.433	$S_3(9)$	27.472	1217
	$S_6(9)$	27.491	975
	$S_8(9)$	27.619	1191
	$S_9(9)$	27.722	794
	$S_{10}(9)$	27.535	600
	$S_{11}(9)$	27.541	600
	$R_8(15)$	27.569	92
	$R_7(17)$	27.601	98
[28.067]	$R_1(12)$	27.925	23
(28.515)	$S_7(9)$	28.399	975
28.878	$S_4(10)$	28.962	1057
	$S_6(9)$	28.916	1121
(29.228)	$S_1(11)$	29.314	1079
	$S_2(11)$	29.269	1056
29.935	$S_2(10)$	29.720	1737
	$R_3(14)$	29.828	55
	$S_R(10)$		
30.093	$S_6(10)$	30.063	935
	$S_{10}(10)$	30.199	616
	$S_8(10)$	30.284	783
	$S_{11}(10)$	30.210	616
	$R_1(13)$	30.323	18
	$R_3(16)$	30.347	74
	$R_7(18)$	30.161	118
*30.475	$S_9(10)$	30.478	1174
31.432	$S_1(12)$	31.556	1492
	$S_2(12)$	31.528	976
	$S_4(11)$	31.317	1484
	$S_8(10)$	31.580	1585
	$S_7(10)$	31.332	935
31.801	$S_3(11)$	31.924	1056
32.698	$S_6(11)$	32.606	887
	$S_8(11)$	32.950	1136
	$S_{10}(11)$	32.871	613
	$S_{11}(11)$	32.892	613
	$R_1(14)$	32.686	14
	$R_3(15)$	32.493	65
*33.319	$S_9(11)$	33.281	757
	$R_3(17)$	33.196	59
33.836	$S_1(13)$	33.799	912
	$S_2(13)$	33.782	896
	$S_4(12)$	33.649	920
34.139	$S_3(12)$	34.106	976
	$S_6(11)$	34.158	989
	$S_7(11)$	34.268	887
35.317	$S_6(12)$	35.116	832
	$R_1(15)$	35.023	11
	$R_3(16)$	35.109	35
35.569	$S_9(12)$	35.616	722
	$S_{10}(12)$	35.554	597
	$S_{11}(12)$	35.599	597
36.045	$S_1(14)$	36.044	1249
	$S_2(14)$	36.034	818
	$S_3(13)$	36.290	896
	$S_4(13)$	35.958	1272
	$S_9(12)$	36.141	1082
	$R_3(18)$	36.077	48
36.593	$S_8(12)$	36.639	1379
37.027	$S_7(12)$	37.173	832
37.348	$S_6(13)$	37.593	774
	$R_1(16)$	37.338	9
(37.950)	$R_3(17)$	37.663	41
(38.233)	$S_1(15)$	38.292	755
	$S_2(15)$	38.286	743
	$S_3(14)$	38.481	818
	$S_4(14)$	38.250	778
	$S_8(13)$	38.260	1018
	$S_{10}(13)$	38.243	571
	$S_{11}(13)$	38.332	571
(38.742)			
39.029	$S_8(13)$	39.023	848
	$S_9(13)$	39.061	679
39.629	$R_1(17)$	39.638	7
40.005	$S_6(14)$	40.034	714
	$S_7(13)$	40.024	774
	$R_3(18)$	40.155	23

[a]Symbols and nomenclature are given in Table I.

TABLE II (*Concluded*)

The pure rotational Raman spectrum of ethylene-d_4[a]

$\Delta\nu$ obs.	Transition	$\Delta\nu$ calc.	I
40.582	$S_1(16)$	40.540	1021
	$S_2(16)$	40.536	670
	$S_3(15)$	40.686	743
	$S_4(15)$	40.529	1062
40.701	$S_9(14)$	40.880	632
41.160	$S_8(14)$	41.315	1166
	$S_{10}(14)$	40.937	539
	$S_{11}(14)$	41.095	539
*42.038	$S_9(14)$	42.030	948
	$R_1(18)$	41.928	5
*42.412	$S_6(15)$	42.441	653
42.807	$S_1(17)$	42.788	610
	$S_2(17)$	42.786	601
	$S_3(16)$	42.901	670
	$S_4(16)$	42.798	641
	$S_7(14)$	42.800	714
42.988			
43.448	$S_8(15)$	43.531	708
	$S_9(15)$	43.479	874
	$S_{10}(15)$	43.633	502
44.155	$S_{11}(15)$	43.905	502
45.055	$S_1(18)$		816
	$S_2(18)$		537
	$S_3(17)$	45.126	601
	$S_4(17)$	45.059	864
	$S_6(16)$	44.817	594
	$S_9(15)$	45.029	583
*45.701	$S_8(16)$	45.697	961
	$S_7(15)$	45.485	653
45.940	$S_8(16)$	46.046	533
46.272	$S_{10}(16)$	46.325	463
46.421			
46.969	$S_{11}(16)$	46.764	463
47.278	$S_1(19)$		482
	$S_2(19)$		476
	$S_3(18)$		537
	$S_4(18)$		515
	$S_6(17)$	47.163	536
(47.699)			
(47.897)	$S_8(17)$	47.843	576
	$S_7(16)$	48.069	594
	$S_9(16)$	48.026	800
48.466	$S_8(17)$	48.580	725
48.631			
*49.003	$S_{10}(17)$	48.994	424
49.564	$S_1(20)$		637
	$S_2(20)$		419
	$S_3(19)$		476
	$S_4(19)$		685
	$S_6(18)$		480
	$S_{11}(17)$	49.682	424
50.106	$S_8(18)$		772
*50.566	$S_7(17)$	50.546	536
*50.961	$S_8(18)$		435
	$S_9(17)$	50.984	484
51.134			
51.767	$S_1(21)$		372
	$S_2(21)$		367
	$S_3(20)$		419
	$S_4(20)$		403
	$S_6(19)$		427
	$S_{10}(18)$		383
52.511	$S_8(19)$		457
	$S_{11}(18)$		383
53.046	$S_7(18)$		480
53.645	$S_8(19)$		583
54.114	$S_1(22)$		485
	$S_2(22)$		319
	$S_3(21)$		367
	$S_4(21)$		530
	$S_6(20)$		378
54.317	$S_8(20)$		604
	$S_9(18)$		653
	$S_{10}(19)$		345
54.764	$S_{11}(19)$		345
55.122	$S_7(19)$		427
55.444			
55.733			
56.050	$S_8(20)$		345
56.405	$S_1(23)$		280
	$S_2(23)$		276
	$S_3(22)$		319
	$S_5(21)$		354
	$S_6(21)$		332
	$S_9(19)$		389
	$S_4(22)$		308
[57.207]	$S_7(20)$		378
	$S_{10}(20)$		307
57.777			
58.245	$S_8(21)$		456
58.581	$S_1(24)$		361
	$S_2(24)$		238
	$S_3(23)$		276
	$S_K(21)$		
58.763	$S_8(22)$		462
	$S_{11}(20)$		307
[59.013]			
59.336	$S_{10}(21)$		
[59.629]	$S_7(21)$		332
	$S_9(20)$		517
60.249			
60.697	$S_8(22)$		
60.893	$S_1(25)$		
	$S_2(25)$		
[61.483]			
62.042	$S_{11}(21)$		
63.093	$S_1(26)$		
63.974			
64.536			
[65.104]			
65.361	$S_1(27)$		
66.119			
(66.726)			
[67.150]			
67.564	$S_1(28)$		
67.837			
68.814			
69.238			
69.750	$S_1(29)$		
70.309			
71.154			
72.118	$S_1(30)$		
[72.750]			
73.306			
[73.574]			
74.373	$S_1(31)$		
74.946			
75.247			
(76.098)			
76.577	$S_1(32)$		
(78.837)	$S_1(33)$		
[81.128]	$S_1(34)$		
[83.331]	$S_1(35)$		
[85.651]	$S_1(36)$		

[a]Symbols and nomenclature are given in Table I.

representation of the energy levels formed the basis for the analysis of the ethylene spectra by Thompson (1939), Houston and Lewis (1933), and Gallaway and Barker (1942).

In the asymmetric top, the K degeneracy is removed: for each value of J there are $2J+1$ sublevels having energy

$$F_0(J_\tau) = \tfrac{1}{2}(A+C)J(J+1)+\tfrac{1}{2}(A-C)E_\tau^J(\kappa). \tag{2}$$

Here A, B, and C are the usual rotational constants. $E_\tau^J(\kappa)$ is a complicated function, dependent on J, on the asymmetry parameter $\kappa = (2B-A-C)/(A-C)$, and on $\tau(=K_a-K_c)$. K_a and K_c are the $|K|$ values for the limiting prolate and oblate symmetric tops. For a given J, the $2J+1$ values of $E_\tau^J(\kappa)$ are ordered according to the values of the subscript $\tau \equiv K_a-K_c = -J, -J+1, -J+2 \ldots +J$, with $\tau = -J$ assigned to the lowest level, $\tau = -J+1$ to the next lowest level, and so on.

The values of $E_\tau^J(\kappa)$ cannot be represented by an explicit formula; however, several methods of calculation are available, as well as tables which are useful for a limited range of J and κ values. In the present analysis, the tables of Townes and Schawlow (1955) for $J \leqslant 12$ with κ given in increments of 0.01 were used. For $J > 12$, the method developed by Golden (1948) was used. Golden's method gives quite accurate expressions for $E_\tau^J(\kappa)$ for those levels corresponding to the lowest τ values (for prolate tops) which satisfy the condition $(K_a/J) \ll 1$. According to the ordering of the sublevels for a given J, the sublevels with the smallest K_a values are the lowest. It is just these levels that show the greatest deviation from the symmetric top levels. Moreover, since the lowest levels will be the most highly populated, transitions from these levels will be expected to contribute the greatest intensity to the spectrum.

Golden's formulation may be summarized as follows:

$$E_\tau^J(\kappa) = \left(\frac{\kappa-1}{2}\right)J(J+1)+\left(\frac{3-\kappa}{2}\right)\alpha.$$

The quantity α is given by

$$\alpha = b-[2\theta+C_1\theta'+C_2(\theta')^2]$$

where b is the characteristic value of Mathieu's equation corresponding to 4θ,

$$\theta(J) = \tfrac{1}{2}\left|\frac{\kappa+1}{3-\kappa}\right|\left\{J(J+1)-\left[1+\frac{1}{2J(J+1)}\right]\right\}$$
$$\theta'(J) = \tfrac{1}{2}\left|\frac{\kappa+1}{3-\kappa}\right|\left[1+\frac{1}{2J(J+1)}\right], \tag{3}$$

and C_1 and C_2 are first- and second-order perturbation corrections. Values of C_1 and C_2 corresponding to $\theta = 0$ to 10 are tabulated in Golden's paper. This range of values permits the calculation of $E_\tau^J(\kappa)$ up to $J = 27$ for C_2H_4 and up to $J = 19$ for C_2D_4.

In Golden's notation, eq. (2) can be written

$$F_0(J_\tau) = CJ(J+1)+\tfrac{1}{2}(2A-B-C)[b+(2-C_1)\theta'-C_2(\theta')^2]. \tag{4}$$

For high J values the term $1/[2J(J+1)]$ in eq. (3) becomes negligible and consequently θ' approaches the value $\frac{1}{2}|(\kappa+1)/(3-\kappa)|$. Equation (4) then takes the following form:

$$F_0(J_\tau) = CJ(J+1)+\tfrac{1}{2}(2A-B-C)b+\tfrac{1}{4}(B-C)(2-C_1)-\frac{\frac{1}{4}(B-C)^2}{2A-B-C}C_2. \tag{5}$$

The expressions for $F_0(J_\tau)$ given in eq. (2) and (5) apply to the rigid rotor. The energy levels of a non-rigid asymmetric rotor correct to first order (Kivelson and Wilson 1952) may be written

$$F(J_\tau) = F_0+A_1F_0^2+A_2F_0J(J+1)+A_3J^2(J+1)^2+A_4J(J+1)\langle P_z^2\rangle +A_5\langle P_z^4\rangle+A_6F_0\langle P_z^2\rangle. \tag{6}$$

The first term, $F_0(\equiv F_0(J_\tau))$, is the energy of the rigid rotor and the remaining six terms arise from the effects of centrifugal distortion. The A_n's are constants depending on the usual rotational constants A, B, C and on the distortion constants D_J, D_{JK}, D_K, R_5, R_6, and δ_J. According to Kivelson and Wilson (1953), these distortion constants (and therefore the six coefficients A_n) can be calculated theoretically, if the rotational constants and harmonic potential constants are known. P_z is the operator for the component of angular momentum along the axis of quantization for the limiting symmetric top (the brackets indicating average values). The quantities $\langle P_z^2\rangle$ can be evaluated according to the method of Bragg and Golden (1949). In addition the approximation that $\langle P_z^4\rangle = \langle P_z^2\rangle^2$ is usually assumed.

2. Symmetry of Rotational Levels

The symmetry of a rotational level in an asymmetric top molecule is designated $++$, $+-$, $-+$, or $--$, depending on whether the rotational eigenfunction remains unchanged or changes sign for a 180° rotation of the molecule about the twofold axes c and a of the momental ellipsoid. That is, the first sign refers to the operation C_2^c and the second to C_2^a. Dennison (1931) has given general rules for determining the symmetry of any level and Wilson (1935) has shown that the statistical weight factors for $++$, $+-$, $-+$, $--$ of $C_2{}^{12}H_4$ are 7:3:3:3 and of $C_2{}^{12}D_4$ are 27:18:18:18.

3. Selection Rules for Rotational Transitions

Since the ethylene molecule has the plane symmetric form (point group V_h), it has no permanent dipole moment and, consequently, it cannot exhibit a pure rotational spectrum in the microwave or infrared regions. However, it does have a pure rotational Raman spectrum.

According to Placzek and Teller (1933) the Raman selection rule for rotational transitions of an asymmetric top is

$$\Delta J = 0, \quad \pm 1, \quad \pm 2. \tag{7}$$

However, there may be further restrictions on account of the symmetry of

the polarizability ellipsoid. For example, in C_2H_4 and C_2D_4 the polarizability ellipsoid has the same symmetry as the momental ellipsoid and therefore Raman transitions can take place only between levels of the same symmetry, that is

$$(8) \qquad ++ \leftrightarrow ++,\ +- \leftrightarrow +-,\ -+ \leftrightarrow -+,\ -- \leftrightarrow --.$$

Since the ethylene molecule deviates only slightly from a symmetric top, one might expect that the quantum number $K(\equiv K_a)$ will be approximately defined and that selection rules for K_a might be applicable. For a symmetric top (where of course K is a good quantum number) the selection rule for pure rotational Raman transitions is $\Delta K = 0$. Classically this is due to the fact that the polarizability ellipsoid is cylindrically symmetric about the figure axis. For an asymmetric top, in general, the three principal axes of the polarizability ellipsoid would be unequal and Raman transitions with $\Delta K_a \neq 0$ would also be allowed. With $\Delta J = 0$ the selection rule would be $\Delta K_a = \pm 2$, the transition for which $\Delta K_a = \pm 1$ being forbidden by the selection rule given in (8). Transitions with $\Delta K_a = 0$ would be the most probable and the intensity of transitions for which $\Delta K_a = \pm 2$ would depend on the magnitude of the difference of the two polarizability components perpendicular to the limiting symmetric top axis. Also according to the symmetric top approximation and the value $I_A/I_B \sim 0.2$ for C_2H_4 and $I_A/I_B \sim 0.3$ for C_2D_4, the S branches would be expected to have considerably higher intensity than the R branches.

4. Equations for Raman Lines

With the selection rules, eq. (7) and (8), it can be shown that the S branches ($\Delta J = 2$, $\Delta K_a = 0$) and R branches ($\Delta J = 1$, $\Delta K_a = 0$) fall into a number of series. The designation for these series is given in Table III along with the usual J_{K_a,K_c} notation. In the symmetric top limit all the S branches

TABLE III

Nomenclature for R and S branches

Branch	Transition		Selection rules
$S_{2n+1}(J)$	$J'_{n,J'-n} \leftarrow J_{n,J-n}$	$n = 0, 1, 2, \ldots . J$	$\Delta J = 2; \Delta K_a = 0$
$S_{2n}(J)$	$J'_{n,J'-n+1} \leftarrow J_{n,J-n+1}$	$n = 1, 2, 3, \ldots . J$	$\Delta J = 2; \Delta K_a = 0$
$R_{2n-1}(J)$	$J'_{n,J'-n} \leftarrow J_{n,J-n+1}$	$n = 1, 2, 3, \ldots . J$	$\Delta J = 1; \Delta K_a = 0$
$R_{2n}(J)$	$J'_{n,J'-n+1} \leftarrow J_{n,J-n}$	$n = 1, 2, 3, \ldots . J$	$\Delta J = 1; \Delta K_a = 0$

would coincide to give a single series of lines with a uniform spacing of $4B_0$. Likewise all of the R branches would also coincide to give another series with a uniform spacing of $2B_0$.

The expressions for the wave number displacements of the R and S branch lines are obtained by applying the selection rules, $\Delta J = 1, 2$; $\Delta K_a = 0$, to the equations for the energy levels, eq. (2):

$$(9) \qquad \begin{aligned} \Delta\nu_R = R(J) &= (A+C)(J+1)+\tfrac{1}{2}(A-C)[E_{\tau'}{}^{J+1}(\kappa)-E_\tau{}^J(\kappa)], \\ \Delta\nu_S = S(J) &= (A+C)(2J+3)+\tfrac{1}{2}(A-C)[E_{\tau'}{}^{J+2}(\kappa)-E_\tau{}^J(\kappa)]. \end{aligned}$$

For high τ (or K_a) values and slight asymmetry, the above equation can be approximated very closely by the symmetric top expansion:

$$\Delta\nu_R = (B+C)(J+1),$$
$$\Delta\nu_S = 2(B+C)(J+3/2). \tag{10}$$

For low and intermediate τ (or K_a) values and high J eq. (10) is not suitable and one must use the asymmetric top expressions. From eq. (5) the equation for the S branches takes on the following form:

$$\Delta\nu_S = C(4J+6)+\tfrac{1}{2}(2A-B-C)(b'-b)-\tfrac{1}{4}(B-C)(C_1'-C_1) - \frac{(B-C)^2}{4(2A-B-C)}(C_2'-C_2) \tag{11}$$

where the primed quantities refer to the upper state and the unprimed to the lower state of the transition. For low K_a and sufficiently high J the quantity $(b'-b) = \Delta b$ approaches a constant value. This happens to each of the series in pairs, first in S_1 and S_2 and then (as J becomes higher) in all the other series S_3 and S_4, then S_5 and S_6 . . . , and so on. The values of Δb for large J can be easily obtained from Tables Relating to Mathieu Functions (1951). From Golden's work a similar situation seems to occur for the differences $(C_1'-C_1) = \Delta C_1$ and $(C_2'-C_2) = \Delta C_2$. Approximate values are found by extrapolation. The term containing ΔC_2 turns out to be quite small ($\sim 10^{-3}$ cm^{-1}) for C_2H_4 and C_2D_4 and can be neglected. With this approximation eq. (11) can be written

$$\Delta\nu_S = C(4J+6)+\tfrac{1}{2}(2A-B-C)\Delta b-\tfrac{1}{4}(B-C)\Delta C_1. \tag{12}$$

The general behavior of the S branches can now be inferred from equations (10), (11), and (12), for a slightly asymmetric molecule. First of all there should be a series of rather broad lines with a spacing of $2(B_0+C_0)$ corresponding to the S branch lines for large K_a eq. (10). For low J values the S branches belonging to the lower K_a values will at first follow the $2(B_0+C_0)$ spacing but as J increases they will "break off" (lowest K_a values first) gradually increasing and/or decreasing their spacing until they have a spacing of $4C_0$ as given in eq. (12). This behavior is shown (exaggerated) for the first six S branches in Fig. 3.

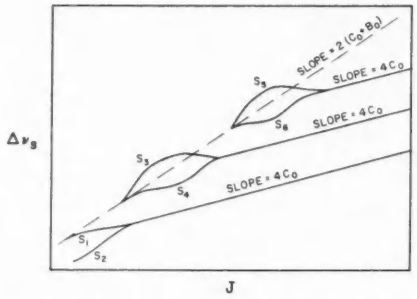

FIG. 3. The behavior of the S branches for a slightly asymmetric top. (The scale for $\Delta\nu_s$ has been exaggerated.)

D. ANALYSIS

1. Determination of Rotational Constants

The analysis of the observed spectra was carried out as follows. First an approximate spectrum was calculated using preliminary values of the rotational constants. (The constants reported by Romanko *et al.* were used as the constants obtained by Allen and Plyler were not yet available.) The small effects due to centrifugal distortion were also included. These were calculated from the force constants given by Crawford, Lancaster, and Inskeep (1953). By means of these approximate spectra it was possible to assign almost all the lines in the C_2H_4 spectrum and most of those in the C_2D_4 spectrum. (Allen and Plyler's constants were used to calculate the first C_2D_4 spectrum as this analysis was carried out after their work was published.) Most of the observed lines were found to be blends, that is due to the superposition of lines arising from several transitions. However, 14 lines in the spectrum of C_2H_4 and 9 in that of C_2D_4 were found to be due to single transitions. All were *S* branch lines. These lines were then used to determine the rotational constants making use of eq. (9).

Equation (9) gives the displacement of *S* branch lines in terms of three unknowns, A, C, and κ. Direct solution of this equation is not possible since κ does not appear explicitly. Therefore the following procedure was adopted. For each of the single transitions the quantities $[E_{\tau'}{}^{J+2}(\kappa)-E_{\tau}{}^{J}(\kappa)]$ were calculated for various assumed values of κ. The equations for $\Delta\nu$ were then taken in pairs (each consisting of two different single transitions) to eliminate A. The resulting equations then contained C alone for the various values of κ. This permitted the determination of a value for C as a function of κ, consistent with the observed $\Delta\nu$ for each pair of lines. Graphs of these relations are given in Fig. 4 for C_2H_4 and in Fig. 5 for C_2D_4. Ideally all curves should intersect at one point whose co-ordinates will be C and κ. However, due to experimental errors the curves of Figs. 4 and 5 intersect at several points, although the intersections are in close proximity. Values of κ were determined by averaging all intersections except those between curves that were almost parallel. The values are given in Table IV. Errors of twice the average deviation were assigned. These errors correspond to errors of 0.02 cm^{-1} in the measurement of less sensitive lines and of 0.04 cm^{-1} for the more sensitive

TABLE IV

Ground state rotational constants (cm^{-1}) and asymmetry parameters of C_2H_4 and C_2D_4

	C_2H_4			C_2D_4	
	Raman, present results	Raman, Romanko *et al.*	Infrared, Allen and Plyler*	Raman, present results	Infrared, Allen and Plyler*
A_0	4.828±0.009	4.66±0.20†		2.432±0.008	
B_0	1.0012±0.0009	1.008_5±0.006	0.9998	0.7369±0.0012	0.7334
C_0	0.8282±0.0004	0.828_9±0.002†	0.8294	0.5630±0.0006	0.5636
κ	−0.9135±0.0003			−0.8139±0.0005	

*Allen and Plyler report errors of about ±0.0002 cm^{-1} for C_2H_4 constants and somewhat larger errors for C_2D_4.
†Deduced from $1/A_0 = 1/C_0 - 1/B_0$.

lines. With κ evaluated it was then a simple procedure to recalculate the values of $[E_{\tau'}{}^{J+2}(\kappa) - E_{\tau}{}^{J}(\kappa)]$ for the single transitions and to solve for A_0 and C_0. The constant B_0 was then calculated from $\kappa = (2B - A - C)/(A - C)$.

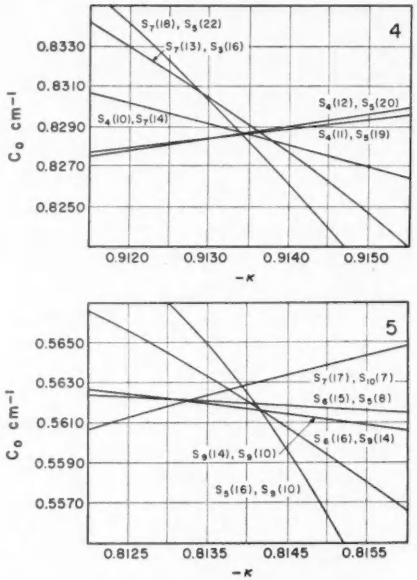

FIG. 4. Determination of κ for C_2H_4.
FIG. 5. Determination of κ for C_2D_4.

The rotational constants of C_2H_4 and C_2D_4 are given in Table IV. Larger relative errors are quoted for the constants of C_2D_4 since fewer lines were available for the analysis of the C_2D_4 spectrum. It will also be noted that the values of C_0 quoted in Table IV differ slightly from those obtained from the graphs of C_0 vs. κ (Figs. 4 and 5) but are considered to be more accurate than the latter. For comparison, the rotational constants reported by Allen and Plyler (1958) and by Romanko, Feldman, Stansbury, and McKellar (1954) are included in Table IV. The final values of the calculated centrifugal distortion constants are given in Table V.

TABLE V

Calculated values* of the centrifugal distortion constants for C_2H_4 and C_2D_4

	C_2H_4, cm^{-1}	C_2D_4, cm^{-1}
D_J	1.143×10^{-6}	6.651×10^{-7}
D_{JK}	2.148×10^{-5}	5.822×10^{-6}
D_K	7.960×10^{-5}	1.916×10^{-5}
R_5	-5.028×10^{-6}	-1.634×10^{-6}
R_6	-1.788×10^{-6}	-2.249×10^{-6}
δ_J	2.112×10^{-7}	1.961×10^{-7}

*The number of significant figures shown is not justified, but was used to secure internal consistency in the calculations.

2. *Discussion of the Analysis and Its Limitations*

Since the values of the constants given in Table IV were obtained from an analysis of a small fraction of each of the observed spectra, it would be most desirable to confirm these values from the remainder of the spectra.

An independent check of the value of C_0 can be made according to eq. (12) from lines of low K_a and high J. A graph of $\Delta\nu_S$ vs. J should give a straight line (at high J) with a slope of $4C_0$ and with an (extrapolated) intercept of $6C_0+\frac{1}{2}(2A-B-C)\Delta b-\frac{1}{4}(B-C)\Delta C_1$. It is found that for $J > 13$ the points lie on a straight line. The straight line portions of the curves for C_2H_4 and C_2D_4 are shown in Figs. 6 and 7. These have been shown on a larger scale by removing some of the slope with a plot of $\Delta\nu-3n$ for C_2H_4 and $\Delta\nu-2n$ for C_2D_4. The

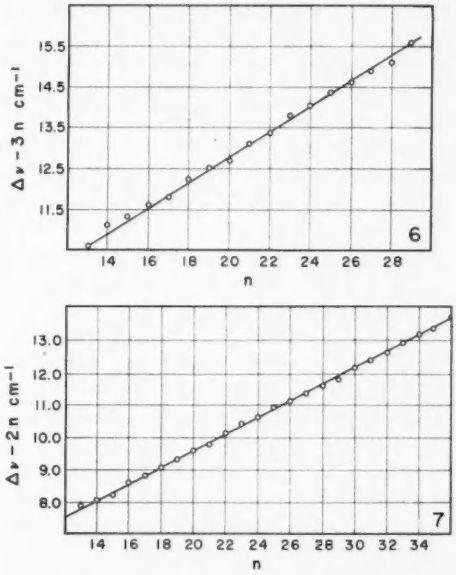

FIG. 6. $\Delta\nu_s$ vs. n for C_2H_4, where $n = J$ for the S_1 and S_2 series; $n = J-1$ for the S_3 and S_4 series; . . . (In order to provide a larger scale $3n$ cm^{-1} has been subtracted from each $\Delta\nu$ value.)

FIG. 7. $\Delta\nu_s$ vs. n for C_2D_4, where $n = J$ for the S_1 and S_2 series; $n = J-1$ for the S_3 and S_4 series; . . . (In order to provide a larger scale $2n$ cm^{-1} has been subtracted from each $\Delta\nu$ value.)

running number n on the abscissa is J for the S_1 and S_2 series, $J-1$ for the S_3 and S_4 series, and so on (see Tables I and II). From these graphs values of $C_0(C_2H_4) = 0.8279\pm0.0009$ cm^{-1} and $C_0(C_2D_4) = 0.5634\pm0.0007$ cm^{-1} were obtained, in excellent agreement with those in Table IV. Also good agreement was found for the intercepts: the observed values are 6.55 ± 0.07 cm^{-1} and 4.49 ± 0.03 cm^{-1} for C_2H_4 and C_2D_4, respectively, which may be compared with the calculated values of 6.60 cm^{-1} and 4.47 cm^{-1}.

In the earlier work of Romanko *et al.* (1954) an expression similar to eq.

(12) was used for the analysis of the S' lines (that is the asymmetric top lines). It was derived from equations given by Mecke (1933) for the limiting *oblate* top. Nevertheless, it was shown to be a fairly good approximation for C_2H_4 and led to a value of $C_0 = 0.828_9 \pm 0.002_7$ cm^{-1} in agreement with the value reported here within the quoted error.

A final test of the validity of the constants given in Table IV was made by calculating the spectra and by comparing them with the observed spectra. The results are given in column 3 of Tables I and II. In column 4 of the tables are listed the approximate relative intensities of the calculated transitions. These are based on the matrix elements of the polarizability for the symmetric top (Placzek and Teller 1933) with $B = \frac{1}{2}(B_0+C_0)$ and on the statistical weights given in Section C(2). For C_2H_4 the over-all agreement between observed and calculated $\Delta\nu$ is good. In particular for those lines which were subsequently found to be due to single transitions, and were not used in the analysis, the agreement is within the experimental error of ± 0.03 cm^{-1}. Furthermore, it was possible to assign all but four of the lines in the C_2H_4 spectrum. An indication of the good agreement can also be obtained from Fig. 2 where the calculated spectrum is drawn beneath the microphotometer trace. For C_2D_4, however, the over-all agreement is not as good and moreover many of the lines remain unassigned. The reasons for this are discussed below.

As just mentioned, all but four of the lines in the spectrum of C_2H_4 were assigned with the constants of Table IV and with the selection rules $\Delta J = 1, 2$; $\Delta K_a = 0$. One of the unassigned lines, however, might possibly arise from a transition with $\Delta K_a = 2$. This line is weak and sharp (see Fig. 2) and was measured on three plates with an average $\Delta\nu = 33.97_5$ cm^{-1}. It lies at the calculated position ($\Delta\nu = 33.980$ cm^{-1}) of the transition $7_{35} \leftarrow 7_{17}$, and in this region all other lines of appreciable intensity have been accounted for. All of the other transitions with $K_a = 3 \leftarrow 1$ (as well as $K_a = 2 \leftarrow 0$) led to calculated $\Delta\nu$ very close to R, S, or ghost lines. Similarly, transitions with $\Delta K_a = 2$ amongst the higher K_a levels gave lines in crowded regions of the spectrum and unfortunately none were detected. Such lines would be expected to be less intense because of the Boltzman factor. If the assignment of the above line could be established as $7_{35} \leftarrow 7_{17}$, it would serve as a critical check on the value of A_0 since the $\Delta\nu$ for transitions with $\Delta K_a = 2$ are mainly dependent on A_0.

The most serious limitation in the preceding analysis is probably the fact that only the 11 lowest τ levels* (corresponding to $K_a \leqslant 5$) could be calculated. Moreover, these were restricted to $J \leqslant 27$ for C_2H_4 and $J \leqslant 19$ for C_2D_4. The next τ levels and therefore the next S branches would correspond to $K_a \geqslant 6$. These branches are undoubtedly present in the spectrum of C_2D_4 and to a lesser extent in that of C_2H_4, but with less intensity than

*In Golden's paper the second-order corrections (C_2) are given for only the eight lowest τ levels. The next three τ levels were calculated with the assumption $C_2 = 0$. This approximation did not produce serious difficulties since it appears that the correction involving C_2 is almost the same for all energy levels giving rise to a specific S branch and therefore contributes very little to any given $\Delta\nu$.

the first 11 S branches. As pointed out before, the energy levels of intermediate and high τ levels are expected to show little deviation from the limiting symmetric top levels (for small asymmetry), and transitions between these levels would give rise to a series of broad lines with a spacing of $2(B_0+C_0)$, according to eq. (10). Such a series of lines was indeed found in the C_2H_4 spectrum and it is labelled as S_K in Table I and Fig. 2. Some lines of the corresponding R_K series were also evident. While some of the lines in the C_2D_4 spectrum can be assigned as S_K lines, their identification is not unambiguous and the series cannot be followed to the end of the spectrum. This was not unexpected in view of the larger asymmetry of the C_2D_4 molecule. There is no doubt that the contribution of transitions amongst the τ levels higher than 11 is mainly responsible for the large number of unassigned, and apparently "misfitted", lines in the C_2D_4 spectrum. It is also quite possible that some of the lines chosen as single transitions are overlapped by weak lines arising from these τ levels and again this occurrence would be more likely for C_2D_4.

Finally it should be mentioned that a few of the lines selected as single transitions on the basis of the approximate spectrum were found to be overlapped by weaker R or S branch lines as indicated in Tables I and II. These weaker lines were so sensitive to the changes in rotational constants that their final calculated positions were shifted, by appreciable amounts, to within $\pm 0.2\ \text{cm}^{-1}$ of the lines used in the analysis. However, the neglect of these few lines would not alter the analysis or constants of Table IV to any appreciable extent.

E. STRUCTURE OF THE ETHYLENE MOLECULE

The principal moments of inertia of C_2H_4 and C_2D_4 and the inertial defects $\Delta = I_C - I_A - I_B$ are given in Table VI. (The small positive values of the inertial defects indicate the planar structure of the molecules.) The three

TABLE VI

Ground state moments of inertia and inertial defects for ethylene and ethylene-d_4, and the structural parameters of the ethylene molecule

Constant	C_2H_4	C_2D_4
I_A^0	3.493±0.007 a.m.u. Å²	6.934±0.023 a.m.u. Å²
I_B^0	16.843±0.015	22.884±0.037
I_C^0	20.361±0.010	29.952±0.032
Δ	0.025±0.020	0.134±0.054

	r_0(C=C)	r_0(C—H)	∠H—C—H
Raman	1.339±0.002 Å	1.086±0.003 Å	117°34′±30′
Infrared	1.337±0.003	1.086±0.003	117°22′±1°
Electron diffraction	1.334±0.003	1.085±0.005	116°±1°

structural parameters of ethylene can be determined from the present data by making the assumption that the structures of C_2H_4 and C_2D_4 are identical in the $v = 0$ vibrational levels. This assumption of course neglects the small

effects of zero-point vibrations. Only three independent moments of inertia are necessary for this determination and the values $I_C^0(C_2H_4)$, $I_C^0(C_2D_4)$, and the average of the two values I_A^0 were used. (The values of I_B^0 were not used in the present work in view of their much larger errors.) The resulting parameters are given in Table VI. For comparison, the recent values obtained by Bartell and Bonham (1957) by electron diffraction and those obtained by Allen and Plyler (1958) by infrared spectroscopy are included in this table.

The three sets of parameters for ethylene as determined by these three different experiments are essentially the same. The three sets appear to have the same accuracy and are considerably more accurate than all the previous determinations of the ethylene structure. All three parameters differ significantly from earlier values with perhaps the change in HCH angle from 120° to 117° being the most striking.

It would appear from Table V that the Raman and infrared values are in closer agreement; however, the apparent small difference between the spectroscopic and electron diffraction values may not be significant because of the effects of zero-point vibrations. Of course these effects enter into both types of measurements, but they do so in different ways and could result in small differences in the structures. An attempt to include these effects was made in the case of the electron diffraction results, but this is not yet possible for the spectroscopic results.

In the spectroscopic determination of molecular structures from ground state constants of isotopic molecules, it is well known that zero-point vibration effects may yield several slightly different sets of values for the parameters, depending on the isotopic molecules used in the calculation. Recently, Costain (1958) has demonstrated that a consistent set of parameters can be obtained from ground state constants by using isotopic substitution on all non-equivalent atoms. This leads to the so-called "r_s structure" which appears to approach more nearly the equilibrium structure than does the "r_0 structure" obtained from the usual calculations. In principle r_0 structures are determined directly from the experimentally determined moments of inertia, whereas r_s structures are determined from *differences* between moments of inertia. The determination of the "r_s structure" of ethylene requires the substitution of at least one C^{12} atom by a C^{13} atom, as well as the H—D substitution.* The present data therefore only allow the calculation of the H—H distances in ethylene: however, these data do permit the calculation of r_s(C—H) and ∠HCH for various assumed values of r_s(C=C). The results are given in Table VII. Clearly the C—H parameters are insensitive to the assumed range of C=C bond lengths. This perhaps indicates little or no real discrepancy between the spectroscopic and electron diffraction results.

*The next best procedure would be to study the spectrum of $D_2C = CH_2$ (C_{2v} symmetry) and to make use of the first moment equation to determine the shift in the center of mass along the C_2 axis and to evaluate the C=C bond length.

TABLE VII

The "r_s" structure of ethylene

r_s(C=C) (assumed), Å	r_s (C—H), Å	∠H—C—H
1.335	1.085	116°50′
1.337	1.084	116°54′
1.339	1.084	117°0′

ACKNOWLEDGMENT

We are grateful to Dr. L. C. Leitch for preparing the samples of deuterated ethylene.

REFERENCES

ALLEN, H. C. and PLYLER, E. K. 1958. J. Am. Chem. Soc. **80**, 2673.
BARTELL, L. S. and BONHAM, R. A. 1957. J. Chem. Phys. **27**, 1414.
BRAGG, J. K. and GOLDEN, S. 1949. Phys. Rev. **75**, 735.
COSTAIN, C. C. 1958. J. Chem. Phys. **29**, 864.
CRAWFORD, B. L., LANCASTER, J. E., and INSKEEP, R. G. 1953. J. Chem. Phys. **21**, 678.
DENNISON, D. M. 1931. Revs. Modern Phys. **3**, 280.
GALLAWAY, W. S. and BARKER, E. F. 1942. J. Chem. Phys. **10**, 88.
GOLDEN, S. 1948. J. Chem. Phys. **16**, 78.
KIVELSON, D. and WILSON, E. B., Jr. 1952. J. Chem. Phys. **20**, 1575.
——— 1953. J. Chem. Phys. **21**, 1229.
LEWIS, C. M. and HOUSTON, W. V. 1933. Phys. Rev. **44**, 903.
MECKE, R. 1933. Z. Physik, **81**, 313.
MULLIKEN, R. S. 1955. J. Chem. Phys. **23**, 1997.
PLACZEK, G. and TELLER, E. 1933. Z. Physik, **81**, 209.
ROMANKO, J., FELDMAN, T., STANSBURY, E. J., and MCKELLAR, A. 1954. Can. J. Phys. **32**, 735.
STOICHEFF, B. P. 1954. Can. J. Phys. **32**, 330.
TABLES RELATING TO MATHIEU FUNCTIONS. 1951. The Computer Laboratory of the National Applied Mathematics Laboratory, National Bureau of Standards.
THOMPSON, H. W. 1939. Trans. Faraday Soc. **35**, 697.
TOWNES, C. H. and SCHAWLOW, A. L. 1955. Microwave spectroscopy, Appendix IV (McGraw-Hill Book Co., Inc., New York).
WILSON, E. B., Jr. 1935. J. Chem. Phys. **3**, 276.

PHOTO ALPHA REACTIONS IN SILVER[1]

J. P. ROALSVIG, R. N. H. HASLAM, L. D. SKARSGARD,[2] AND E. E. WUSCHKE[3]

ABSTRACT

The reaction $Ag^{109}(\gamma, \alpha)Rh^{105}$ has been investigated by using the secondary activity of Rh^{105}. Statistical theory was used to obtain information about the reactions $Ag^{107}(\gamma, \alpha)Rh^{103}$ and $Ag(\gamma, \alpha)Rh$. The present values for the absolute yield and cross section are in agreement with previous work using either the secondary activity or photographic plates.

I. INTRODUCTION

Photo alpha reactions in silver have been investigated both by measurement of the secondary activity of the daughter nucleus (Greenberg *et al.* 1954; Laboulaye and Beudon 1954; Schmouker *et al.* 1955; Erdös *et al.* 1955; Erdös 1957) and by photographic plate work (Greenberg 1957; Toms *et al.* 1958). The fact that the yield values, and consequently also the cross-section values, measured previously at this laboratory by the secondary activity method (Greenberg *et al.* 1954), are much lower than values obtained at other laboratories by the same method and also all values obtained from plate work suggests that our previous values are in error. It is probable that the chemical separation used to isolate the radioactive Rh^{105} from the irradiated silver was unsatisfactory. It was thus thought worth while to re-examine the reaction $Ag^{109}(\gamma, \alpha)Rh^{105}$ using improved techniques. Another factor making this experiment desirable is the recent redetermination of the activation curve for the reaction $Ni^{58}(\gamma, n)Ni^{57}$ (Roalsvig, Haslam, and McKenzie 1959), which was used as a standard for normalization of the rhodium yield.

II. EXPERIMENTAL TECHNIQUE

1. Irradiation

The samples, consisting of 80 g of $AgNO_3$, were irradiated in a cylindrical lucite container, 5 cm long and 3 cm in diameter. The cylinder was placed in a special holder close to the target of the betatron donut, so that the X-ray beam passed along its axis. Thin nickel disks of the same thickness and diameter were used as monitors and were fastened to the front and back of the container. The samples were irradiated at different maximum photon energies of the betatron, ranging from 15.5 Mev to 24.0 Mev. The irradiation time ranged from 3 hours at 15.5 Mev to 45 minutes at 24.0 Mev.

2. Separation Method

At the end of the irradiation period, the rhodium formed in the reaction $Ag(\gamma, \alpha)Rh$ was separated from the silver nitrate by the following chemical procedure:

[1]Manuscript received March 9, 1959.
Contribution from Physics Department, University of Saskatchewan, Saskatoon, Saskatchewan.
[2]Present address: Physics Department, University of Toronto, Toronto, Ontario.
[3]Present address: Atomic Energy of Canada Limited, Chalk River, Ontario.

The silver nitrate was dissolved in 100 ml of distilled water and 10 ml of Fe^{3+} carrier solution (containing 9.64 mg of Fe^{3+} per ml) were added. This was then precipitated with 10 ml of NH_4OH, filtered, and washed with distilled water. After dissolution of the precipitate in HNO_3, a similar separation was carried out again, adding another 10 ml of Fe^{3+} carrier and precipitating and washing with NH_4OH. After filtration, the precipitate was again dissolved in HNO_3 and a similar procedure carried out for the third time, this time adding 20 ml of Fe^{3+} and precipitating with 50 ml of HN_4OH. After filtration, the final precipitate was dried and ignited to Fe_2O_3.

3. Counting Procedure

The final precipitates were counted between two Geiger–Müller counters placed end to end to secure higher counting efficiency. The nickel monitor disks were also counted, the front one before and the back one after each rhodium count. The counting rates were corrected to the mid-point of the rhodium counting interval by application of the appropriate exponential correction for decay. The samples were followed through several half-lives.

4. Correction Factors

(*a*) *Geometry and Backscattering*

The samples were all counted in the same geometry, so no correction for different geometry factors was necessary. Also, the samples were mounted on a very thin *Q*-film, making corrections for backscattering negligible.

(*b*) *Self-absorption*

The observed counting rates were corrected for self-absorption in the samples, using the formula for self-absorption of Baker and Katz (1953).

(*c*) *Half-lives*

If the half-lives of Rh^{105} and Ni^{57} are the same, the ratio of rhodium to nickel counts should remain constant for samples irradiated together. The ratio was measured through several half-lives, and was found to be constant as expected.

(*d*) *Efficiency of Powder versus Disk*

The counting efficiency of powder is lower than that of the disks, that is, if equal masses of nickel powder and nickel disk are given the same dose in identical geometry, the observed activity will be higher for the disk than for the powder, counted in identical geometry. A test of the relative counting efficiency of nickel powder and nickel disks was made, and the ratio obtained was used in the analysis of the results to correct for this effect.

(*e*) *Relative Doses*

Method I: Samples of $AgNO_3$, into each of which had been uniformly mixed 1 g of nickel powder, were given 15-minute irradiations in the same position as was used for the other samples. Nickel disks were again mounted in front of and behind the samples. After irradiation the nickel powder was removed by dissolving the sample in water and mechanically filtering out the nickel. A mass of powder equal to the mass of each of the front and rear disks was weighed out, and alternate counts were taken on the activities of the

powder and the disks. After correcting for the effect (*d*), the dose given to the powder, and consequently to the silver nitrate, was related to the dose given to the two monitor disks.

Method II: Measurements of the ratio of the activities in the front and rear nickel detectors showed that this ratio remained constant over the range of energies used in this work. That indicates that the effect of beam spreading with energy is largely balanced by changes in the beam absorption with energy. The beam was therefore assumed to be absorbed in an exponential manner in passing through the sample. In this case $N_b = N_t e^{-\mu' L}$ where

N_b = dose given to back detector,
N_t = dose given to front detector,
μ' = effective linear absorption coefficient,
L = length of sample.

Experimental values gave $\mu' = 0.168$ cm^{-1}. The average dose given to the $AgNO_3$ sample was then calculated from

$$N_{av} = \frac{\int_0^L N_t e^{-\mu' x} dx}{L}.$$

The relative doses, as measured by methods I and II, were in good agreement.

(*f*) *Chemical Separation*

Correction should also be made for the percentage recovery of iron in the chemical separation; 40 ml of $Fe(NO_3)_3$ solution were introduced, containing 9.64 mg of Fe^{3+} per milliliter. Thus if all iron were recovered, the mass of iron should be 386 mg. If the precipitate is in the form of Fe_2O_3 after oxidation, its mass should be 552 mg. On the other hand, if the iron is present as FeO, the mass of the precipitate should be 497 mg. The actual masses were found to be between 510 and 550 mg. Thus the calculated percentage yield range from a minimum of 93% to a maximum of 110% depending on the assumption made about the form in which the iron is present. The precipitates did differ in color, indicating incomplete oxidation in some cases. Thus it is impossible to determine the actual chemical yield, and the best assumption seems to be to take 100% as the yield.

(*g*) *Isotopic Abundance*

The counting rates were corrected for the abundance of the isotopes Ag^{109} and Ni^{58}.

III. RESULTS

1. Activation Curve

After application of the above-mentioned correction factors, the ratio of the yield in α-particles per roentgen per mole Ag^{109} to the yield in neutrons per roentgen per mole Ni^{58} was found as a function of the maximum betatron energy. In order to find the absolute yield values for the $Ag^{109}(\gamma, \alpha)Rh^{105}$ reaction, the absolute yield values for $Ni^{58}(\gamma, n)Ni^{57}$ must be known. The activation curve for the latter reaction has recently been redetermined at this

laboratory (Roalsvig, Haslam, and McKenzie 1959). Using the values taken from this work, the absolute activation curve for $Ag^{109}(\gamma, \alpha)Rh^{105}$ was calculated and is given in Fig. 1. The absolute yield value at 23 Mev was found to be 970 α/r mole.

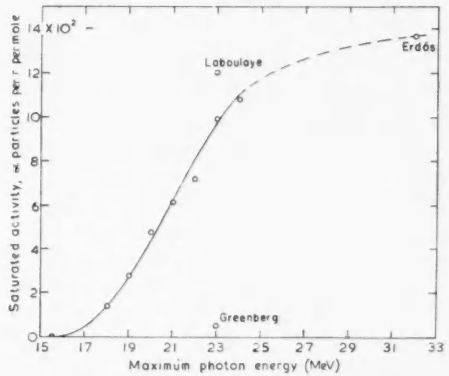

FIG. 1. Absolute yield curve for the reaction $Ag^{109}(\gamma, \alpha)Rh^{105}$. Also given are the yield values of Laboulaye and Beudon, and Greenberg *et al.* at 23 Mev, and of Erdös *et al.* at 32 Mev.

2. Cross-section Curve

The cross-section curve was calculated from the activation curve by using the method of Penfold and Leiss (1958), and is given in Fig. 2 (solid curve).

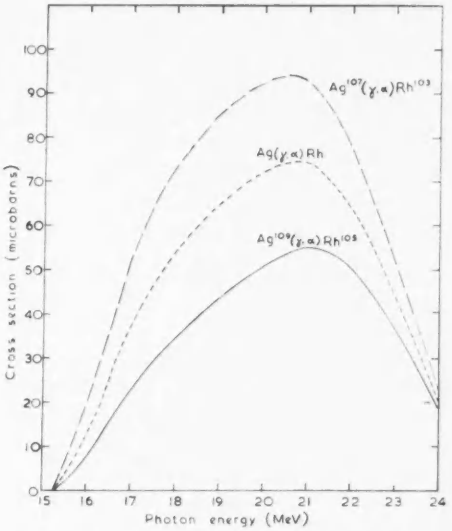

FIG. 2. Cross-section curves for the reactions $Ag^{109}(\gamma, \alpha)Rh^{105}$, $Ag^{107}(\gamma, \alpha)Rh^{103}$, and $Ag(\gamma, \alpha)Rh$.

The characteristic values are:

$$\sigma_m = 55\ \mu b$$
$$E_m = 21.0\ \text{Mev}$$
$$\Gamma_{\frac{1}{2}} = 6.1\ \text{Mev}$$
$$\int_0^{24\ \text{Mev}} \sigma dE = 0.31\ \text{Mev.mb.}$$

3. The Reaction $Ag^{107}(\gamma, \alpha)Rh^{103}$

This reaction cannot be measured by secondary activity since the daughter nucleus Rh^{103} is stable. However, by using the statistical theory, the cross-section curve for this reaction might be determined when the cross-section curve for the reaction $Ag^{109}(\gamma, \alpha)Rh^{105}$ is known.

For two neighboring isotopes such as Ag^{109} and Ag^{107}, the cross sections for γ-capture are almost equal. Also the sums $\sum F_i$ of the half-widths covering all modes of decay of the excited nuclei must be equal. We thus have (Blatt and Weisskopf 1952, Chapter VIII):

$$\frac{\sigma(\gamma, \alpha)_{(1)}}{\sigma(\gamma, \alpha)_{(2)}} = \frac{F_{\alpha(1)}}{F_{\alpha(2)}} = \frac{I_{\alpha(1)}}{I_{\alpha(2)}}, \qquad I_\alpha = K \int_{E_\alpha=0}^{h\nu-Q} E_\alpha \omega(\epsilon) \sigma_{\alpha c} dE_\alpha$$

where

K = a constant

$\omega(\epsilon)$ = the level density of the residual nucleus at an energy ϵ, where $\epsilon = h\nu - Q - E_\alpha$

Q = the binding energy of the alpha particle

$\sigma_{\alpha c}$ = the capture cross section for the alpha particle of energy E_α by the residual nucleus.

The ratio $\{\sigma(\gamma, \alpha)Ag^{107}\}/\{\sigma(\gamma, \alpha)Ag^{109}\}$ has been calculated by Greenberg (1957). It decreases fairly linearly from 2.5 at 16 Mev to 1.3 at 24 Mev. The calculated cross-section curve for the reaction $Ag^{107}(\gamma, \alpha)Rh^{103}$ is given in Fig. 2 (dotted curve). The characteristic values are:

$$\sigma_m = 94\ \mu b$$
$$E_m = 20.5\ \text{Mev}$$
$$\Gamma_{\frac{1}{2}} = 6.3\ \text{Mev}$$
$$\int_0^{24\ \text{Mev}} \sigma dE = 0.54\ \text{Mev.mb.}$$

4. The Total Reaction $Ag(\gamma, \alpha)Rh$

The cross section for the total reaction $Ag(\gamma, \alpha)Rh$ was calculated from the cross-section curves of the two isotopes. It is also shown in Fig. 2 (dashed curve). The characteristic values of this curve are:

$$\sigma_m = 75\ \mu b$$
$$E_m = 20.8\ \text{Mev}$$
$$\Gamma_{\frac{1}{2}} = 6.3\ \text{Mev}$$
$$\int_0^{24\ \text{Mev}} \sigma dE = 0.43\ \text{Mev.mb.}$$

TABLE I

Reported values for the reaction $Ag^{109}(\gamma, \alpha)Rh^{105}$

References	Yield, α/r mole	E_m, Mev	σ_m, μb	$\Gamma_{1/2}$, Mev	$\int_0^{E_1} \sigma dE$, Mev.mb	E_1, Mev
Laboulaye and Beudon (1954)	2200 at 23 Mev	22	~170		~1	24
Laboulaye and Beudon (renorm.)	1200 at 23 Mev		~90		~0.6	24
Greenberg *et al.* (1954)	50 at 23 Mev					
Greenberg (1955)	1750 at 23 Mev					
Schmouker *et al.* (1955)						
Erdös *et al.* (1955)						
Erdös (1957)	1360 at 32 Mev				0.2	32
Present work	970 at 23 Mev	21.0	55	6.1	0.31	24

TABLE II

Reported values for the reaction $Ag(\gamma, \alpha)Rh$

References	Yield, α/r mole	E_m, Mev	σ_m, μb	$\Gamma_{1/2}$, Mev	$\int_0^{E_1} \sigma dE$, Mev.mb	E_1, Mev
Greenberg *et al.* (1954)	67 at 23 Mev					
Greenberg (1957)	2000 at 23 Mev	>24	>210			
Toms *et al.* (1958)	1700±700 at 21.5 Mev					
Present work	1420 at 23 Mev	20.8	75	6.3	0.43	24

IV. DISCUSSION

1. $Ag^{109}(\gamma, \alpha)Rh^{105}$

The previously reported values for this reaction are given in Table I. Laboulaye and Beudon (1954) normalized their relative values according to the reported values of Katz *et al.* (1951) for the reaction $Ni^{58}(\gamma, n)Ni^{57}$. If the newer values of Roalsvig, Haslam, and McKenzie (1959) are used for this reaction, the yield value of Laboulaye and Beudon at 23 Mev becomes 1200 α/r mole, which is in reasonable agreement with our value 970 α/r mole. The yield value of Greenberg *et al.* (1954) is as mentioned previously far lower than any other value reported. However, the same author (1955) obtained a new yield value which is somewhat higher than the present one. Schmouker *et al.* (1955), Erdös *et al.* (1955), and Erdös (1957) obtained a yield of 1360 α/r mole at 32 Mev, which agrees with our value in the order of magnitude, as can be seen by the dashed extension of our activation curve on Fig. 1. The present value for the maximum cross section is much lower than that reported by Laboulaye and Beudon (1954), by a factor of about two if the renormalized curve is used.

However, our value for the integrated cross section lies in the region between the value of Laboulaye and Beudon and that of the Swiss group.

2. $Ag(\gamma, \alpha)Rh$

The previously reported values for the gamma–alpha reaction in silver are given in Table II. By using the photon spectrum as given by Katz and Cameron (1951), the ratio of the yields of the reactions $Ag(\gamma, \alpha)Rh$ and $Ag^{109}(\gamma, \alpha)Rh^{105}$ at 23 Mev was calculated from the curves in Fig. 2 to be 1.46. Taking the yield value of $Ag^{109}(\gamma, \alpha)Rh^{105}$ to be 970 α/r mole, the yield value of $Ag(\gamma, \alpha)Rh$ at 23 Mev becomes 1420 α/r mole.

The present yield value at 23 Mev is somewhat lower than those reported by Greenberg (1957) and Toms *et al.* (1958) using photographic plates, however, of the same order of magnitude. Since events in which neutron or proton emission follow the alpha-particle emission would be detected in plate work, but not in our work, the present lower value would be expected.

This might also be seen by a comparison of the cross-section curves of Greenberg (1957) and of the present work. Greenberg's cross-section curve is still rising at 24 Mev, while our curve has passed its maximum and is falling off rapidly at this energy.

REFERENCES

BAKER, R. G. and KATZ, L. 1953. Nucleonics, **11** (2), 14.
BLATT, J. M. and WEISSKOPF, V. F. 1952. Theoretical nuclear physics (John Wiley & Sons, Inc., New York).
ERDÖS, P., JORDAN, P., and STOLL, P. 1955. Helv. Phys. Acta, **28**, 322.
ERDÖS, P. 1957. Helv. Phys. Acta, **30**, 639.
GREENBERG, L., TAYLOR, J. G. V., and Haslam, R. N. H. 1954. Phys. Rev. **95**, 1540.
GREENBERG, L. 1955. Private communication.
——— 1957. Ph.D. Thesis, University of Saskatchewan, Saskatoon, Saskatchewan.
KATZ, L. and CAMERON, A. G. W. 1951. Can. J. Phys. **29**, 518.
KATZ, L., JOHNS, H. E., BAKER, R. G., HASLAM, R. N. H., and DOUGLAS, R. A. 1951. Phys. Rev. **82**, 271.
LABOULAYE, H. DE and BEUDON, J. 1954. Compt. rend. **239**, 411.

PENFOLD, A. S. and LEISS, J. E. 1958. Analysis of photo cross sections, Physics Research Laboratory, University of Illinois, Champaign, Illinois, U.S.A.
ROALSVIG, J. P., HASLAM, R. N. H., and MCKENZIE, D. 1959. Can. J. Phys. **37**, 607.
SCHMOUKER, J., ERDÖS, P., JORDAN, P., and STOLL, P. 1955. J. Phys. Rad. **16**, 169.
TOMS, M. E. and MCELHINNEY, J. 1958. Yields of photo-alpha particles, NRL Problem H 01-09, Conference on Photonuclear Reactions, Washington, D.C., U.S.A.

STATISTICAL THEORY OF AVALANCHE BREAKDOWN IN SILICON[1]

R. E. BURGESS

ABSTRACT

The current flowing in silicon junctions under conditions of high electric field sufficient to cause avalanche breakdown consists of a sequence of pulses of constant magnitude and with randomly distributed spacing and duration. A statistical model is presented for this intermittent conduction mechanism in which the transition probabilities between the conducting and non-conducting states are Markoffian and depend on the excess of the applied voltage over the breakdown voltage; power-law and exponential dependences are considered and the precise form is shown not to be critical in deriving from these simple conditions a number of predictions about the macroscopic current–voltage characteristic, all of which have been confirmed by experiment.

It is demonstrated generally that a randomly switched discharge of positive resistance has a macroscopic current–voltage characteristic which depends upon the d-c. source resistance and can have a region of negative slope. Only with a negligibly small source resistance is the true characteristic obtained.

The observable fluctuations of current and their spectral distribution are derived and indicate the noisiness of silicon junctions under avalanche conditions.

The influence of illumination on the breakdown statistics and macroscopic characteristic are briefly discussed.

1. INTRODUCTION

Conventional circuit elements whether linear or non-linear display d-c. current–voltage characteristics which are independent of the resistance of the e.m.f. source used for the measurement. If, however, the element is time-variable (either in a systematic or random fashion), the macroscopic d-c. characteristic, i.e. the relation between the average current and average voltage, will in general be a function of the source resistance. This implies that a detailed specification of external source conditions is required in order to give an unequivocal meaning to measured characteristics.

The present paper is primarily concerned with the properties of avalanche diodes which effectively contain a random switch in series with a resistive component which may be linear or non-linear but always has a positive differential resistance.

In general if the source e.m.f. is E and its resistance S the mean current $\bar{\imath}$ and the mean potential difference (p.d.) $\bar{v}$ across the diode are related by $E = \bar{\imath}S + \bar{v}$ where the bar denotes averages over times long enough to provide representative values of the current and voltage, i.e. long compared with the relaxation times of the process. Then $\bar{\imath}$ and $\bar{v}$ correspond to values indicated by meters having inertia.

The ratio $\bar{v}/\bar{\imath}$ is the apparent d-c. resistance R_0 of the diode, and the deriva-

[1]Manuscript received March 10, 1959.

Contribution from the Department of Physics, University of British Columbia, Vancouver, B.C. The research for this paper was supported by the Defence Research Board of Canada under Grant No. 9512-22.

tive $d\bar{v}/d\bar{\imath}$ is its apparent differential resistance ρ. Both of these will, in general, be a function of the source resistance and e.m.f. Furthermore, even though the resistive components in the circuit are positive, it is possible for the apparent differential resistance to be negative under certain conditions.

These considerations are particularly relevant to the phenomenon of avalanche breakdown in strong electric fields (over 2×10^5 v/cm) arising in silicon avalanche diodes in which the current flow is composed of a random sequence of rectangular and unidirectional current pulses of fixed amplitude. The random timing and duration of the impulses correspond to the stochastic character of the avalanche multiplication process which causes a breakdown discharge in localized regions of high electric field (McKay 1954; Newman 1955; Chynoweth and McKay 1956). The use of these diodes as voltage regulators and switching elements calls for an examination of the manner in which the random character of the conduction process determines the macroscopic characteristics in a given circuit and also the "noisiness" of the device as expressed in terms of microscopic fluctuations of the instantaneous operating point about its mean position.

Some of the experimentally observable effects in avalanche diodes are shown to stem from the voltage dependence of the switching transition probabilities from one state to the other. Physical models are related to these statistical parameters and lead to a phenomenological explanation of the complicated characteristics observed in avalanche diodes under breakdown conditions. The basic statistical model analyzed involves a switch in two states—open (state 0) and closed (state 1) and undergoing transitions between these states with transition probabilities p_{01} and p_{10} per unit time. In the steady state (assuming statistical stationarity) the fraction f of the time that the switch is closed is given by

$$\frac{f}{1-f}=\frac{p_{01}}{p_{10}} \tag{1.1}$$

or

$$f=\frac{p_{01}}{p_{01}+p_{10}}. \tag{1.2}$$

The mean frequency of the switch closings (or openings) is

$$\nu=\frac{p_{01}p_{10}}{p_{01}+p_{10}}=\frac{f}{\tau_1}=\frac{1-f}{\tau_0} \tag{1.3}$$

where $\tau_1 = 1/p_{10}$ is the mean duration of the 1-state and $\tau_0 = 1/p_{01}$ is the mean duration of the 0-state.

For the current pulses to be rectangular (i.e. very rapid rise and fall and flat-topped) the capacitance across the diode must be small enough for the associated charge and discharge time constants to be small compared with $1/p_{10}$ and $1/p_{01}$.

The d-c. macroscopic characteristic relating $\bar{\imath}$ and $\bar{v}$ as measured by meters with time constants larger than $1/\nu$ also represents the a-c. characteristic at frequencies small compared with ν. The irregular variations of the current

and voltage will appear as noise superimposed on the average characteristic.

The differential resistance discussed later is defined as the slope of the $\bar{v}$, $\bar{\imath}$ curve at constant S:

$$\rho \equiv \left(\frac{d\bar{v}}{d\bar{\imath}}\right)_S = \left(\frac{d\bar{v}}{dE}\right)_S \Big/ \left(\frac{d\bar{\imath}}{dE}\right)_S. \tag{1.4}$$

This definition is chosen because of its theoretical significance and its correspondence to the manner in which the characteristic is commonly determined, i.e. by variation of E with S fixed.

If i_0 and v_0 are the current and voltage in state 0 and i_1 and v_1 the values in state 1 the macroscopic averages are

$$\bar{\imath} = fi_1+(1-f)i_0 \qquad \bar{v} = E-S[fi_1+(1-f)i_0]$$

and the apparent d-c. resistance is

$$R_0 = \frac{E}{fi_1+(1-f)i_0}-S, \tag{1.5}$$

while the differential resistance is

$$\rho = \frac{1}{d[fi_1+(1-f)i_0]/dE}-S. \tag{1.6}$$

Even in the simple case where the random switch is in series with a fixed linear resistance R so that $i_0 = 0$ and $i_1 = E/(S+R)$ and even if f is constant it is seen that both the d-c. resistance and the differential resistance depend on the resistance of the source. Furthermore, if df/dE is sufficiently large, ρ can be negative even though the system contains a linear positive resistance. These features are unorthodox since normally the d-c. characteristics of even a non-linear resistive device do not depend upon the source resistance used for measurement.

2. CHARACTERISTICS OF A RANDOM AVALANCHE BREAKDOWN

Let it now be supposed that f and R are both functions of voltage as is the case in the intermittent discharge which appears in silicon p–n junctions under avalanche conditions. In general the statistics of the switch depend upon the voltage across the device in both states. It will be assumed that the diode passes a prebreakdown current i_0 when the applied p.d. is less than threshold value v_b; for v above v_b the current increases proportionally to the excess voltage due to the discharge path:

$$i = i_0 \quad \text{for } v < v_b \qquad\qquad i = i_0+g(v-v_b) \quad \text{for } v > v_b \tag{2.1}$$

where g is the discharge conductance. Then when $E \geqslant v_b+Si_0$

$$v_1 = \frac{E+Sgv_b-Si_0}{1+Sg} \qquad i_1 = i_0+\frac{g(E-v_b-Si_0)}{1+Sg} \tag{2.2}$$

are the p.d. and current in the discharge condition (state 1).
Hence

$$\bar{v} = E-S\bar{\imath} \qquad \bar{\imath} = i_0+\frac{fg(E-v_b-Si_0)}{1+Sg}. \tag{2.3}$$

On the assumption that the parameters g and i_0 are independent of E the apparent differential resistance is

$$\rho = \frac{S+(1/g)}{d[f(E-v_b-Si_0)]/dE} - S \tag{2.4}$$

which is a function of both E and S. The value of ρ when $S = 0$ will be denoted ρ_0 (the intrinsic ρ of the diode) and this is seen to be always positive for the systems under consideration in which df/dE is non-negative.

When $S > 0$, the $\bar{\imath}$, $\bar{v}$ characteristic can have a negative slope if f is a sufficiently rapidly increasing function of E and this tendency is more pronounced as S is made larger. Clearly a negative differential resistance can only appear if $S > \rho_0/(1-\rho_0 g)$. Hence the expected behavior is that, if S is sufficiently large, as E (and $\bar{\imath}$) increase $\bar{v}$ will show first a maximum and then a minimum with the region of negative ρ lying between these extrema.

In terms of the transition probabilities we have

$$\frac{df}{dE} = f(1-f)\left[\frac{1}{p_{01}}\frac{dp_{01}}{dv_0} - \frac{1}{1+gS}\frac{1}{p_{10}}\frac{dp_{10}}{dv_1}\right]$$

where p_{01} is a function of v_0 $(=E-Si_0)$ while p_{10} is a function of v_1. It is seen that df/dE is zero at $f = 0$ and 1 and will have a maximum at some value of f which depends upon the precise dependence of p_{01}/p_{10} on $(E-v_b)$ and will usually lie near $f = 0.5$.

The intrinsic macroscopic characteristic has a slope,

$$\frac{1}{\rho_0} = g\frac{d[f(E-v_b)]}{dE}, \tag{2.5}$$

which can be appreciably greater than the true conductance g of the avalanche discharge path. This intrinsic parameter enables the differential resistance for any finite S to be expressed as

$$\rho = \rho_0(1+gS) - S. \tag{2.6}$$

In view of the statistical nature of the avalanche process it is clear that p_{01} must be proportional to the rate of influx of carriers entering the high-field region where breakdown occurs and also be an increasing function of the excess of v_0 over the breakdown voltage v_b. Conversely the switch-off probability p_{10} will be a rapidly decreasing function of (v_1-v_b), since the discharge can be maintained with greater certainty when there is an excess of energy imparted to the avalanching carriers over that needed just to sustain the feedback mechanism provided by the ionization due to the carriers of both signs.

When the discharge region is broken down and taking up a potential difference v_b the resistance $(1/g)$ of the system is assumed to be constant. This resistance is composed of the sum of the differential resistance of the discharge and the series resistance of the spreading regions on either side of the discharge; the current constriction due to the extremely localized nature of the discharge will probably result in this bulk resistance being the significant part of the total.

(*a*) *Power-Law Model*

In order to consider the dependence of f on E in more detail we must postulate the dependence of the transition probabilities p_{01} and p_{10} on the voltages v_0 and v_1 which exist before each transition. One possible form suggested by physical considerations is:

$$\begin{cases} p_{01} = A(v_0 - v_b)^m \\ p_{10} = B(v_1 - v_b)^{-n} \end{cases} \tag{2.7}$$

giving

$$\frac{1}{f} - 1 = \frac{B}{A} \frac{(1+Sg)^n}{(E - v_b - Si_0)^{m+n}}$$

which assert that the probability of breakdown ($0 \rightarrow 1$) is an increasing function of the excess of v_0 over v_b while the probability of the discharge ceasing ($1 \rightarrow 0$) is a decreasing function of the excess of v_1 over v_b. Thus f is a monotonically increasing function of E.

For this model it is found that

$$\frac{df}{dE} = \frac{f(1-f)(m+n)}{E - v_b - Si_0}$$

and hence

$$\rho = \frac{gS(1-f)[1-f(n+m)]+1}{gf[1+(1-f)(n+m)]}. \tag{2.8}$$

If gS is sufficiently large the macroscopic characteristic will show "turnover" ($\rho = 0$) at the two values of f given by

$$f = \frac{n+m+1 \pm [(n+m-1)^2 - 4(n+m)/gS]^{\frac{1}{2}}}{2(n+m)}, \tag{2.9}$$

which correspond to the maximum and minimum of $\bar{v}$ which appear in the macroscopic characteristic.

The minimum value of ρ_0 and hence of ρ for any arbitrary S occurs when $f = (n+m+1)/2(n+m)$ which is midway between the two values for turnover (if they exist). At this point

$$\rho = \rho_{\min} = \frac{4(n+m) - gS(n+m-1)^2}{g(n+m+1)^2}. \tag{2.10}$$

Thus if

$$S > \frac{4(n+m)}{g(n+m-1)^2} \tag{2.11}$$

a negative slope will appear in the characteristic which would not be manifested if S were zero. The slope of the intrinsic characteristic is

$$\frac{1}{\rho_0} = gf[1+(m+n)(1-f)]. \tag{2.12}$$

Experimental data on ionization rates as a function of electric field and on the slope of intrinsic characteristic indicates that $m+n \gg 1$. Thus the value

of f for which the slope is a maximum and hence ρ is a minimum (for any S) is just slightly above $\frac{1}{2}$. Experimental observation confirms that the slope of the macroscopic characteristic for $S = 0$ can, when $f \simeq \frac{1}{2}$, considerably exceed the conductance g corresponding to a sustained discharge ($f = 1$). For instance, if typically $m+n = 14$ and $f = \frac{1}{2}$ the slope is $4g$. Thus the apparent sharpness of the breakdown process is enhanced by the relatively rapid increase of the duty-cycle ratio f with applied voltage. For $m+n = 14$ the value of f for minimum ρ is 0.536 and a value of S of only $1/3g$ would be adequate to cause the appearance of a negative slope in the $\bar{\imath}$, $\bar{v}$ characteristic; a smaller value of S would preserve a positive slope which, however, would be very much greater than g. The importance of the source resistance in determining the abruptness of the breakdown in avalanche diodes is overlooked in commercial specifications of these devices.

From equations (1.2), (1.3), and (2.6) it is seen that as the source resistance S is increased the mean frequency ν of the pulses increases while the mean duration τ_1 and their fractional duration ($f = \nu\tau_1$) decrease. As the source voltage is increased τ_1 and f increase while ν passes through a maximum.

(*b*) *Exponential Model*

An alternative model for the transition probabilities has the general form

$$\begin{cases} p_{01} = a \exp[\alpha(v_0 - v_b)^r] \\ p_{10} = b \exp[-\beta(v_1 - v_b)^r] \end{cases} \tag{2.13}$$

where r can be positive or negative. It is seen that the following conditions would hold for the parameters:

$$\begin{array}{lll} \text{if } r > 0 & \alpha, \beta > 0 & a \ll b \\ \text{if } r < 0 & \alpha, \beta < 0 & a \gg b \end{array}$$

These are required to ensure that p_{01} is an increasing function of v_0 and that p_{10} is a decreasing function of v_1. Also if r is positive, p_{01}/p_{10} must become very small compared with unity at voltages just above v_b; conversely, if r is negative p_{01}/p_{10} must become very large compared with unity when the voltage appreciably exceeds v_b.

The slope of the intrinsic characteristic for these transition probabilities is found to be

$$\frac{1}{\rho_0} = gf\left[1+(1-f)r \ln\left(\frac{b}{a}\frac{f}{1-f}\right)\right] \tag{2.14}$$

and the important term in $r \ln(b/a)$ is seen always to be positive. If, as is anticipated, this term is large compared with unity the slope will have its maximum for f close to but slightly above $\frac{1}{2}$. At $f = \frac{1}{2}$

$$\frac{1}{\rho_0} = \frac{g}{2}\left[1+\frac{r}{2}\ln\frac{b}{a}\right]. \tag{2.15}$$

Typically if $r = 1$, $b/a = 10^6$ the value of $1/\rho_0$ is $4g$. It is seen by comparison with the power-law model that the intrinsic slope is closely similar in form

if $(m+n)$ is replaced by $r \ln(b/a)$. It is concluded that (except when f is very near to 0 or 1) the details of the model for the transition probabilities are not significant in determining the macroscopic characteristics of the device.

The choice of r would depend upon physical considerations such as the $\exp(-c/F)$ dependence of the ionization rate on electric field F (cf. Chynoweth 1958) which determines the probabilities of the breakdown initiating and ceasing. The use of a negative r may be particularly appropriate where the probabilities need to be described accurately in the region of small excess voltage (p_{01} very small, p_{10} very large, f very small).

3. FLUCTUATIONS

The variances of the current and potential difference provide measures of the over-all "noisiness" of the device:

$$\text{var } i = f(1-f)(i_1-i_0)^2, \tag{3.1}$$

$$\text{var } v = S^2 \text{ var } i. \tag{3.2}$$

Both variances have $f(1-f)$ as a factor which arises from the similarity of the random switching process to a Bernoulli trial.

The spectral density of the current fluctuations is given by (see Appendix)

$$W_i(\omega) = \frac{4\tau \text{ var } i}{1+\omega^2\tau^2} = \frac{4f(1-f)(i_1-i_0)^2\tau}{1+\omega^2\tau^2} \tag{3.3}$$

where $\tau = 1/(p_{01}+p_{10})$. This simple type of single-relaxation-time spectrum had already been inferred for silicon avalanche noise (Burgess 1955).

Substituting from (2.2)

$$W_i(\omega) = \frac{4f(1-f)\tau}{1+\omega^2\tau^2}\left[\frac{g(E-v_b-Si_0)}{1+Sg}\right]^2. \tag{3.4}$$

Although the spectral density has the simple form $(1+\omega^2\tau^2)^{-1}$ for its frequency distribution, its dependence on the source e.m.f. E and resistance S is complicated since these terms appear directly and also implicitly in f and τ.

Since the noise arises from a gross modulation of the current flow it is normally very much greater than the shot noise $2e\bar{i}$ which would be associated with the current, the ratio being of the order of $(i_1-i_0)\tau/e$ which might typically lie in the range 10^8 to 10^{14}. Alternatively the noise due to the avalanche process may be likened to a form of shot noise in which charge q of mean square value $2(i_1-i_0)^2\tau^2$ is randomly transported at mean rate ν so giving a low frequency spectral density $2\nu\overline{q^2} = 4f(1-f)\tau(i_1-i_0)^2$ in agreement with (3.3).

4. EFFECT OF ILLUMINATION ON AVALANCHE BREAKDOWN

If a silicon junction is illuminated with photons of energy sufficient to produce carrier pairs, a fraction of these will enter the localized region in which avalanche breakdown is occurring. The dominant effect of this will be

to increase p_{01} in direct proportion to the increase of prebreakdown current i_0 since each carrier entering the region has a certain probability of initiating the discharge, that is, the parameter A in equation (2.7) or a in (2.13) is proportional to the carrier influx. The other parameters are not expected to be affected significantly; some increase of g due to bulk photoconductivity may become important at large values of S.

The observable effects of illumination are thus expected to be the increased frequency of the current pulses by virtue of a decrease of the mean off-time τ_0. The resulting increase of f increases $\bar{\imath}$ whatever the value of the source resistance. However, the slope of the intrinsic characteristic may be increased or decreased by illumination depending upon whether f is moved closer to or further from the value which minimizes ρ_0.

5. CONCLUSIONS

The statistical treatment of the previous sections leads to the following conclusions regarding silicon junction diodes in the avalanche breakdown region:

(i) The macroscopic characteristic is a function of the source resistance and as $(E-v_b)$ increases the characteristics for various S converge to a single function since $f \to 1$ and the uninterrupted discharge is measured.

(ii) If the source resistance is large enough a negative slope will appear between two voltage turnover points in the macroscopic characteristic. The minimum value of the slope resistance occurs for a value of f slightly above 0.5.

(iii) The mean frequency of the current pulses is an increasing function of the source resistance while it displays a maximum as $E-v_b$ increases.

(iv) The amplitude of the current pulses is a linear function of the applied voltage (equation 2.2).

(v) The mean duration τ_1 of the impulses and the fractional duty cycle f are increasing functions of $(E-v_b)$ and decreasing functions of S.

(vi) The slope of the intrinsic characteristic can be appreciably greater than the true conductance of the avalanche discharge path.

(vii) The noise spectral density of the current fluctuations is of the form $W(0)/(1+\omega^2\tau^2)$, and is greatly in excess of shot noise ($W(0) \gg 2e\bar{\imath}$).

(viii) Illumination of the junction decreases the mean off-time τ_0 and increases the mean pulse frequency ν and the fractional duty cycle f.

All of these inferences have been confirmed experimentally (Drews 1957). They also incidentally indicate that most published experimental data and commercial specifications of silicon avalanche diodes are without significance in the absence of a statement of the resistance of the voltage source used for the measurements. In principle this should be zero; when S is made very small there is experimental evidence to indicate that no negative resistance arises in the discharge path itself and this is consistent with our adoption of a positive g in the model.

REFERENCES

BURGESS, R. E. 1955. Brit. J. Appl. Phys. **6**, 185.
——— 1956. Proc. Phys. Soc. B, **69**, 1020.
CHYNOWETH, A. G. 1958. Phys. Rev. **109**, 1537.
CHYNOWETH, A. G. and MCKAY, K. G. 1956. Phys. Rev. **102**, 369.
DREWS, R. E. 1957. M.Sc. Thesis, University of British Columbia, Vancouver, B.C.
MCKAY, K. G. 1954. Phys. Rev. **94**, 877.
NEWMAN, R. 1955. Phys. Rev. **100**, 700.

APPENDIX

SPECTRAL DISTRIBUTION FOR RANDOM TRANSITIONS BETWEEN TWO STATES

The spectral distribution can be readily derived using the "g–r" theory for a univariate Markoff process (Burgess 1956). Consider N independent identical systems, each capable of existing in two states 0 and 1. Then in terms of the transition probabilities p_{01} and p_{10} the rate law for the number of systems n in state 1 is the simple linear equation:

$$\frac{dn}{dt} = (N-n)\,p_{01} - n\,p_{10}$$

where the first term corresponds to the generation (or forward) rate (g) while the latter corresponds to the reverse rate (r).

The equilibrium value of n given by $g(\bar{n}) = r(\bar{n})$ is

$$\bar{n} \equiv Nf = N\frac{p_{01}}{p_{01}+p_{10}}$$

where (cf. equation 1.2) we identify $\bar{n}/N$ with f, the probability of a system being in state 1.

The relaxation time for perturbations from equilibrium is:

$$\tau = \left(\frac{dr}{dn} - \frac{dg}{dn}\right)^{-1}_{n=\bar{n}} = \frac{1}{p_{01}+p_{10}}$$

and the variance of n is given by the Bernoulli result:

$$\text{var } n = \tau g(\bar{n}) = Nf(1-f).$$

Since the fluctuations in n derive from a simple relaxation process the spectral density is

$$W_n(\omega) = \frac{4\tau \text{ var } n}{1+\omega^2\tau^2}.$$

For our case of a single discharge path we put $N = 1$ and since the current change in the transition from the 0-state to the 1-state is $(i_1 - i_0)$, the spectral distribution of the current fluctuations is:

$$W_i(\omega) = \frac{4f(1-f)(i_1-i_0)^2\tau}{1+\omega^2\tau^2} \tag{3.3}$$

by virtue of the one-to-one correspondence between the state variable n and the current i.

CRYSTAL GROWTH AND THE THERMODYNAMICS OF IRREVERSIBLE PROCESSES[1]

J. S. KIRKALDY

ABSTRACT

The principle of minimum rate of entropy production is applied to steady-state transport processes in the neighborhood of an alloy crystal face growing into its melt. The procedure gives a satisfactory rationale of observed interface morphology. It is noted that segregation, which occurs in cellular or dendritic growth of alloys, is a direct manifestation of the system's attempt to minimize entropy production by conserving free energy. The general problems of growth of pure and impure single crystals from the melt and vapor are discussed.

INTRODUCTION

There are many dissipative systems in nature for which the external constraints and the phenomenological transport equations do not uniquely determine the process path. The most familiar of such systems are those involving internal phase interfaces. These interfaces introduce further (internal) constraints into the system in the form of supersaturation relationships, continuity conditions, and heat sources or sinks, but because of the flexibility of the interface morphology and the existence (in some cases) of surface transport mechanisms, the process path may still not be uniquely determined. A familiar example of this is the steady-state unidirectional growth of an alloy single crystal into its melt. Evidently, for such a system we can satisfy the phenomenological equations and the constraints for a very wide range of growth conditions with the presumption of a flat interface. However, we know that for many conditions of growth within this range the interface actually attains a cellular or dendritic morphology (Tiller and Rutter 1956). The question then arises: What thermodynamic principle determines the choice of process path (if there is a choice) for a given complex irreversible process?

In the past, various principles have been invoked for the case of crystal growth: choice of configuration for optimum heat transfer, the elimination of constitutional supercooling (in alloy crystal growth), or, somewhat equivalently, passage through states of minimum free energy. While these perhaps contain elements of the truth in their specific applications, they have no fundamental foundation. Accordingly we have looked to the thermodynamics of irreversible processes for a suitable generalization.

THE PRINCIPLE OF MINIMUM RATE OF ENTROPY PRODUCTION

Prigogine (1955) and de Groot (1952*a*) have stated an important theorem applicable to single-phase dissipative systems in the steady state. We paraphrase this as follows: In a system which can be described by n independent

[1]Manuscript received in original form September 26, 1958, and, as revised, February 23, 1959.
Contribution from the Department of Metallurgy and Metallurgical Engineering, McMaster University, Hamilton, Ontario.

continuous thermodynamic forces (free energy or thermal gradients, chemical affinities), $\mathbf{X}_1, \mathbf{X}_2, \ldots \mathbf{X}_n$, of which $\mathbf{X}_1, \mathbf{X}_2, \ldots \mathbf{X}_k$ are fixed by the boundary conditions and a further number $n-k$ of forces, $\mathbf{X}_{k+1}, \mathbf{X}_{k+2}, \ldots \mathbf{X}_n$ are free to adjust themselves in conformity with the first k forces, the system approaches the steady state defined by the fluxes $\mathbf{J}_i = 0$ $(i = k+1, k+2, \ldots n)$ with a minimum in the rate of entropy production per unit volume, σ. The $\mathbf{J}_i$ are linearly related to the thermodynamic forces by

$$\mathbf{J}_i = \sum_{j=1} L_{ij}\mathbf{X}_j \qquad (i = 1, 2, \ldots n), \tag{1}$$

and are conjugated in such a way that

$$T\sigma = \sum_{i=1}^{n} \mathbf{J}_i \cdot \mathbf{X}_i, \tag{2}$$

where T is the absolute temperature. The quantity $T\sigma$ has the form of a sum of Joule heats and is accordingly known as the energy dissipation function.

In another formulation, Brown (1958) has shown that for a single-phase, multicomponent system in a steady conduction–diffusion–reaction state, the field equations can be derived from the variation principle

$$\delta \int_V \sigma dV = 0 \qquad \text{(minimum)}. \tag{3}$$

This form is most useful for our present purposes. It is to be noted that both formulations of the principle of minimum entropy production assume the constancy of the phenomenological coefficients and require that the processes be near equilibrium for their validity.

In what follows we plan to interpret these statements in a much wider sense than is implied by the mathematical formalism leading to them. In particular our variations will be made in the interface morphology without establishing the connection between these variations and the mathematical ones involved in the precise statements. Furthermore, we extend the principle to apply to heterogeneous as well as homogeneous systems. As such, these statements become postulates of qualitative behavior, and even though they have some theoretical basis and appreciable intuitive compulsion, they must stand in the final analysis on the agreement between the deductions from them and the observations.

For non-stationary systems, we extend the steady-state principle by assuming the qualitative principle that any dissipative system starting from an initial condition with specified external constraints and proceeding towards a steady state (equilibrium is considered to be a steady state of order zero) proceeds through states of minimum integrated entropy production rate. We base this on the fact that one can think of any complex non-steady-state process as proceeding towards a continuous series of quasi-stationary states, provided the relaxation time for local change in entropy production rate (e.g., the time required for a crystal face to change its morphology a significant amount) is much less than the relaxation time for the whole process.

GROWTH OF ALLOY SINGLE CRYSTALS

Consider the steady-state growth of a metal single crystal into a binary alloy melt. We will ignore for the moment any crystallographic or nucleation effects and consider the thermodynamics of a typical volume V (see Fig. 1) which migrates at the same constant rate v as the solid–liquid interface. It is not necessary for the following qualitative arguments to specify the third dimension of Fig. 1. However, in line with the observations, we can think of the cuspoidal liquid indentations as the elevation of an array of cell boundaries.

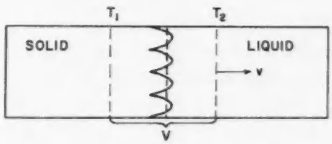

FIG. 1. Schematic advancing steady-state solid–liquid interface.

The Variation Principle and Interface Morphology

The variation principle (3) applied to a growing alloy single crystal is

$$(4)\quad \delta \int_V \sigma \, dV = \delta\left[\int_V \frac{(\mathbf{J}_q \cdot \mathbf{X}_q + \sum \mathbf{J}_k \cdot \mathbf{X}_k)}{T} dV + \int_a \sum \frac{J_i A_i da}{T}\right] = 0$$

where q refers to thermal and k to diffusion variables. A_i is the chemical affinity and J_i is the chemical reaction rate for reaction i. Solidification of a binary alloy involves two reactions: components 1 and 2 from liquid (L) to solid (S). Because these are surface reactions we have transposed the corresponding volume integral into a surface one.

The thermodynamic forces are (de Groot 1952*b*)

$$(5)\quad \mathbf{X}_q = -\frac{\nabla T}{T},$$

$$(6)\quad \mathbf{X}_k = -T\nabla\left(\frac{\mu_k}{T}\right),$$

and

$$(7)\quad A_i = \mu_i^{\mathrm{L}} - \mu_i^{\mathrm{S}},$$

and if we ignore the Soret and Dufour effects (due to cross terms in the phenomenological transport matrix), the fluxes are

$$(8)\quad \mathbf{J}_q = -K\nabla T$$

where K is the conventional thermal conductivity,

$$(9)\quad \mathbf{J}_k = \sum_{i=1}^{n} L_{ki}\mathbf{X}_i,$$

and

$$(10)\quad J_i = v\rho_i / M_i.$$

where ρ_i and M_i are the masses per unit volume in the solid alloy and the atomic masses, respectively. If v is taken constant, the element of area in (4) must always be taken at right angles to the average growth direction.

For dilute ideal binary solutions the integrands in (4) reduce approximately to (see Appendix I)

$$\sigma_V = \frac{K}{T^2}(\nabla T)^2 + \frac{DR\rho_2}{M_2 C_1}(\nabla C_1)^2 \tag{11}$$

and

$$\sigma_a = \frac{1}{T}\sum_{i=1}^{2} J_i A_i = \frac{v}{T}\left[\frac{\rho_1}{M_1}(\mu_1^L - \mu_1^S) + \frac{\rho_2}{M_2}(\mu_2^L - \mu_2^S)\right] \tag{12}$$

where D is the diffusion coefficient, and R is the gas constant per mole. The concentration of solute, C_1, is measured in mole fractions. To apply the variation principle we set our boundary conditions so that the liquid metal has an initial composition of C_0 and along the direction of growth fix two temperatures T_1 and T_2 which include the melting range of the alloy. We then proceed to move these fixed temperature points at an equal and constant velocity v. Shortly, a steady state will be attained in the volume V, which for argument's sake has a morphology as indicated in Fig. 1. Now we mentally vary the interface from the steady configuration to a virtual one involving a flat interface (dotted) and note thereby the change in the total rate of entropy production in V. This is a convenient variation since a tractable mathematical solution of the transport equations for a flat interface with the same growth rate is already known.

Observationally, for a given alloy single crystal, cells appear only if the velocity exceeds a certain critical value (Walton *et al.* 1959). For conditions only slightly more severe than the critical ones, the cells are quite featureless, and crystallographic effects appear only in the extent and orientation of the cell boundaries. This suggests for these conditions that the variation of the reaction rate term in (4) is of secondary importance and that explicit contributions will only appear when the cells become sufficiently elongated that large areas of other low index interfaces are bared. We will accordingly neglect this term to the first order in a variation between a flat and slightly corrugated interface.

The contributions of the conduction and diffusion terms to σ can be evaluated in terms of known coefficients and in the neighborhood of the interface, near the critical conditions, they turn out to be of the same magnitude. For the particular example examined in Appendix I, the contribution per unit volume of liquid was three times greater in the diffusion field than in the thermal field. Comparing the qualitative liquid solute distribution of Fig. 2 with that for the corresponding flat interface we conclude that for the non-planar configuration the effective volume of integration in the liquid is relatively small, tending to a lowered total entropy production rate. On the other hand, the lateral gradients introduced tend to cancel this to an undetermined extent. The entropy production due to diffusion in the solid is negligible because of the low diffusion coefficients.

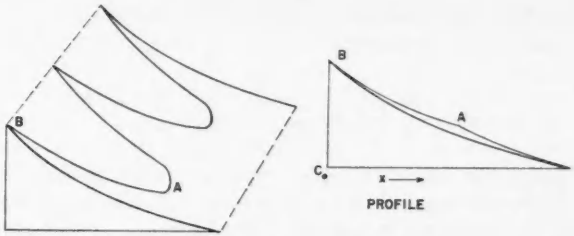

FIG. 2. Representative steady-state liquid solute distribution near an advancing solid–liquid interface.

Finally, referring to Fig. 2 and paying close attention to the projection profile and the requirement of substantial interfacial equilibrium, it seems plausible that in varying from a flat to a corrugated interface, the average latent heat source is moved closer to the sink at T_1 as indicated in Fig. 1, with a corresponding decrease in the integrated conduction entropy production. It must, however, be noted that the decrease in entropy production will arise mainly through the replacement of some of the solid by liquid ($K_S \sim 2K_L$) near the cell cusps. The change in effective volume of integration therefore appears to be much smaller than in the diffusion field so the contribution to the total entropy production change may be negligible. Some numerical estimates in favor of this conclusion are given at the end of Appendix III.

Unfortunately, the qualitative nature of these statements precludes any unequivocal statement as to their validity. Accordingly, it is worth while to seek another less direct but more rigorous description of the entropy evolution of the test volume.

Consider the total steady-state entropy balance for our volume V (de Groot 1952*c*),

$$(13) \qquad \int_V \frac{\partial s}{\partial t}\, dV = -\int_V \operatorname{div} \frac{(\mathbf{J}_q - \sum \mu_k \mathbf{J}_k + s\mathbf{v})}{T}\, dV + \int_V \sigma\, dV = 0,$$

where s is the entropy per unit volume and $\mathbf{v}$ is the velocity of the center of mass relative to V. For an ideal solution in the approximation that the total latent heat production shows insignificant variations with concentration (or temperature) and that the temperatures T_1 and T_2 lie in regions where the components of $\mathbf{J}_k$ in the growth direction vanish, the variation of the entropy production rate between a corrugated and flat interface becomes (see Appendix III)

$$(14) \qquad \Delta \int_V \sigma\, dV \cong \Delta \int_V \operatorname{div} s\mathbf{v}\, dV = \Delta \int_a s\mathbf{v}\cdot\mathbf{n}\, da = v a \Delta \overline{s(T_1)},$$

where $\overline{s(T_1)}$ is the average entropy per unit volume at temperature T_1 and $v = |\mathbf{v}|$ is the speed of advance of the interface. Since Δs is experimentally always positive, this demonstrates the low relative entropy production of a non-planar configuration. Furthermore, since the variation on the right-hand

side of (14) is carried out isothermally and since the enthalpy per unit volume in the solid is relatively insensitive to local composition and defect structure changes, this becomes

$$\Delta \int_V \sigma \, dV \cong -\frac{va\Delta\overline{f(T_1)}}{T_1}, \tag{15}$$

where $\bar{f}$ is the average Gibb's free energy per unit volume. Thus, the principle of minimum entropy production is manifested in cellular growth by the conservation of free energy in the solid solute segregation and (possibly) in the strain energy of defect structures.

It is interesting to note that (15) implies a dominant role of the diffusive entropy production in the determination of interface morphology, for to the extent that

$$\Delta \int \frac{\text{div } \mathbf{J}_q}{T} dV \sim 0, \tag{16}$$

which was established in Appendix III, there is no mechanism available to create chemical free energy from thermal energy at the rate required by (15).

While it is not clear as yet how to interpret the phenomenon in a precise mechanistic way, there appears to be an important connection between the principle of minimum entropy production and Hamilton's principle. For a single particle system in a non-conservative force field this latter is (Whittaker 1944)

$$\int_{t_0}^{t_1} (\delta T + \sum_{r=1}^{3} Q_r \delta q_r) dt = 0 \qquad \text{(minimum)}, \tag{17}$$

where T is the total kinetic energy and $\sum_{r=1}^{3} Q_r \delta q_r$ is the work done by all the forces in an arbitrary displacement of the co-ordinates q_r. In general the Q_r are time-dependent. In an alloy system in the steady state the forces associated with diffusion gradients and the change in chemical potential at a phase boundary can be assumed to be derived from an average potential P, which is a function of the co-ordinates only, so we can write approximately

$$\delta \int_{t_0}^{t_1} \left[(T-P) + \int \sum_{r=1}^{3} Q'_r \delta q_r \right] dt = 0 \qquad \text{(minimum)}. \tag{18}$$

This can be interpreted to mean that the particle follows a trajectory with the highest possible value of the potential P throughout consistent with the constraints. With suitable averaging it also seems plausible to suppose that an assembly of particles all starting out at some base potential at time t_0 should attain the highest possible potential or free energy at some later time t_1 in agreement with the inferences of the principle of minimum entropy production.

The qualitative result of the analysis leading to equation (15) should be re-emphasized since it is perhaps a novel one. It states that this dissipative system passes through states of *maximum* free energy consistent with the

constraints. This points up the danger of applying the equilibrium principle of minimum free energy to any part of a dissipative system unless the process is an extremely slow one.

While the tendency towards maximum free energy states has only been demonstrated for the steady-state alloy solidification process, it appears to have a qualitative applicability to all dissipative processes in nature. The possible extension of these ideas to other phenomena will be outlined in a later section.

The Solute Distribution

Whatever the steady-state interface morphology, there remains the necessity that (substantial) equilibrium be maintained at every point on the interface. This is only possible along the sides of the cells (with their continuously decreasing temperature) if a solute distribution can be provided which constitutionally matches the interface temperature distribution.

With a starting alloy of normal constitution and of sufficiently high concentration, this is automatically supplied by the pile-up of solute on the liquid side of the interface (see Fig. 2). If we presume, in line with the theoretical discussion above, that the cells extend themselves to the maximum consistent with the constraints so as to assure the optimum production of chemical and strain energy in the final solid, the diffusion field at the tip of the projections must satisfy the continuity relation that the actual thermal field $(\nabla T)_L$ and the constitutional thermal field $(\nabla T)_C$, derived from the solute distribution, be congruent, i.e.,

$$(\nabla T)_L = (\nabla T)_C = \left(\frac{dT}{dC}\right)_L (\nabla C)_L, \tag{19}$$

where $(dT/dC)_L$ is the liquidus slope obtained from the constitution diagram. In the terminology of the Chalmers' school this means that constitutional supercooling must be eliminated at the cell tips. The limiting case in which $(\nabla C)_L$ for a flat interface satisfies (19) defines the condition for onset of cellular growth (Walton *et al.* 1955).

An estimate of the solute distribution for long cells and for $(\nabla T)_S > (\nabla T)_L$ can be obtained by imposing on the solution of the linear diffusion equation

$$C_L(x) \sim Ae^{-(v/D)x} + C_0, \tag{20}$$

which originates at a cell cusp, the condition that at the latter point

$$(\nabla T)_L \cong (\nabla T)_S = \left(\frac{dT}{dC}\right)_L (\nabla C)_L. \tag{21}$$

The calculation of the value of x in (20) which satisfies (19) gives an estimate of the cell length which is of the order of that observed (see Appendix II).

It remains to make an estimate of the cell spacing, d. The controlling constraint is the requirement that there be appreciable lateral mass transfer to assure the solute balance in the system. The condition for this is the requirement that an atom be able to move from the tip of the cell to an

intermediate point in a time of the same order that it takes the interface to move a similar distance. Hence,

$$d \sim \frac{D}{v}. \tag{22}$$

This leads to values of the spacing within a factor of about two of those observed (cf. Tiller and Rutter 1956, Table V) and shows the right qualitative variation with the variable v. This estimate does not, however, account for the variation with $(\nabla T)_L$ observed by Rutter and Chalmers (1953) and Tiller and Rutter (1956).

DENDRITE FORMATION

Dendritic Growth into Alloy Melts

In the discussion thus far we have ignored any crystallographic effects at the interface. This is a reasonable approximation for slight changes in the profile of the interface since the supersaturation (or supercooling) required to maintain steady-state growth is relatively constant over the whole interface. The observations bear this out since for conditions slightly more severe than the critical ones defined by equation 19, the corrugations or cells are quite smooth and featureless, and the crystallography appears only in the orientation and length of the corrugation or cell boundaries. We naturally expect crystallographic effects to appear as soon as the cusps are deep enough to bare an appreciable area of different low index plane to the liquid. This is because the supersaturation conditions are different for different crystal faces. According to the principle of minimum entropy production, for a given velocity preferred growth will occur on those faces which have the lowest chemical entropy production as indicated by relation (12). This can rationalize the dependence of cell boundary orientation and the tendency towards side-branching on equivalent preferred planes when the cell cusps become deep enough. As the growth conditions become more severe, the field components at right angles to a primary preferred growth direction of a cubic crystal approach a condition wherein (19) can be satisfied in that direction and there will be then a tendency towards side-branching from the newly bared faces of low dissipation. Branching, however, is incompatible with local steady state so an unstable condition arises.

An over-all steady state of minimum entropy production can still be maintained if an available coupled mechanism of decreasing local entropy production allows the system to enter an oscillatory mode. Figure 3, showing a

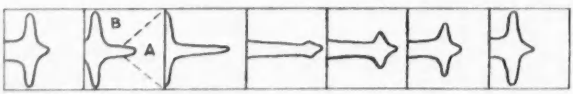

FIG. 3. Representative cyclic configuration near an advancing dendrite tip.

series of qualitative pictures equally spaced in time of a dendrite tip, indicates that this is in fact what happens. The decreasing local entropy production

which sustains the oscillation presumably occurs in the build-up of solute and latent heat which occurs as the branches and dendrite cores make their alternating forward spurts. It is further necessary to presume that a region of constitutional supercooling oscillates between regions A and B on Fig. 3 to anticipate each spurt so that the sudden latent heat build-up can be accommodated.

Since the local entropy production is now a function of time it is obvious that (3) can no longer describe the details of the process. However, the principle of minimum entropy production might be preserved by forming a double variation integral,

$$\delta^2 \iint \sigma \, dV \, dt = 0 \text{ (minimum)}. \tag{23}$$

If σ could then be expressed as a suitable quadratic function of independent field variables and their time rates of change then the equivalent Lagrangian field equations would give the required oscillatory solutions. The mathematical complexities, of course, preclude any detailed procedure of this type, but in principle it would seem to represent the situation adequately.

The frequency of oscillation is determined by the relaxation time of the diffusion field since this is the slowest process in the system. This is the time to transmit an interaction across the dendrite spacing d, so the frequency

$$\nu \sim \frac{D}{d^2}, \tag{24}$$

and by (22) the branch spacing

$$a = \frac{v}{\nu} \sim \left(\frac{vd}{D}\right) \cdot d \sim d \tag{25}$$

as is usually observed.

The application of the total entropy balance (13) to a variation between a dendritic and a flat interface is complicated by the fact that (15) may no longer be a very good approximation because of the concentration dependence of the latent heat production. However, there is little doubt that (15) still qualitatively describes the process and that we can interpret the stored free energy in the final solid as an indication of the system's tendency towards minimum entropy production.

In the previous section we proposed that no constitutional supercooling occurs at the tips of cells on a solidifying interface and in this one we have found it necessary to propose a region of supercooling oscillating between the dendrite tips and the adjacent interdendritic spaces in steady-state growth. Plaskett and Winegard (1958) have demonstrated the existence of constitutional supercooling ahead of a slowly growing, non-steady-state dendritic interface by observing the development of equiaxed grains in that region. It may be that the nucleating regions are the pockets of supercooling required by our analysis of dendritic growth, or it may be that a more extensive, continuous region of supercooling develops ahead of a non-steady interface. In either case, the extent of these regions cannot be appreciably greater than

the diffusion length D/v which was about 10 microns for their conditions. Accordingly, nucleation of the new grains must have occurred very close to the growing interface.

Dendritic Growth into Pure Melts

Weinberg and Chalmers (1951) have demonstrated that dendritic growth only occurs in pure melts if there is an appreciable region of liquid supercooling ahead of the interface. A typical observation in commercial pure ingots is a top surface skin of dendrites which presumably derives from the supercooling caused by radiation and convection from this uninsulated surface. This process is almost inherently a non-steady-state one because of the experimental difficulties in producing a moving zone of supercooling.

As before, there is a choice of solidification paths compatible with the constraints and phenomenological equations (thermal conduction and chemical reaction only). In this case the only important constraint is that the latent heat production and the coupled thermal field be compatible with the supercooled surroundings and boundaries. The interface morphology is accordingly very flexible under these conditions.

If we examine the dominant thermal conduction term in terms of an equivalent quasi-stationary process described by the variation principle (3) we form the qualitative conclusion that dendritic growth reduces the entropy production as compared to a flat interface by distributing the latent heat source as intimately as possible within the sink, shortening the transport paths and lessening the average thermal gradients. The corresponding increase in the available energy state is provided by the increase of surface energy.

GROWTH OF CRYSTALS FROM THE VAPOR

We generally note in sublimation processes a rather greater sensitivity to crystallography than in solid–liquid reactions. This is due in part to the great sensitivity of growth rates to the supersaturation and to the existence of different growth mechanisms and saturation conditions on different crystal faces. Nonetheless, the same thermodynamic principles should apply in solid–gas reactions as above. Application of these principles may often be simplified by assuming (with some justification) a quasi-stationary state in the transport fields, since in this case (3) applies.

While we reserve a full discussion of this complicated problem to a later contribution, it is interesting to note that the existence of efficient surface transport mechanisms may result in the freeing of certain of the transport forces. This means, as a result of Prigogine's theorem, that at the steady state, the conjugate fluxes vanish. If we have two components of surface flow on a metal whisker or crystal with low entropy production rate, then two components of the external diffusion and (or) convection (depending on whether there is an impure or pure vapor environment) fields may be freed. These will evidently be the two angular components in spherical co-ordinates so the diffusion or convection fields can be (approximately) spherically symmetric, irrespective of the interface morphology. The rationalization of the

high observed growth rates of metal whiskers (Sears 1955; Coleman and Sears 1957) and snow crystal dendrite branches requires just this sort of mass transport configuration.

It is interesting to consider in this respect the experiment of Bunn (1949). In two-dimensional crystallization from a solution he observed a circular solute distribution about an approximately square crystal. In the discussions, these results were discounted by F. C. Frank because a surface diffusion mechanism was unable to rationalize them. In the light of the present work it would seem attractive to postulate an alternative surface transport mechanism—perhaps some sort of monolayer viscous transport—which would explain the results.

FURTHER APPLICATIONS OF THE PRINCIPLE OF MINIMUM ENTROPY PRODUCTION

The principle of minimum entropy production appears to have qualitative applicability to all dissipative processes in nature. This is particularly evident if we regard as an approximate corollary the statement that "a dissipative system passes through states of *maximum available energy* compatible with the constraints". In the case of a system proceeding towards a steady state this is exemplified by the build-up of potential energy and the maintenance of high dynamic efficiency in the steady state. Good examples of this are the thermal diffusion cell, the steady-state alloy growth considered here, the vortex in the bath tub drain, or the history of the adult biological organism.

In the many common processes which are proceeding towards equilibrium we invariably note the tendency to pass through states of high available energy. Ostwald's rule for chemical reactions (Darken and Gurry 1953*a*), which notes that many reactions pass preferentially through metastable states before reaching the ground state, appears to be closely related to this principle. The many exceptions to the rule appear to express nothing more than the rate dependence of the entropy production, i.e., fast reactions will tend to go through higher energy states than slow ones and very slow ones will tend to go directly to the ground state. Many examples of such a rate dependence are familiar in metallurgical transformations.

Finally, one can qualitatively extend the application of the principle to the evolution of both the universe and the species by noting the local tendency towards organization as universal dissipation proceeds.

SUMMARY

The principle of minimum entropy production (or energy dissipation) has been applied to the dissipative processes involved in metal crystal growth and this procedure leads to a satisfactory rationale of surface morphology. It is proposed that in solidification from an alloy melt, diffusion supplies the dominant source of entropy production, and the system tends to minimize this by arranging the morphology in such a way as to conserve available energy through solute segregation. In a supercooled pure melt, the morphology is arranged for low entropy production by distributing the latent heat source

uniformly within the sink, i.e., by a dendritic formation which exhibits corresponding states of high surface energy.

ACKNOWLEDGMENTS

The author is indebted to Drs. R. G. Summers-Gill of McMaster University and W. A. Tiller of Westinghouse Research Laboratories for their comments on the manuscript.

REFERENCES

BROWN, W. B. 1958. Trans. Faraday Soc. **54**, 772.
BUNN, C. W. 1949. Discussions Faraday Soc. **5**, 132.
COLEMAN, R. V. and SEARS, G. W. 1957. Acta Met. **5**, 131.
DARKEN, L. S. and GURRY, R. W. 1953*a*. Physical chemistry of metals (McGraw-Hill Book Co., Inc., New York), p. 311.
——— 1953*b*. Physical chemistry of metals (McGraw-Hill Book Co., Inc., New York), p. 266.
DE GROOT, S. R. 1952*a*. Thermodynamics of irreversible processes (North-Holland Publishing Co., Amsterdam), p. 196.
——— 1952*b*. Thermodynamics of irreversible processes (North-Holland Publishing Co., Amsterdam), p. 98.
——— 1952*c*. Thermodynamics of irreversible processes (North-Holland Publishing Co., Amsterdam), p. 99.
——— 1952*d*. Thermodynamics of irreversible processes (North-Holland Publishing Co., Amsterdam), p. 102.
KELLEY, K. K. 1935. U.S. Department of the Interior, Bureau of Mines, Bulletin 383, p. 60.
PLASKETT, T. S. and WINEGARD, W. C. 1957. Trans. Am. Soc. Metals, **51**.
PRIGOGINE, I. 1955. Introduction to thermodynamics of irreversible processes (Charles C. Thomas, Publisher, Springfield, Illinois), p. 75.
RUTTER, J. W. and CHALMERS, B. 1953. Can. J. Phys. **31**, 15.
SEARS, G. W. 1955. Acta Met. **3**, 361.
TILLER, W. A. and RUTTER, J. W. 1956. Can. J. Phys. **34**, 96.
WALTON, D., TILLER, W. A., RUTTER, J. W., and WINEGARD, W. C. 1955. Trans. Am. Inst. Mining Met. Engrs. **203**, 1023.
WEINBERG, F. and CHALMERS, B. 1951. Can. J. Phys. **29**, 382.
WHITTAKER, E. T. 1944. A treatise on analytical dynamics (Dover Publications, New York), p. 248.

APPENDIX I

To simplify the entropy production expression,

$$\sigma_V = \sigma_1+\sigma_2 = \frac{1}{T}\left(\mathbf{J}_q\cdot\mathbf{X}_q+\sum \mathbf{J}_k\cdot\mathbf{X}_k\right), \tag{26}$$

we obtain directly from (5) and (8)

$$\sigma_1 = \frac{K}{T^2}(\nabla T)^2. \tag{27}$$

For a binary alloy

$$\mathbf{J}_1 = L_{11}\mathbf{X}_1+L_{12}\mathbf{X}_2 = L_{11}(\mathbf{X}_1-\mathbf{X}_2) \tag{28}$$

and

$$\mathbf{J}_2 = L_{21}\mathbf{X}_1+L_{22}\mathbf{X}_2 = -L_{11}(\mathbf{X}_1-\mathbf{X}_2) \tag{29}$$

since (de Groot 1952*d*)

$$L_{11} = -L_{12} = -L_{21} = L_{22}. \tag{30}$$

Thus

$$\sigma_2 = L_{11}(\mathbf{X}_1-\mathbf{X}_2)^2/T. \tag{31}$$

Neglecting the T dependence of equation (7) and using Fick's relation

$$\mathbf{J}_1 = -D\nabla C_1, \tag{32}$$

we obtain for a dilute, ideal solution,

$$\sigma_2 = D\frac{R}{C_1}(\nabla C_1)^2. \tag{33}$$

The units of the concentration C_1 are mole fractions. Since R is the gas constant per mole, we convert σ_2 to unit volume and finally obtain equation 11. To compare σ_1 and σ_2 at the critical condition defined by equation 19 we obtain

$$\sigma_V = \left[\frac{K}{T^2}+\frac{DR\rho_2}{M_2C_1}\left(\frac{dC_1}{dT}\right)_L^2\right](\nabla T)^2. \tag{34}$$

Using the critical values for the 0.03% tin in lead alloy given in Tiller and Rutter's Table V and the values for lead, $\rho_2 = 10.5$ g/cm^3, $M_2 = 207.2$ g/mole, and $K_L = 0.04$ cal/sec cm °C, we find that on the liquid side of the critical flat interface, the diffusion term per unit volume is about three times the conduction one.

APPENDIX II

To make an estimate of cell or dendrite lengths we assume the liquid solute distribution (20)

$$C \sim C_0+A\,e^{-v/Dx}$$

originating at point B on Fig. 2 and impose the condition

$$\nabla C(0) = (\nabla T)_S\left(\frac{dC}{dT}\right)_L \tag{35}$$

to determine A. We then solve for the value $x = x'$, which satisfies

$$\nabla C(x') = (\nabla T)_L\left(\frac{dC}{dT}\right)_L. \tag{36}$$

This procedure should lead to reasonable estimates provided $(\nabla T)_S > (\nabla T)_L$.

Taking as typical values those given by Tiller and Rutter (1956, pp. 105 and 116), we have:
$C_0 = 0.01\%$ tin in lead, $v = 0.0167$ cm/sec, $(\nabla T)_L = 5.4°$ C/cm, $D = 7\times10^{-5}$ cm^2/sec, and from handbooks $L = 5.89$ cal/g, K_S(Pb) $= 0.08$ cal/sec cm °C, K_L(Pb) $= 0.04$ cal/sec cm °C, ρ(Pb) $= 10.5$ g/cm^3, ρ(Sn) $= 7.3$ g/cm^3.
We obtain $(\nabla T)_S$ from the continuity relation for a flat interface,

$$K_S(\nabla T)_S = K_L(\nabla T)_L+v\rho L. \tag{37}$$

This gives $(\nabla T)_S = 15.6°$ C/cm and satisfies our condition that $(\nabla T)_S > (\nabla T)_L$.

Carrying out the calculation we obtain $A = 0.022\%$ and $x' = 45$ microns. This is in order of magnitude agreement with the cell profiles shown in Tiller and Rutter's Fig. 27.

APPENDIX III

For the simplification to equation (14) of the expression for the difference in total entropy balance between a flat and corrugated interface, we note first that for steady state and for reference temperature points T_1 and T_2 well removed from the interface

$$\Delta\int_V \frac{\partial s}{\partial t}\,dV = \Delta\int_V \frac{\operatorname{div}\sum \mu_k \mathbf{J}_k}{T}\,dV = 0. \tag{38}$$

Accordingly we can write

$$\Delta\int_V \sigma\,dV = \Delta\int_V \frac{\operatorname{div} s\mathbf{v}}{T}\,dV + \Delta\int_V \frac{\operatorname{div}\mathbf{J}_q}{T}\,dV, \tag{39}$$

and it remains to indicate under what conditions the last term on the right-hand side is negligible compared with the first.

We can write the heat balance at constant pressure

$$\operatorname{div}\mathbf{J}_q = -C_p\rho\frac{\partial T}{\partial t} + Q \tag{40}$$

where Q represents the heat sources and sinks in the system. This will include the latent heat source, chemical free energy converted to heat in the reaction and diffusion fields, and a sink corresponding to conversion of thermal energy into chemical energy. This latter could arise from thermal diffusion effects, but because of the relatively small magnitude of such effects, this term can be considered as negligible. We can now invoke the steady-state condition that

$$\frac{\partial T}{\partial t} = -v\frac{\partial T}{\partial x}, \tag{41}$$

divide by T and integrate to give

$$\Delta\int_V \frac{\operatorname{div}\mathbf{J}_q}{T}\,dV = \Delta\int_V \frac{C_p\rho v}{T}\frac{\partial T}{\partial x}\,dV + \Delta\int_V \frac{q\,dV}{T} + \Delta\int_a \frac{\rho v L}{T}\,da, \tag{42}$$

where q represents the non-latent chemical heat sources and L is the latent heat.

We now consider each of the terms on the right-hand side separately. A non-zero value of the first one would arise mainly from the exchange of some liquid and solid in the solidification zone giving rise to a change ΔC_p. We can, therefore, approximate this term for the system considered in Appendix II by

$$\Delta_1 \sim \overline{\frac{\Delta C_p \rho_2 v}{T}\frac{\partial T}{\partial x}}\int dV \sim \pm 1\times 10^{-6}\,\frac{a}{T}\ \text{cal/deg sec}. \tag{43}$$

In this estimate we have used $\Delta C_p = 0.001$ cal/g (Kelley 1935), $\rho_2 = 10.5$ g/cm^3, $v = 0.0167$ cm/sec, and $\partial T/\partial x \sim 10°$ C/cm. The effective volume of integration is probably zero to the first order, but as a conservative estimate we have represented it by one tenth of a solidification zone of 45 microns width.

The second term represents the conversion of free energy in the diffusion field into enthalpy. For ideal solutions this is zero since the enthalpy of mixing is zero. More generally it may contribute another (usually fractional) term to the right-hand side of (14). For a regular solution (Darken and Gurry 1953*b*) the difference in the rate of heat evolution in the diffusion field per degree absolute is estimated to be

$$\Delta_2 \sim \frac{1}{10}\left[RT\alpha\frac{v\rho_2}{M_2}\Delta C_1\frac{a}{T}\right] \sim \pm 1.5\times 10^{-5}\frac{a}{T}\ \text{cal/deg sec} \tag{44}$$

where α generally lies between ± 2 (we have chosen $\alpha = \pm 1$ here) and ΔC_1 is the concentration difference between the interface and the alloy concentration (0.00014 in this calculation). The bracketed quantity is the rate of heat evolution for a flat interface and the difference between this and that for a non-planar interface, Δ_2 (which is zero to the first order), is taken as one tenth of the whole.

Finally, the latent heat L depends on the interface concentration (or temperature). We therefore make the estimate

$$\Delta_3 \sim \overline{\frac{\rho_2 v}{T}\frac{\Delta C_1}{}\frac{\partial L}{\partial C_1}}\int_a da \sim \pm 1\times 10^{-5}\frac{a}{T}\ \text{cal/deg sec.} \tag{45}$$

In this we have taken $L = 5.89\,(1\pm C_1)$ cal/g and $\Delta C_1 = 1/40A$. (See Appendix II for calculation of A.) The mean change in one or the other direction is probably about $\frac{1}{4}A$, but to the first order the positive changes will cancel the negative ones so we have reduced this even more.

For comparison we estimate the right-hand side of (15) as

$$-v\Delta\bar{f}\frac{a}{T} \sim 1\times 10^{-4}\frac{a}{T}\ \text{cal/deg sec.} \tag{46}$$

In evaluating this we have assumed an ideal solution and a segregation of 0.01% existing in one twentieth of the solid volume.

As an alternative we can estimate the maximum change in entropy production due to change in the diffusion fields by means of equation 12. This change should be of the order of one-half the entropy production existing in a volume near a flat interface which is equal to the actual volume of the solidification zone. For an ideal solution this gives

$$\frac{1}{2}\overline{\frac{DR\rho_2}{M_2C_1}(\nabla C_1)^2}\int dV \sim 0.4\times 10^{-4}\frac{a}{T}\ \text{cal/deg sec} \tag{47}$$

in rough agreement with (46).

For comparison, the corresponding conduction term is

$$\overline{\frac{\Delta K}{T^2}(\nabla T)^2}\int dV \sim 0.7\times 10^{-5}\frac{a}{T}\ \text{cal/deg sec.} \tag{48}$$

Here, the main change would appear to be through the possible exchange of some liquid for solid with a corresponding change in the thermal conductivity.

We have taken $\Delta K = 0.04$ cal/sec cm, $\nabla T = 15.6°$ C/cm and the effective volume as one tenth of the solidification zone. The term appears to be small compared with the diffusion term (47).

The general result of these calculations is to indicate that the quantity

$$\Delta \int_V \frac{div\, \mathbf{J}_q}{T}\, dV$$

is made up of a sum of terms of variable sign which to the first order vanishes. Our estimates of the second-order variations suggest that in ideal solutions and most others as well, these terms can be neglected in comparison to (46) and that equations (14) or (15) give an accurate description of the solidification process. Even if there exist cases where the latter terms are not negligible, the inference remains valid that solid solute segregation attending non-planar growth is a measure of the system's attainment of minimum entropy production, since the segregation term in (14), like the entropy production change, is always positive.

SPINS OF EXCITED STATES OF Os^{188} [1]

W. J. KING AND M. W. JOHNS

ABSTRACT

Seven excited states of Os^{188} populated through the beta decay of Re^{188} have been studied by gamma–gamma angular correlation experiments. The data for the various cascades fit the following theoretical functions: (all gamma-ray energies are in kev and the description following each cascade refers to the first transition) 478–155 (2–2–0, 99.7% *E*2, δ +ve), 931–155 (0–2–0), 672–633 (2–2–0), 97% *M*1, δ −ve *or* 3–2–0, 94% *M*1, δ −ve *or* conceivably 4–2–0), 828–633 (2–2–0, 98% *M*1, δ −ve *or* conceivably 3–2–0, 80% *M*1, δ −ve), 1132–633 (0–2–0), and 1308–633 (2–2–0, 98% *M*1, δ −ve). Some attenuation occurred in the correlations involving the 155-kev gamma ray. The *K*-conversion coefficients for the 478- and 633-kev transitions have been measured as 0.023 ± 0.003 and 0.010 ± 0.002 respectively, confirming the *E*2 character for these transitions obtained by angular correlation. These results, coupled with data concerning log *ft* values and gamma-ray intensities, lead to the following spin and parity assignments for levels in Os^{188}: 155 (2+), 633 (2+), 1086 (0+), 1306 (2+ *or* 3+), 1461 (2+), 1765 (0+), 1941 (2+), and 1958 (1+ *or* 2+).

The 631–137 correlation data in Os^{186} was found to fit an attenuated 2–2–0 function with the first transition 99% *E*2 and δ −ve. This result supports the established decay scheme for this nucleus.

INTRODUCTION

Seventeen-hour Re^{188} has been the subject of many investigations but no well-established decay scheme was proposed until 1956. In that year, workers in this laboratory (Johns *et al.* 1956) and at the Bartol Research Foundation (Potnis 1956) independently arrived at essentially the decay scheme of Fig. 1. An investigation of the shapes of the beta-spectra feeding the 0- and 0.155-Mev levels of Os^{188} (Nielsen and Nielsen 1958) revealed that both spectra show departures from the allowed shape which establish them as non-unique first-forbidden transitions. Since the spins of these two levels are known to be 0+ and 2+, one is forced to assign spin 1 and negative parity to the ground state of Re^{188}. From the gamma-ray intensity balance, Johns *et al.* (1956) found that all of the excited states of Os^{188} shown in Fig. 1 are fed by first-forbidden beta transitions. Hence one is led to expect that the spins of all levels of Os^{188} excited by the beta decay of Re^{188} must be 0, 1, 2, or 3 with positive parity. Levels with higher spins can only be excited indirectly through cascading gamma rays.

Both angular correlation (Potnis *et al.* 1956) and internal conversion measurements (Nielsen and Nielsen 1958; Johns *et al.* 1956) led to a 2+ assignment for the 0.633-Mev level, but nothing was known concerning the spins of the weakly populated higher levels. This paper describes a series of angular correlation experiments whose results lead to an assignment of spins to five of these states.

The beta decay of Re^{186} populates levels in Os^{186} at 0.137 and 0.768 Mev above the ground state (Metzger and Hill 1951) and leads to the 631–137

[1]Manuscript received January 6, 1959.
Contribution from Hamilton College, McMaster University, Hamilton, Ontario.

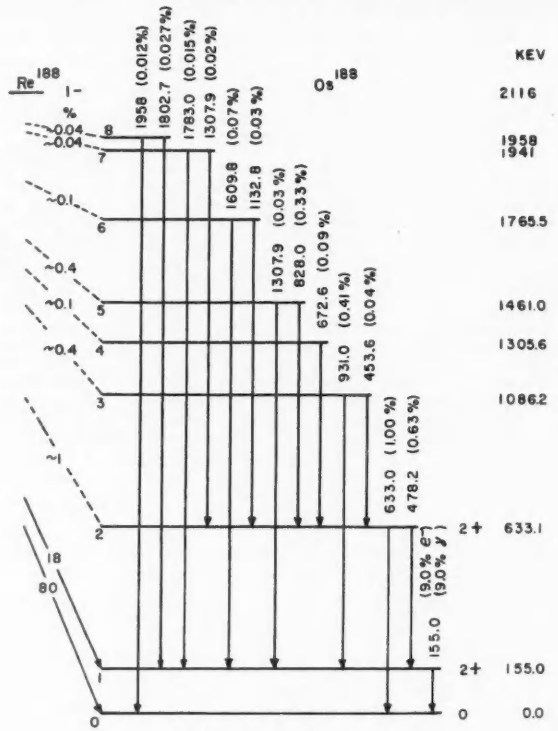

FIG. 1. Decay scheme of Re^{188}.

cascade* in 0.025% of the disintegrations (Porter *et al.* 1955; Johns *et al.* 1956). The angular correlation of this cascade was studied by Hurley and Jastram (1954) but their results are available only in abstract form. In view of this fact, it was felt worth while to re-examine this cascade as part of the present investigation. It has been clearly shown by many workers that the 0.137-Mev transition is pure $E2$ and that hence the cascade of interest is of the type J–2–0, with all the available evidence suggesting that $J = 2$.

Recent investigations of the decay of Ir^{186} and Ir^{188} by Diamond and Hollander (1958) have identified a number of the higher spin states belonging to the ground-state rotational sequence 0, 2, 4, 6 . . . in Os^{186} and Os^{188}. A similar sequence has been established in Os^{190} (Scharff-Goldhaber *et al.* 1958) and the presence of two low-lying spin 2 states has been confirmed in all these nuclei and in Os^{192} by the Coulomb excitation experiments of Barloutaud *et al.* (1958). The last-named workers also reinterpret earlier data available concerning Os^{192} (Baggerley *et al.* 1955) to make it fit the pattern established from the other osmium nuclei. None of the states with spin greater than two have been identified in the rhenium decay processes, but all of this data will

*In the interests of brevity, gamma-ray cascades will be simply labelled by the energies of the two gamma rays in kev without explicit mention of units.

be used in the discussion of the results of the present experiments and is summarized in Fig. 7.

APPARATUS AND METHOD

The gamma-ray angular correlation spectrometer consisted of two scintillation detectors mounted in the same horizontal plane with the source located 7 cm from the front face of the detectors. Each detector consisted of a $1\frac{1}{2}$ in. $\times$ 1 in. NaI(Tl) crystal coupled to an R.C.A. 5819 photomultiplier. The angle between the fixed and movable detectors could be altered by rotating the latter in a horizontal plane about a vertical axis through the source. Coincidences between photons detected in the two detectors were observed with a Bell–Graham–Petch (1952) coincidence circuit modified in the following manner. The pulse from each photomultiplier was inverted, clipped by means of a 200-ohm cable to 4×10^{-8} seconds, and then amplified with two Hewlett-Packard wide-band amplifiers (460A and 460B) in cascade. The amplified pulses were fed to a 404A pentode limiter whose output led to the fast coincidence circuit. The resolving time of this unit was adjustable from 2×10^{-9} to 2×10^{-8} seconds, with a value of 8×10^{-9} seconds being commonly employed. The output of the fast coincidence unit recorded coincidences between all pairs of gamma rays detected in the scintillators. Energy selection was performed in both side channels by means of single-channel pulse height analyzers (Tracerlab RL1-6). The outputs of these channels and the fast coincidence unit were fed to a triple coincidence unit of resolving time 5×10^{-7} seconds whose output yielded coincidences between pulses of selected heights. Under the conditions of the experiment, the maximum usable source strength was determined by the number of pulses reaching the side-channel analyzers rather than by the accidental coincidence rate. Wherever possible, unwanted low-energy pulses were prevented from reaching these analyzers by removing the associated X rays or gamma rays with 1 g/cm^2 lead or 0.6 g/cm^2 tin absorbers placed over the face of the detector.

Sources were prepared from spectroscopically pure natural rhenium or rhenium enriched to 98.2% in the heavier isotope. The solid sources consisted of about 1 mg of polycrystalline metallic powder while the liquid sources consisted of rhenium dissolved in hydrogen peroxide. The liquid and solid sources gave essentially the same anisotropy for all the Re^{188} cascades but there was a noticeable difference between the two for the Re^{186} cascade. Most of the Re^{188} data was obtained from metallic sources, irradiated in sealed quartz vials about 10 mm long and 1 mm in diameter, and used in an unopened condition. The primary beta rays were absorbed by inserting the source vial in a hole drilled along the axis of a carbon cylinder mounted concentrically with the axis of rotation of the spectrometer. The position of this cylinder was adjusted to locate the small source accurately at the center of the circle defined by the intersection of the horizontal axes of the crystals. The correct vertical position was first determined by visual inspection and then the lateral position adjusted until the counting rate in the movable detector was constant to within 1% as the detector was rotated from the 90° to the 270° position.

For each cascade studied, an experimental resolution curve was obtained by adjusting a variable delay line in the fast coincidence unit. The gamma–gamma correlation data was then obtained with the circuit set at the delay corresponding to the peak of this curve. The chance rate was measured either by inserting a sufficient delay in one channel leading to the fast coincidence circuit or by inserting a large delay in one of the side channels. Under the conditions of these experiments the chance rate was never more than 5% of the true coincidence rate.

Before studying a cascade, each side-channel spectrum was determined and the "windows" set on the desired portions of the photopeaks of the two gamma rays involved using the same geometry as that in which the correlation data was to be recorded. With these window settings, the number of coincidence counts and the number of counts in the movable counter obtained in 15 minutes were recorded for a sequence of angles ranging from 90° to 180° and back in 22.5-degree steps. Following this sequence, the side channels were recalibrated to check for drifts, and, in the rare cases where appreciable drifts had occurred, the data was rejected. For most of the cascades, the sequence was repeated until several thousand coincidences had been recorded at each of the five angles. For each angular position, the ratio $R(\theta) = C_t(\theta)/N(\theta)$ was formed. In this expression, $N(\theta)$ is the cumulated number of counts recorded in the movable detector for a given angular position while $C_t(\theta)$ is the cumulated number of observed coincidences at the same position corrected for the small number of chance coincidences present. The function $R(\theta)$ embodies the experimental information concerning the angular correlation of the cascade under study. It can be seen that this method of treating the data not only corrects for decay but also introduces a first-order correction for errors in centering of the source on the axis and for small window drifts. Using the least-squares method outlined by Rose (1953), the function $R(\theta)$ was used to determine the A'_ν coefficients in the expansion

$$R(\theta)/C = 1 + A'_2 P_2(\cos\theta) + A'_4 P_4(\cos\theta)$$

where C is a constant of proportionality of no further importance.

These A'_ν coefficients were corrected for the finite angular resolution of the detectors in the manner described by Rose (1953), using the functions explicitly evaluated by him for a source-to-crystal-face distance of 7 cm and $1\frac{1}{2}$ in. × 1 in. detectors.* The A_ν's so obtained represent the true coefficients

*It was pointed out by the reviewer that the correction factors for the finite size of the detectors given by Rose are not strictly applicable to an experiment in which only the photopeak pulses are counted. To answer this criticism, the authors have determined the correction factors experimentally, using the method described by Lawson and Frauenfelder (1953) but setting the pulse height analyzer to accept only the photopeaks of the gamma rays from the collimator. The solid-angle correction factors were determined for radiations of energy 0.129 Mev (Os^{191}), 0.411 Mev (Au^{198}), and 1.33 Mev (Co^{60}). As might be expected, the experimental factors obtained were slightly less than those computed by Rose; the differences ranging from zero at 0.129 Mev to a maximum of 0.2% for the J_2/J_0 ratio and 0.8% for the J_4/J_0 ratio at an energy of 1.3 Mev. These measurements indicate that the A_2 values in Table I should be reduced by 0.4% while the A_4 values should be reduced by amounts ranging from 0.8 to 1.2%. Since other uncertainties in the measured coefficients are of the order of 10%, the systematic errors introduced by the use of Rose's coefficients are trivial and do not alter any of the conclusions reached.

for the selected pair of gamma rays combined with whatever contribution from other gamma rays was included in the windows chosen. A discussion of these effects is included in the section dealing with experimental results.

EXPERIMENTAL RESULTS

Figure 2 presents the gamma-ray spectrum of Re^{188} as observed in either scintillation detector. This fails to reveal the detailed structure of the spectrum

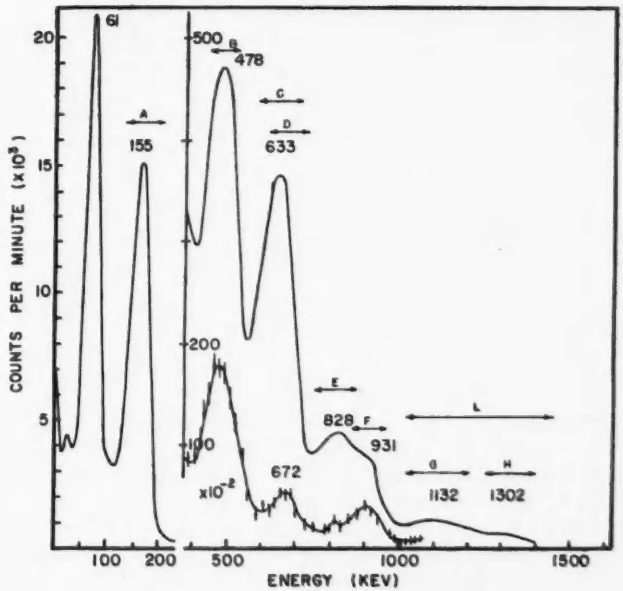

FIG. 2. Scintillation counter spectrum of the gamma rays of Os^{188}. Lower curve—gamma rays in coincidence with the 0.155-Mev radiation.

obtained with magnetic spectrometers (Johns *et al.* 1956) but is sufficiently well defined to enable one to pick out any cascade of Fig. 1 without too much interference from the others. The windows used in the angular correlation studies are indicated above the photopeaks. The weak 0.672-Mev peak is masked by the much stronger 0.633-Mev peak in the single-channel spectrum; its intensity, deduced from the coincidence spectrum, agrees with the value obtained with the magnetic spectrometer.

The experimental data for the cascades of Os^{188} are presented in Fig. 3 and in Table I. Each figure shows the experimental points, the least-squares fit to these points, and the least-squares fit to the data corrected for the finite solid angle of the detectors. The differences between the two curves are not large and small errors in these corrections would not significantly alter the conclusions which are presented in the following pages. Table I gives the

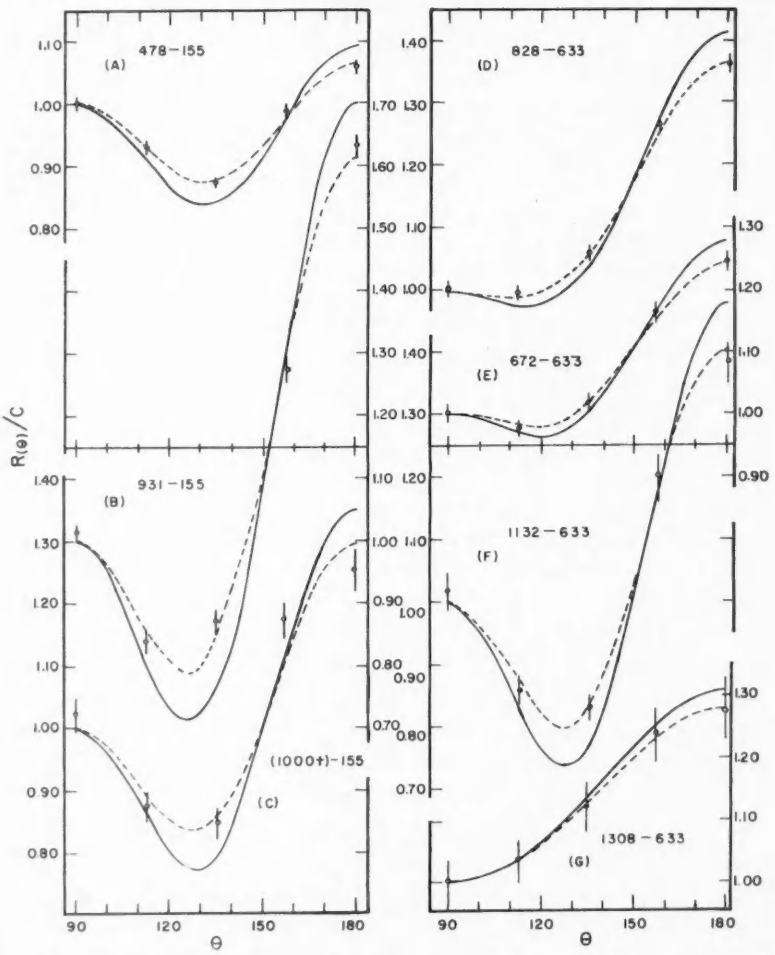

FIG. 3. Experimental angular correlation functions for the gamma rays of Os^{188}. The broken line represents the least-squares fit to the experimental points. The solid line is the correlation function corrected for the finite solid angle of the detectors.

solid-angle-corrected coefficients for each cascade together with pertinent information concerning the experimental conditions. It also presents the coefficients for the "pure" cascades obtained by subtracting the effect of interfering cascades. These background-corrected cascades are shown in Fig. 5. The difficulty in estimating the magnitude of such backgrounds of course leads to rather large uncertainties in the "pure" coefficients; in some cases, these large uncertainties made it impossible to reach unique spin assignments.

The standard deviations on the experimental coefficients quoted in Table I

TABLE I

Angular correlation functions of Os^{188} and Os^{186}

Energies of cascading gamma rays, kev	Type of source	Windows used (see Fig. 2)	Number of counts at each position	Average rate per minute	Intensity of interfering cascades	A_2	A_4
478–155 Os^{188}	Liquid	A and B	5500	20	10% due to	-0.004 ± 0.013	$+0.199 \pm 0.019$
	Solid		4500	20	931–155 etc.	-0.030 ± 0.029	$+0.213 \pm 0.042$
	Total		10000	20		-0.016 ± 0.010	$+0.205 \pm 0.015$
					Pure 478–155	-0.048 ± 0.010	$+0.162 \pm 0.015$
931–155 Os^{188}	Solid	A and F	1500	4	20% due to (1000+)–155	$+0.271 \pm 0.032$	$+0.588 \pm 0.048$
					Pure 931–155	$+0.313 \pm 0.060$	$+0.640 \pm 0.080$
(1000+)–155 Os^{188}	Solid	A and L	1300	10		$+0.101 \pm 0.060$	$+0.379 \pm 0.088$
828–633 Os^{188}	Liquid	C and E	4500	9	12.5% due to 1308–633	$+0.193 \pm 0.008$	$+0.133 \pm 0.013$
	Solid		4500	9	12.5% due to 1132–633	$+0.216 \pm 0.019$	$+0.146 \pm 0.029$
	Total		9000	9		$+0.205 + 0.010$	$+0.139 + 0.012$
					Pure 828–633	$+0.222 \pm 0.02$	$+0.026 \pm 0.025$
672–633 Os^{188}	Solid	D and D	5000	8	17% 828–633 8% 1132–633 8% 1308–633	$+0.131 \pm 0.023$	$+0.124 \pm 0.034$
					Pure 672–633	$+0.103 \pm 0.05$	$+0.06 \pm 0.07$
1308–633 Os^{188}	Solid	C and H	900	1	Pure 1308–633	$+0.180 \pm 0.005$	$+0.017 \pm 0.006$
1132–633 Os^{188}	Solid	C and G	2000	2	50% 1308–633	$+0.153 \pm 0.037$	$+0.479 \pm 0.055$
					Pure 1132–633	$+0.13 \pm 0.08$	0.94 ± 0.12
631–137 Os^{188}	Solid	137 Photopeak and all pulses above	8000	2	None	-0.026 ± 0.003	$+0.061 \pm 0.003$
	Liquid	200 kev	3000	2	None	-0.056 ± 0.003	$+0.123 \pm 0.004$

were computed using equation (30) of Rose's (1953) article. In using this equation, it is assumed that the standard deviations in the individual points determine only the relative weight of the points in the least-squares analysis, but that there is no uncertainty in the position of the points themselves. This assumption seems to be reasonable when the number of coincidences at each point is large. In such cases, the standard deviations of the coefficients calculated in this manner give a true indication of the sensitivity of the function to be fitted to variations in the coefficients. However, when the number of coincidences recorded at each position is small, the uncertainties in the positions of the individual points may well be the dominant factors in determining the errors in the coefficients. The appropriate expression for calculating the standard deviations in the coefficients is then equation (20) of Rose's paper. In the analysis of the results, both equations were used and found to give essentially the same standard deviations except for the 672–633 and 1308–633 cascades; for these, the limits of error deduced from equation (20) were several times larger than those deduced from equation (30). A casual inspection of Fig. 3 shows that the least-squares fit to the experimental points for these two cases is considerably better than one would expect on the basis of the statistical accuracy of the individual points. This suggests that larger limits of error are more realistic than those quoted in Table I for these two cascades.

The 478–155 and the 828–633 cascades were studied with both solid and liquid sources. Since both types of source gave essentially the same correlation function, the two sets of data were averaged in interpretation as shown in Table I.

Although Potnis *et al.* (1956) had demonstrated from angular correlation studies that the 0.633-Mev level was 2+ in character and Johns *et al.* (1956) had measured α_k for the 0.478-Mev radiation, the discrepancies in the mixing ratio for the 0.478-Mev radiation between the two sets of results made it seem worth while to remeasure the internal conversion coefficients of the 0.478- and 0.633-Mev transitions. These were obtained by using a source of rhenium enriched in the heavier isotope and a 50-cm beta-ray spectrometer. The values of 0.023 ± 0.003 and 0.010 ± 0.002 obtained for the K-conversion coefficients of the 0.478-Mev and 0.633-Mev transitions respectively are in good agreement with the theoretical values for pure $E2$ transitions and the recent experimental values of Nielsen and Nielsen (1958).

The 631–137 cascade of Os^{186} was examined with both solid and liquid

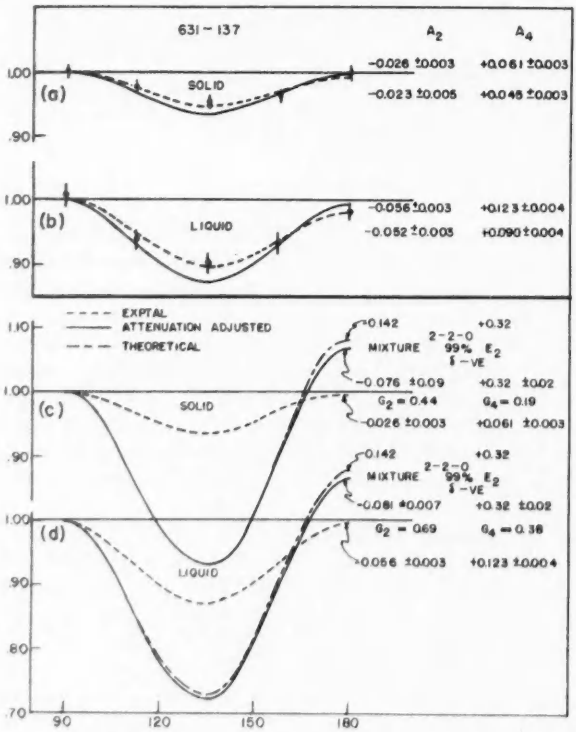

FIG. 4. Angular correlation functions for the 631–137 cascade of Os^{186}; (*a*) and (*b*) present the data for the solid and liquid sources respectively; the dotted curves fit the observed points, the solid curves are corrected for the finite solid angle of the detectors; (*c*) and (*d*) present the analysis of the data on the basis of attenuation.

sources. In order to prevent overloading of the side-channel analyzers by X rays and low-energy gamma rays, absorbers of 0.9 g/cm² lead and 0.6 g/cm² tin were used over the high-energy and low-energy detectors respectively. About 3000 coincidences were recorded at each angle for the liquid source and about 8000 coincidences per position for the solid source at an average coincidence rate of 2 per minute. The results of these experiments, presented in Fig. 4, (*a*) and (*b*), show clearly the existence of attenuation due to the reorientation of the nuclei in the relatively long-lived intermediate state (8×10^{-10} seconds; McGowan 1951).

DISCUSSION OF EXPERIMENTAL RESULTS

From Fig. 1, it is evident that the only cascades of Os^{188} present in appreciable intensity involve the ground state and one of the 2+ states at 0.155 and 0.633 Mev. Hence the second component of all the cascades studied is pure *E*2 and the experimental functions may be compared with theoretical curves for cascades of the form *J*–2–0 where *J* is restricted to the integral values from 0 to 3 by the fact that the ground state of Re^{188} is 1− in character. The choice $J = 4$ is also possible for levels excited from higher-lying states of spin 2 or 3.

The coefficients A_ν can be evaluated as the product of two terms (Biedenharn and Rose 1953), each of which depends on only one transition in the cascade.

$$A_\nu = A_\nu^{(1)} A_\nu^{(2)} = [A_\nu^{(1)\prime}(1-Q_1)]\times[A_\nu^{(2)\prime}(1-Q_2)]$$

where Q is the fractional intensity of the higher-order multipole in the transition. Q is equal to $\delta^2/(1+\delta^2)$ where δ is the ratio of the reduced matrix element for the higher multipole to that for the lower multipole in the same transition. In all of the cascades of concern here $Q_2 = 0$, $A_2^{(2)} = -0.5976$, and $A_4^{(2)} = -1.069$ so that the theoretical A_ν values are given directly in terms of $A_\nu^{(1)\prime}$ and Q_1. Arns and Wiedenbeck (1958) have published a convenient table of graphs showing $A_2^{(1)}$ and $A_4^{(1)}$ as a function of Q for all cases of interest. A comparison of experiment with theory is made by dividing the experimental A_2 and A_4 coefficients by the values of $A_2^{(2)}$ and $A_4^{(2)}$ given above and then examining these graphs to find a pair of $A_2^{(1)}$ and $A_4^{(1)}$ values for a given spin sequence consistent with these experimental values and a common Q value.

The lifetime of the 0.155-Mev level has been found to be 6.5×10^{-10} seconds (Sunyar 1954). This lifetime is long enough that one might expect to find some attenuation of the correlation through nuclear reorientation in the intermediate state. The effect of this attenuation is to replace the A_ν coefficients by $A_\nu G_\nu$ where the values of G_ν ($\nu = 2, 4 \ldots$) are the same for all cascades involving this intermediate state. Steffen (1955) points out that the attenuation is a function only of the lifetime of this state and the environment in which the nucleus finds itself. While one might expect some attenuation effects for cascades involving the 0.155-Mev level, none should appear for those involving the much shorter-lived 0.633-Mev level.

The 931–155 coincidence data must be corrected for contributions from gamma rays of energy greater than 1 Mev which tend to smear out the

observed correlation pattern. Even without this correction, it is obvious that this cascade can only be associated with a 0–2–0 spin sequence since none of the other possibilities can give such a large A_4 coefficient (Fig. 5, (A), and Table I).

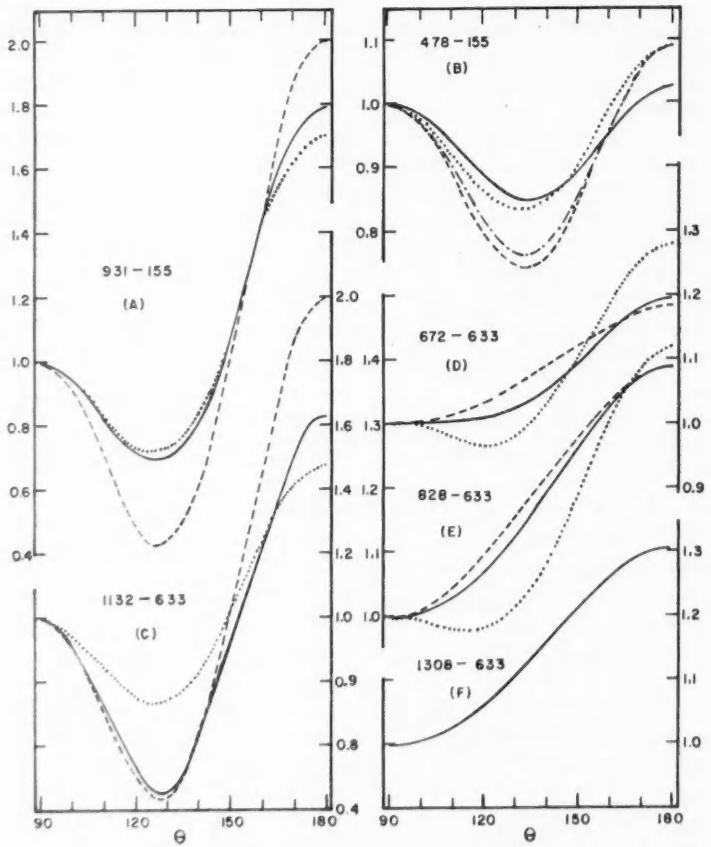

FIG. 5. Comparison of experimental and theoretical angular correlation functions in Os^{188}. The dotted curves present the experimental data corrected for the finite solid angle of the detectors. The solid curves are the "pure" experimental angular correlation functions after corrections for finite solid angle and for interfering cascades have been made. The broken curves are theoretical functions.

(A) 931–155. The "pure" experimental function and the theoretical function for a 0–2–0 cascade can be matched exactly with attenuation factors $G_2 = 0.87$ and $G_4 = 0.56$.

(B) The "pure" experimental function when corrected for attenuation using the factors of (A) above yields the heavy broken curve. It agrees closely with the theoretical curve shown for a 2–2–0 cascade with $Q_1 = 99.7\%$, δ −ve.

(C) 1132–633. The theoretical function is for a 0–2–0 cascade.

(D) 672–633. The theoretical curve is a 2–2–0 correlation function with $Q_1 = 0.03$, δ −ve.

(E) 828–633. The theoretical curve is a 2–2–0 correlation function with $Q_1 = 0.01$, δ −ve.

(F) 1308–633. The theoretical curve for a 2–2–0 cascade with $Q_1 = 0.013$ and δ −ve fits the experimental data exactly.

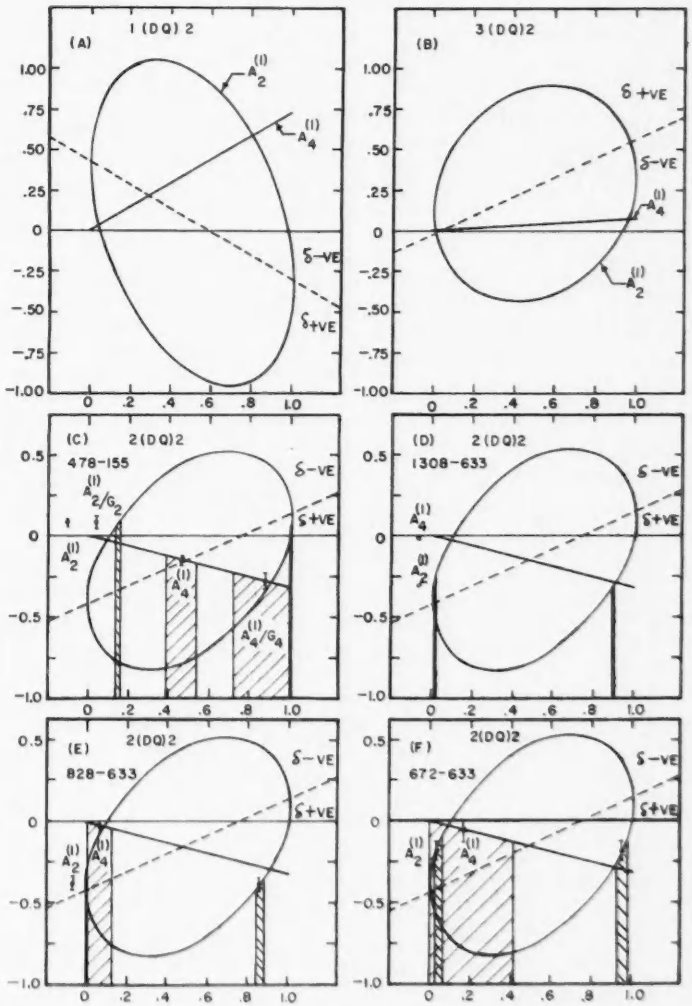

FIG. 6. Evaluation of Q values from the experimental coefficients. Each figure shows the value of $A_2^{(1)}$ and $A_4^{(1)}$ as a function of Q for the cascades of Fig. 5.

(A) The spin sequence 1–2–0.
(B) The sequence 3–2–0.
(C) The sequence 2–2–0 applied to the 478–155 cascade.
(D) The sequence 2–2–0 applied to the 1308–633 cascade.
(E) The sequence 2–2–0 applied to the 828–633 cascade.
(F) The sequence 2–2–0 applied to the 672–633 cascade.

However, the "pure" experimental coefficients are still not as large as the theoretical 0–2–0 coefficients ($A_2 = 0.358$, $A_4 = 1.142$) and one is tempted to regard the difference as due to attenuation of the type discussed above. To bring the experimental coefficients in agreement with the theoretical ones requires that $G_2 = 0.87 \pm 0.16$ and $G_4 = 0.56 \pm 0.06$. The validity of this assumption can be tested by applying these factors to the 478–155 cascade since it should be attenuated in the same way.

It is estimated that 10% of the observed 478–155 coincidence recorded may be due to the effect of higher-energy gamma rays in coincidence with the 0.155-Mev radiation. The pure correlation function which is presented in Fig. 5, (B), and whose coefficients are tabulated in Table I corresponds to $A_2^{(1)} = +0.080 \pm 0.020$ and $A_4^{(1)} = -0.152 \pm 0.015$. An inspection of Fig. 6 shows that these values rule out the cascades 1–2–0 and 3–2–0 and suggests that the cascade may be an attenuated 2–2–0. The $A_2^{(1)}$ coefficient is consistent with $Q_1 = 0.15$ or 1.0 while the $A_4^{(1)}$ coefficient yields $Q_1 = 0.46$. Application of the attenuation factors G_2 and G_4 deduced from the 931–155 cascade alters $A_2^{(1)}$ and $A_4^{(1)}$ to $+0.092 \pm 0.03$ and -0.27 ± 0.03 respectively. While the change in $A_2^{(1)}$ makes no significant change in the predicted Q values the attenuation-corrected $A_4^{(1)}$ coefficient is consistent with $Q_1 = 0.88 \pm 0.12$, thus removing the inconsistency present with the uncorrected coefficients. Figure 5, (B), presents both the correlation function for the attenuation-corrected coefficients and the theoretical 2–2–0 function for $Q = 0.997$ and δ +ve. The agreement is excellent and leads to the conclusion that the intensity of the dipole component in the 0.478-Mev transition is less than 0.5%. Support for this conclusion is obtained from the measured internal conversion coefficient for this transition which sets an upper limit of 16% on the intensity of the dipole component.

The 478–155 cascade has also been studied by Potnis *et al.* (1956). Although these workers reached the same conclusions concerning the 0.478-Mev radiation as those above, they obtained the unattenuated correlation function with solid metallic sources. The detailed shape of the 478–155 experimental function is very sensitive to the amount of the 931–155 cascade accepted by the apparatus because of the strong anisotropy of the latter cascade. In the present experiments, the "window" used for the 0.478-Mev gamma ray accepted only about half of its photopeak. Even with this window, it is estimated that 10% of the coincidences recorded were due to higher-energy gamma rays. With the wider window used by Potnis and his co-workers, it is conceivable that 30% of the coincidences were due to these radiations. Such a contribution is quite sufficient to explain the discrepancies between their experimental curves and ours. It is possible that the full correlation obtained by Potnis *et al.* was fortuitous, and that their correlation function would have been in close agreement with ours had they corrected for the coincidences caused by higher-energy gamma rays. On the other hand, it is also quite reasonable to attribute the differences between their work and the results found here to the differences in source environment in the two experiments.

The 1308–633 cascade requires no background correction so that its inter-

pretation is relatively simple. The data leads to values of -0.30 ± 0.01 and -0.016 ± 0.005 for $A_2^{(1)}$ and $A_4^{(1)}$ respectively. The 2–2–0 spin sequence is the only physically acceptable cascade which can simultaneously give a large negative $A_2^{(1)}$ and a small negative $A_4^{(1)}$ coefficient (Fig. 5, (F), and 6, (D)). Thus, according to the data, the 1.308-Mev transition must be a dipole–quadrupole mixture with $Q_1 \sim 0.02$ and δ −ve and the spin of the 1.941-Mev level is 2. By arbitrarily increasing the limits of error on $A_4^{(1)}$ to 0.03, the data can be fitted to a 3–2–0 correlation function with $Q_1 = 0.12$ and δ −ve. While the spin choice of 3 for the 1.941-Mev level cannot be rigorously excluded on the basis of the angular correlation data, it seems to be effectively ruled out by the fact that the $\log f_0 t$ value (8.2) for beta transitions to this level is appropriate to a first-forbidden non-unique beta decay and considerably too small for a first-forbidden transition of the unique type. Thus it is concluded that the 1.941-Mev level has spin 2 and even parity.

The large A_4 coefficient associated with the 1132–633 experimental correlation function suggests that one of the cascades contributing to this data is 0–2–0 in character. Since the 1308–633 cascade is definitely not of this type, the 1132–633 cascade must be. Subtraction of the 1308–633 cascade background from the experimental data leads to the "pure" correlation coefficients of Table I and the solid curve of Fig. 5, (C). Although these do not represent the complete anisotropy expected for a pure 0–2–0 cascade the differences can easily be due to uncertainties in the magnitude of the background from the 1308–633 cascade. It is concluded that the level at 1.765 Mev has zero spin. Independent evidence for the existence of a zero-spin level above 1.3 Mev is afforded by the strongly anisotropic correlation function obtained for the coincidences between all gamma rays above 1 Mev and the 0.155-Mev transition.

The 828–633 experimental correlation function has been corrected for the background of coincidences due to two higher-energy cascades as shown in Table I and Fig. 5, (E). While the "pure" A_2 coefficient is quite insensitive to the magnitude of this background, the "pure" A_4 coefficient depends on it strongly and can be driven negative if the intensity of this background is made large enough. The "pure" coefficients of Table I are consistent only with a 2–2–0 cascade in which Q_1 is less than 0.02 and δ is negative (Fig. 6, (E)). However, if the estimated background intensity is increased from the 25% upper limit used to the rather implausible value of 33%, the data can also be interpreted in terms of a 3–2–0 cascade with $Q \sim 0.2$ (δ −ve). The spin 3 assignment for the 1.461-Mev level is inconsistent with other evidence available. The $\log f_0 t$ value for the beta transitions to this level has been established as 8.4 from the gamma-ray intensity balance. While failure to detect weak gamma rays makes this value a lower limit, it is inconceivable that the careful search for weak gamma rays in the energy region 0.2 to 0.7 Mev carried on earlier in this laboratory (Johns *et al.* 1956) could have missed radiation of sufficient intensity to raise this value to more than 8.7. The value 8.4 lies between the well-established 8.6 and 8.1 $\log f_0 t$ values for the first-forbidden non-unique transitions to the 0.155-Mev and ground

states of Os^{188} and is much too small for the first-forbidden unique transition required if the 1.461-Mev level is 3+ in character. Although the absence of the ground-state transition from this level seems to suggest a spin assignment greater than 2, the upper limit of 0.02% set on the intensity of this transition (Johns *et al.* 1956) is quite inadequate to help one in deciding between the 2+ and the 3+ choice. In the light of the angular correlation data and the f_0t value for the beta transitions to this level, it is concluded that the 1.461-Mev level has spin 2 and positive parity.

One third of the observed 672–633 coincidences may be due to background from other cascades, and consequently the "pure" coefficients tabulated in Table I show rather large experimental errors. In fact when the errors are considered the coefficients (Fig. 6, (F)) are consistent with the following three possible cascades, in order of decreasing probability: 2–2–0 with $Q_1 = 0.03$ (δ −ve), 3–2–0 with $Q_1 = 0.06$ (δ −ve), and 4–2–0.

It is impossible to distinguish between these three choices on the basis of the angular correlation measurements alone. If the spin 4 assignment for the 1.306-Mev level is accepted, the beta transition feeding this level must be of negligible intensity and undetected gamma rays of a total intensity of 0.09% must be present to feed this level. Since possible transitions from the 1.461- or 1.941-Mev levels to this state are masked by other stronger radiations, it is impossible to test this assumption directly. However, in view of the small energy release involved in such radiations and the general intensity pattern of the decay process of Fig. 1, it seems very unlikely that radiations of sufficient intensity to feed this level in .09% of the disintegrations can occur. There seems to be no way of deciding between the assignments 2+ and 3+ from either the angular correlation data or the *ft* value for the beta transition to the 1.306-Mev level. Nor can the presence of a 1.306-Mev gamma ray be used to reach a decision, since such a radiation fits into the decay scheme in three places. The assignments actually made in Fig. 1 are based on coincidence results and on the known doublet line profile of this gamma ray as seen with the 50-cm beta-ray spectrometer (Johns *et al.* 1956). No evidence concerning the existence of a 1.306-Mev ground-state transition exists at the present time. Therefore, one can only conclude that the spin of the 1.306-Mev level is 2 or 3 with positive parity with a reservation that the spin 4 assignment is remotely possible.

In principle, it should be possible to use the angular correlation technique to determine the spin of the 1.958-Mev level by studying the 1802–155 cascade. However, all cascades involving the 0.155-Mev radiation proved difficult to handle because very few of the 0.155-Mev photons are coincidence makers while their high intensity results in overloading in the side-channel analyzers unless weak sources are used. On the other hand, most of the 0.633-Mev photons are potential coincidence makers and strong sources can be used when the 0.155-Mev photons are removed with lead absorbers. It is estimated that the maximum achievable coincidence rate for the 1802–155 cascade would have been an order of magnitude smaller than for any of the other cascades studied. One can draw certain conclusions concerning the

spin of the 1.958-Mev level from the decay scheme of Fig. 1. The fact that the beta transition to this level has a $\log f_0 t$ value of 8.0 characteristic of a first-forbidden transition leads to the conclusion that this state has positive parity. The fact that the gamma-ray transitions from this level to the zero-spin ground state and the 2+ state at 0.155 Mev are roughly equal in intensity restricts the spin assignment of the 1.958-Mev level to the choices 1 or 2.

The 631–137 cascade of Os^{186} must be of the form J–2–0 with J restricted to the values 1 or 2 by virtue of the fact that the gamma-ray transitions from the 0.768-Mev level to the ground state and the 2+ state at 0.137 Mev are roughly equal in intensity. Since the measured A_4 coefficients for both solid and liquid sources are positive while the A_4 coefficient for a 1–2–0 cascade is zero or negative no matter what mixing occurs, the data of Table I and Figs. 4 and 6 shows clearly that the angular correlation pattern must be interpreted as a 2–2–0 cascade. The fact that the coefficients for the liquid and solid sources are different suggests that the attenuation due to nuclear reorientation in the intermediate state occurs with one or both types of sources. The experimental solid-source data yields $A_2^{(1)} = +0.044$ which gives $Q = 0.12$ (δ −ve) or $Q = 0.99$ (δ +ve) and $A_4^{(1)} = -0.057$ consistent with $Q = 0.18$. The experimental liquid-source data yields $A_2^{(1)} = +0.094$ associated with $Q = 0.15$ (δ −ve) or $Q = 0.995$ (δ +ve) and $A_4^{(1)} = -0.115$ consistent with $Q = 0.36$. Steffen (1955) points out that attenuation factors are not smaller than the "hard core" value of 0.2 for G_2 and 0.11 for G_4. Therefore the $A_2^{(1)}$ and $A_4^{(1)}$ coefficients corrected for attenuation (i.e., $A_2^{(1)}/G_2$ and $A_4^{(1)}/G_4$) must lie between the experimental values for the solid curve and +0.22 and −0.52 respectively. The range of values allowed for $A_2^{(1)}$ limits Q to values from 0.16 to 0.26 (δ −ve) or 0.99 to 1.00 (δ +ve or −ve) while the range for $A_4^{(1)}$ limits Q to values between 0.36 and 1.00.

The only value of Q consistent with both the $A_2^{(1)}$ and $A_4^{(1)}$ ranges is 0.99 ± 0.01 (δ +ve or −ve). This choice imposes essentially no limits on the G_2 factor and requires G_4 to be 0.19 and 0.38 for the solid and liquid sources respectively. On this basis, it is concluded that the spin of the 0.768-Mev level is certainly 2+, and that the 0.631-Mev transition is about 99% $E2$.

No internal conversion data exists to check these conclusions but independent angular correlation data has been provided by Hurley and Jastram (1954). These workers, using electrochemically deposited sources (Jastram 1958), found an unattenuated 2–2–0 angular correlation pattern for this cascade corresponding to $Q = 0.99$ with δ −ve.

INTERPRETATION

Figure 7 presents the information available concerning low-lying levels in four even–even osmium nuclides together with additional details concerning the beta-ray and gamma-ray transitions involved in the decay of Re^{186} and Re^{188}. The following observations concerning the level systematics suggest that these nuclei fall in the transition region between spheroidal nuclei with well-developed rotational bands and nearly spherical nuclei with a vibrational level structure.

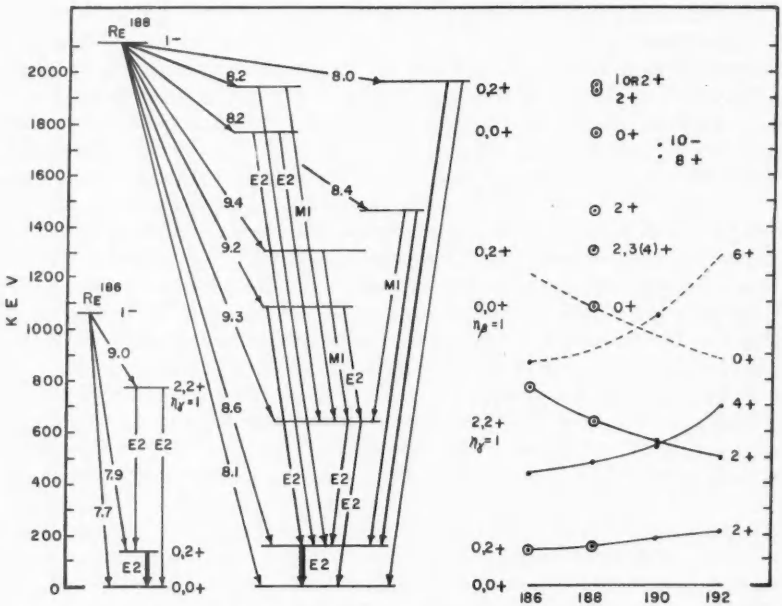

FIG. 7. Excited states in Os^{186}, Os^{188}, Os^{190}, and Os^{192}. The decay schemes for Re^{186} and Re^{188} show the positions of the levels, the log *ft* values of the beta groups feeding them, and the multipole classifications of the gamma rays wherever they are known. The decay scheme of Re^{188} is drawn to illustrate the interpretation in the discussion. The data for the high spin states of Os^{186} and Os^{188} and for the levels of Os^{190} and Os^{192} is taken from the references discussed in the introduction.

(*a*) The spacings of the 0, 2, 4, 6 . . . levels of the ground-state rotational bands show increasing departures from those expected for pure rotational levels as the mass number increases; thus, while in Os^{186} the 4+ and 6+ states are respectively 4% and 10% too low, the departures amount to 12% and 20% in Os^{190}.

(*b*) The excitation energy of the second 2+ state (hereafter referred to as 2′+) which is observed in all four nuclei decreases rapidly with increasing mass number and has almost reached the position expected for a two-phonon vibrational state when the mass reaches 192.

(*c*) The ratio of the *ft* values for the beta transitions from Re^{186} to the two lowest states of Os^{186} is 1.6±0.4 in good agreement with the value 2.0 expected for a pure rotational structure. However, in the Re^{188} decay, the corresponding ratio, 3.2±0.6, already shows the effect of departures from pure rotational behavior.

(*d*) The ratio of the reduced *E*2 transition probabilities for the $2' \rightarrow 2$ and $2' \rightarrow 0$ transitions is found to be 2.7±0.6 and 2.6±0.3 in Os^{186} and Os^{188} respectively. These ratios are to be compared with a value of 1.43 predicted for a pure rotational structure and a value of infinity for a pure vibration. All

these facts point to the conclusion that we are dealing here with nuclei in which a strong coupling exists between the rotational and vibrational modes of collective motion.

The $2+'$ level in Os^{188} has been interpreted as the $(2, 2)+$ state associated with a gamma vibration (Alder *et al.* 1956; Nielsen and Nielsen 1958). This interpretation is supported by comments (*b*) and (*d*) above and by the predominantly $E2$ character of the $2' \rightarrow 2$ transition.

An alternative description of the 0, 2, 4, 2′ levels in all four nuclei is given by Davydov and Filippov (1958), who have investigated the energy levels to be expected from the rotation of an asymmetric top. They show that the rotational levels, instead of being a simple 0, 2, 4 . . . sequence, now include the spin values 0, 2, 2, 3, 4, 4, 4, 5, 5 . . . The spacing of these levels is evaluated in terms of the parameter γ, which determines the deviation of the nucleus from axial symmetry. In particular, the authors express the ratio of the energies of the 2′ and 2 states and various reduced transition probabilities in terms of the parameter γ. Table II presents a comparison between the results of their theory and experiment for the four osmium nuclides. In this table γ is

TABLE II

			$[b(E2{:}2' \rightarrow 2)]/[b(E2{:}2' \rightarrow 0)]$		$[b(E2{:}2' \rightarrow 0)]/[b(E2{:}2 \rightarrow 0)]$	
	$E(2')/E(2)$	γ	Theor.	Expt.	Theor.	Expt.
Os^{186}	5.6	16.6°	3.2	2.7	0.062	
Os^{188}	4.1	19.2°	4.7	2.6	0.072	0.16
Os^{190}	3.0	22°	8.2		0.067	0.047
Os^{192}	2.6	24°	>12		0.055	0.059

evaluated from the ratio of the excitation energies of the two spin 2 levels and the values so obtained used to obtain the other ratios in the table. The experimental results in the last column are obtained from Coulomb excitation data (Barloutaud *et al.* 1958).

In a spherical nucleus with its pure harmonic structure, the one-phonon state has spin 2, the two-phonon state is a degenerate triplet with three possible spins, 0, 2, or 4, and so on. The addition of nucleons to an unfilled shell introduces interactions between these particles and the collective motions which remove these degeneracies and gradually alter the level spacings so that the description in terms of phonon excitation becomes inappropriate. For these nuclei, it is useful to consider the collective motions in terms of rotational and vibrational levels, each with their characteristic form of level spacing. Since the strength of the coupling between collective and particle motions does not change the number of collective levels but merely alters their spacing, one can still use the phonon label on a level in a spheroidal nucleus to indicate the level with which it is associated in a spherical nucleus. This labelling is particularly useful in transition nuclei where the level structure reveals qualities of both spheroidal and spherical nuclei. Thus, in even–even nuclei, the first member of the ground-state rotational band ($K = 0$ $I = 2$) can be

labelled a one-phonon excitation, while the $K = 0$ $I = 4$ member of the same band, the $K = 2$ $I = 2$ (gamma vibration), and the $K = 0$ $I = 0$ (beta vibration) can all be labelled as two-phonon excitations.

In the language of the last paragraph, the 2+ state in all four nuclei of Fig. 7 would be called a one-phonon state while the 2′+ and 4+ levels would both be labelled two-phonon states. It is attractive to consider the 0+ state of Os^{188} at 1.086 Mev as the third member of the two-phonon triplet and label it as a two-phonon beta vibration. The level of excitation of this beta vibration should decrease with increasing mass number much as the 2′+ gamma vibration does and the expected trend has been indicated in Fig. 7. Unfortunately, none of the processes studied in the other nuclides of this series would be expected to populate such a 0+ level with appreciable intensity. It is, however, interesting to note that a 0+ state at about the same excitation has been identified in Er^{166} (Fraser and Milton 1955), which is located in the transition region just above the 82-neutron closed shell.

If the 0+ state at 1.086 Mev is accepted as the candidate for the two-phonon beta vibration, the 1.306-Mev level is probably the first-excited state of a rotational band based on this vibrational level. This assignment for the 1.306-Mev level agrees with the preferred experimental spin value and leads to a reasonable value for the moment of inertia of the nucleus in the ground state. The *ft* values for beta transitions to these two levels have a ratio of 1.6, in agreement with the value 2.0 expected for a pure rotational structure. However, one would expect the transition from the 0, 2+ level of this rotational band to the 2, 2+ level, associated with the two-phonon gamma vibration to be predominantly $E2$ in character. In fact, the observed transition is predominantly $M1$ (whether the angular correlation data be interpreted in terms of spin 2 or 3 for the 1.306-Mev level). This relaxation of the K-selection rule is another indication that the collective model represents an oversimplification of the situation in this nuclide. An alternative choice for the second member of the rotational band based on the beta-vibrational level is the 2+ state at 1.461 Mev. This choice has nothing to recommend it since it leads to a very small moment of inertia of the nucleus. Moreover, the ratio of the *ft* values for beta transitions to the 1.461- and 1.086-Mev levels is only 0.16 and the 0.828-Mev transition de-exciting the 1.461-Mev level is predominantly $M1$.

It is impossible to be definite about the interpretation of the four remaining levels of the decay scheme of Fig. 7 since the excitation level is now high enough that particle excitations are likely to be in competition with collective motions. It does seem likely that the levels at 1.765 and 1.941 Mev are the 0, 0+ and 0, 2+ members of a third rotational band since these levels show much the same pattern of de-excitation as that from the pair of levels at 1.086 and 1.306 Mev. Support for this view comes from the value of ~ 1 for the ratio of the *ft* values for beta transitions feeding this pair of levels. On the other hand, the de-excitation of the 1.941-Mev level is predominantly by $M1$ radiation, which is again K-forbidden.

One striking feature of the decay scheme of Fig. 1 or Fig. 7 is the absence of ground-state transitions and the intensity of transitions feeding the 2′+

state at 0.633 Mev. There are four levels in the decay scheme which feed both the 2′+ and the 2+ levels of Fig. 7 and in every case, the reduced transition probability for the transition to the 2′+ level is from 3 to 40 times greater than that for the transition from the same level to the 2+ state. The reduced transition probabilities for the unobserved ground-state transitions are of course smaller still. This indicates that the internal structure of the nucleus in the upper levels is more like that in the 2+′ level than in the ground or 2+ states.

Wilets and Jean (1956) and Mottelson (1957) have pointed out that the transition nuclei are "softer" against shape deformation than either the truly spherical nuclei or the strongly deformed spheroidal nuclei. The observations of the last paragraph would suggest that Os^{188} is such a "soft" nucleus and that a gamma vibration of energy 0.633 Mev is sufficient to bring the nucleus into a new equilibrium shape which it retains for many of the higher excitations.

This view seems to deny the possibility of regarding the Os^{188} nucleus as an asymmetric rigid rotator since the basic premise of Davydov and Filippov's treatment is that the asymmetry is built into the nuclear shape in the ground state and is unaltered by the excitation of the rotational levels. Of necessity, their treatment can say nothing about the location of the 0+ beta vibration since such a vibration by definition is a shape distortion which does not affect the axial symmetry of the nucleus. Despite these conclusions, Davydov and Filippov's theory is very attractive since it leads for the first time to detailed numerical predictions concerning level spacings and transition probabilities for these transition nuclei. In contrast, the approach of the Bohr–Mottelson theory through beta and gamma vibrations leads only to order of magnitude estimates—what might be facetiously called a "soft theory" for "soft nuclei".

ACKNOWLEDGMENTS

The sources used in these experiments were obtained through the courtesy of the United States Atomic Energy Commission and Brookhaven National Laboratories. We should like to thank the National Research Council of Canada and the Ontario Research Foundation for financial assistance in the form of grants and the Imperial Oil Company for Fellowships awarded to one of the authors (W. J. K.).

The authors would also like to acknowledge the helpful correspondence held with Professor Philip Jastram of Ohio State University and consultations with Professors M. A. Preston and J. D. Bankier of this laboratory. The assistance of A. Artna, R. Price, R. Goodman, and D. MacArthur in recording the data is gratefully acknowledged.

REFERENCES

ALDER, K., BOHR, A., HUUS, T., MOTTELSON, B., and WINTHER, A. 1956. Revs. Modern Phys. **28**, 432.

ARNS, R. G. and WIEDENBECK, M. L. 1958. Phys. Rev. **111**, 1631 and privately circulated report.

BAGGERLEY, L. L., MARMIER, P., BOEHM, F., and DUMOND, J. W. M. 1955. Phys. Rev. **100**, 1364.
BARLOUTAUD, R., LEVESQUE, A., LEHMANN, P., and DUIDORT, J. 1958. J. phys. radium, **19**, 60.
BELL, R. E., GRAHAM, R. L., and PETCH, H. E. 1952. Can. J. Phys. **30**, 35.
BIEDENHARN, L. C. and ROSE, M. E. 1953. Revs. Modern Phys. **25**, 729.
DAVYDOV, A. S. and FILIPPOV, G. F. 1958. Nuclear Phys. **8**, 237.
DIAMOND, R. M. and HOLLANDER, J. M. 1958. Nuclear Phys. **8**, 143.
FRASER, J. S. and MILTON, J. C. D. 1955. Phys. Rev. **98**, 1173A.
HURLEY, J. P. and JASTRAM, P. S. 1954. Phys. Rev. **95**, 627A.
JASTRAM, P. S. 1958. Private communication.
JOHNS, M. W., MCMULLEN, C. C., WILLIAMS, I. R., and NABLO, S. V. 1956. Can. J. Phys. **34**, 69.
LAWSON, J. S. and FRAUENFELDER, H. 1953. Phys. Rev. **91**, 649.
MCGOWAN, F. K. 1951. Phys. Rev. **81**, 1066.
METZGER, F. R. and HILL, R. D. 1951. Phys. Rev. **82**, 646.
MOTTELSON, B. R. 1957. Revs. Modern Phys. **29**, 186.
NIELSEN, K. O. and NIELSEN, O. B. 1958. Nuclear Phys. **5**, 319.
PORTER, R. T., FREEDMAN, M. S., NOVEY, T. B., and WAGNER, F. 1955. Phys. Rev. **98**, 214L.
POTNIS, V. R., DUBEY, V. S., and MANDEVILLE, C. E. 1956. Phys. Rev. **102**, 459.
POTNIS, V. R. 1956. Phys. Rev. **104**, 722.
ROSE, M. E. 1953. Phys. Rev. **91**, 610.
SCHARFF-GOLDHABER, G., ALBURGER, D. E., HARBOTTLE, G., and MCKEOWN, M. 1958. Phys. Rev. **111**, 913.
STEFFEN, R. M. 1955. Phil. Mag. **4**, 293.
SUNYAR, A. W. 1954. Phys. Rev. **95**, 626A.
WILETS, L. and JEAN, M. 1956. Phys. Rev. **102**, 788.

NOTES

ON THE CALCULATION OF THE VELOCITY OF SOUND IN SEA WATER

CHARLOTTE FROESE*

INTRODUCTION

An accurate knowledge of the velocity of sound in sea water as a function of salinity, temperature, and pressure is essential in oceanography. Tables are available but the values quoted may differ by as much as 3 m/sec from one table to the next, when the desired accuracy is to within .1 m/sec. Of these tables, the two most frequently used are by Kuwahara (1939) and by Del Grosso (1952).

Kuwahara computed the sound velocity, V_{stp}, as a function of salinity, temperature, and pressure. His calculations were based on theoretical considerations which express the sound velocity in terms of specific heat, specific volume, and compressibility of sea water. Empirical formulae were derived for these physical properties, and so the accuracy of his tables will depend mainly on the accuracy of these formulae.

More recently Del Grosso (1952) measured the velocity of sound at atmospheric pressure experimentally using modern interferometric techniques. From these results he derived an equation for V_{st0} which he believes to be accurate to within .2 m/sec.

Sound velocities at pressures up to 1000 atmospheres are currently being measured. These direct measurements are capable of greater precision than the indirect method of Kuwahara, and at the moment a considerable discrepancy exists between the two. For example, for $V_{35,0,0}$ Del Grosso obtained a value 3.1 m/sec higher than the one given by Kuwahara. This discrepancy is an indication of the error present in the empirical formulae used by Kuwahara. Some of them were based on measurements made as far back as 1889 and could be determined now with greater accuracy.

The purpose of this investigation was, first of all, to check Kuwahara's tables by using the same basic formulae but employing a different method. A program was written for ALWAC III-E, the automatic computer at the University of British Columbia, to perform the calculations. This program would also serve another purpose; as new measurements are made of the specific heat, specific volume, or compressibility, the same program may be used to recompute the sound velocity and compare the results with direct measurements. This paper deals entirely with the results of the first stage of the investigation. A description is given of the method by which the sound velocity was computed and the results compared with Kuwahara's tables.

*Present address: Department of Mathematics, University of British Columbia, Vancouver, B.C.

SOUND VELOCITY COMPUTATION

The velocity of sound in sea water is given by the equation

$$V = \left(-\alpha^2 \Big/ \frac{1}{\gamma}\frac{\partial \alpha}{\partial p}\right)^{\frac{1}{2}} \tag{1}$$

where

$$\frac{1}{\gamma}\frac{\partial \alpha}{\partial p} = \frac{\partial \alpha}{\partial p} + \frac{T}{JC_p}\left(\frac{\partial \alpha}{\partial t}\right)^2, \tag{2}$$

α = specific volume,

C_p = specific heat at constant pressure,

and T = temperature in degrees absolute.

The specific volume, α_{stp}, was computed using the same formulae as those employed by Kuwahara (1939) but they were rewritten in a form more suitable for computation on an automatic computer.

The specific heat of sea water was divided into two parts so that

$$C_p = C_p(st0) - \frac{T}{J}\int_0^p \frac{\partial^2 \alpha}{\partial t^2}\, dp$$

where the first is the value at zero pressure, and the second is the pressure correction term obtained from thermodynamic considerations. Kuwahara's formula was used to compute the first but none was given for the second. In order to obtain the pressure correction term, the second derivative $\partial^2\alpha/\partial t^2$ had to be evaluated. Though α is given by an analytic formula, it is too complex to warrant analytic differentiation; instead the derivative was computed numerically according to the formula

$$\alpha_n'' = (\alpha_{n+1} - 2\alpha_n + \alpha_{n-1})/h^2 + 0(h^2) \tag{3}$$

with $h = 1/2°$ C. A formula was then fitted to the results using a least squares approximation; values from the formula differed from the original data by less than 2 in 1000. From this formula the pressure correction was obtained.

According to equations (1) and (2), values of α, $(\partial\alpha/\partial p)$, and $(\partial\alpha/\partial t)$ are required in order to compute the sound velocity. As before, the partial derivatives were replaced by differences using the formula

$$\alpha_n' = (\alpha_{n+1} - \alpha_{n-1})/2h + 0(h^2), \tag{4}$$

where h was 100 decibars for the derivative with respect to pressure and $1/2°$ C for the derivative with respect to temperature. These partial derivatives occur in equation (2). The most important contribution is from the $\partial\alpha/\partial p$ term and if V is to be correct to six figures, $\partial\alpha/\partial p$ should be correct to about the same though some accuracy is gained in taking the square root. Therefore, $h = \Delta p$ had to be chosen large enough so that the difference, $\alpha_{n+1} - \alpha_{n-1}$, retained six significant figures, but small enough so that the truncation error in (4) did not affect these figures. A nearly optimum value was $\Delta p = 100$ decibars, which gave a difference of almost six figures and a truncation error of one in the sixth figure. The significance gained by increasing Δp would be offset by

an increase in the truncation error. The value of $h = \Delta t$ is not as critical since the contribution to (2) from the second term is considerably smaller.

Equations (1) and (2) were rewritten in terms of differences and the sound velocity computed for a series of values of s, t, and p.

COMPARISON OF RESULTS

The results of these calculations were compared with the values given by Kuwahara. In his tables, the sound velocity is divided into four parts so that

$$V_{stp} = V_{35.0,p} + \Delta V_t + \Delta V_s + \Delta V_{stp},$$

and each of these quantities tabulated separately. In Table I, the velocities $V_{35,0,p}$ are compared; the differences are hardly more than those due to round-off, the largest being 0.07. The same applies to Tables II and III where the temperature correction, ΔV_t, and salinity correction, ΔV_s, respectively are

TABLE I

Comparison of the velocities, $V_{35,0,p}$ in m/sec

p, decibars	ALWAC	Kuwahara	Difference
0	1445.44	1445.5	−.06
500	1454.45	1454.5	−.05
1000	1463.43	1463.4	.03
2000	1481.30	1481.3	.00
3000	1499.02	1499.0	.02
4000	1516.57	1516.6	−.03
5000	1533.92	1533.9	.02
6000	1551.05	1551.1	−.05
7000	1567.94	1568.0	−.06
8000	1584.55	1584.6	−.05
9000	1600.86	1600.9	−.04
10000	1616.86	1616.9	−.04

TABLE II

Comparison of the temperature correction, ΔV_t, in m/sec

t, °C	ALWAC	Kuwahara	Difference
−2	−9.32	−9.3	−.02
0	0.00	0.0	.00
2	8.99	9.0	−.01
4	17.62	17.6	.02
5	21.79	21.8	−.01
10	41.25	41.3	−.05
15	58.34	58.4	−.06
20	73.22	73.2	.02
25	86.18	86.2	−.02
30	97.65	97.7	−.05

TABLE III

Comparison of salinity correction, ΔV_s, in m/sec

Salinity, ‰	ALWAC	Kuwahara	Difference
30	−6.54	−6.5	−.04
33	−2.62	−2.6	−.02
35	0.00	0.0	.00
37	2.61	2.6	.01
40	6.53	6.5	.03

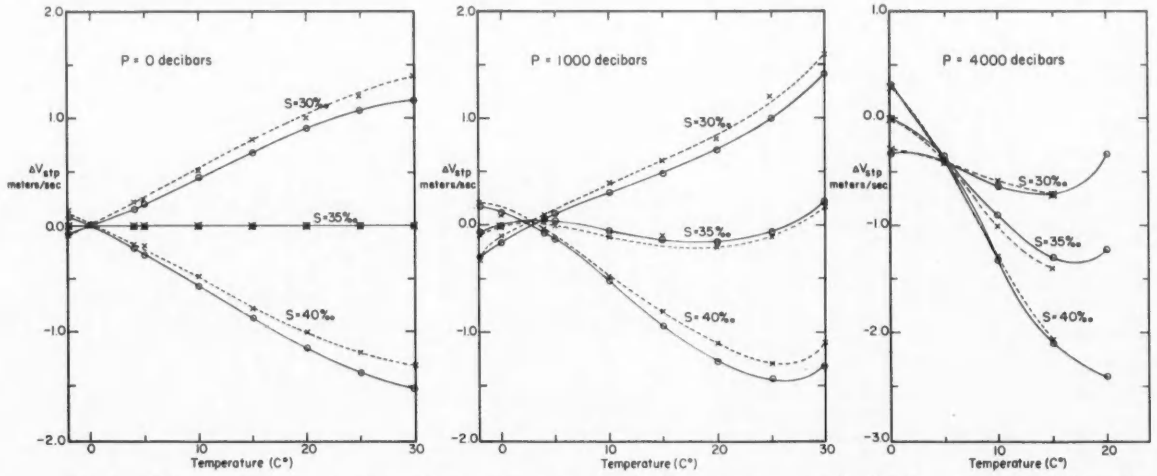

FIG. 1. Plots of ΔV_{stp} as a function of temperature for several different pressures and salinities: —○— ALWAC, —×— Kuwahara (Table IV).

given. Greater differences occur in Table IV where ΔV_{stp}, the correction for simultaneous changes in any two or more variables, are compared. These usually occur at the limits of the range where t is large. In Fig. 1, plots of ΔV_{stp} as a function of temperature for several different pressures and salinities are given both as computed by ALWAC and by Kuwahara. These indicate the relative magnitude of the differences.

TABLE IV

Comparison of $\Delta V_{stp} = V_{stp} - V_{35,0,p} - \Delta V_t - \Delta V_s$ in m/sec

		Salinity, ‰								
		30			35			40		
p, decibars	t, °C	ALWAC	K.	Diff.	ALWAC	K.	Diff.	ALWAC	K.	Diff.
0	−2	−.07	−.1	.03	.00	.0	.00	.09	.1	−.01
	0	.00	.0	.00	.00	.0	.00	.00	.0	.00
	5	.21	.2	.01	.00	.0	.00	−.27	−.2	−.07
	10	.45	.5	−.05	.00	.0	.00	−.57	−.5	−.07
	15	.70	.8	−.10	.00	.0	.00	−.87	−.8	−.07
	20	.92	1.0	−.08	.00	.0	.00	−1.14	−1.0	−.14
	25	1.09	1.2	−.11	.00	.0	.00	−1.37	−1.2	−.17
	30	1.19	1.4	−.21	.00	.0	.00	−1.53	−1.3	−.23
2000	0	−.24	−.2	−.04	.00	.0	.00	.24	.2	.04
	5	−.02	.0	−.02	−.03	.0	−.03	−.10	−.1	.00
	10	.08	.1	−.02	−.22	−.2	−.02	−.64	−.6	−.04
	15	.18	.3	−.12	−.41	−.4	−.01	−1.18	−1.1	−.08
	20	.41	.5	−.09	−.44	−.5	.06	−1.55	−1.4	−.15
	25	.88	1.0	−.12	−.18	−.2	.02	−1.57	−1.4	−.17
4000	0	−.32	−.3	−.02	.00	.0	.00	.32	.3	.02
	5	−.40	−.4	.00	−.36	−.4	.04	−.39	−.4	.01
	10	−.63	−.6	−.03	−.90	−1.0	.10	−1.32	−1.3	−.02
	15	−.70	−.7	.00	−1.30	−1.4	.10	−2.11	−2.1	−.01
		33			35			37		
6000	−2	.09	.1	−.01	.23	.2	.03	.37	.3	.07
	0	−.09	−.1	.01	.00	.0	.00	.09	.1	−.01
	2	−.37	−.4	.03	−.33	−.3	−.03	−.29	−.3	.01
	4	−.70	−.7	.00	−.71	−.7	−.01	−.73	−.7	−.03
8000	−2	.52	.5	.02	.54	.5	.04	.56	.5	.06
	0	.02	.0	.02	.00	.0	.00	−.02	.0	−.02
	2	−.56	−.5	−.06	−.62	−.6	−.02	−.70	−.7	.00
	4	−1.16	−1.1	−.06	−1.28	−1.2	−.08	−1.40	−1.4	.00
10,000	−2	1.08	1.1	−.02	.91	.9	.01	.74	.7	.04
	0	.21	.2	.01	.00	.0	.00	−.21	−.2	−.01
	2	−.70	−.7	.00	−.95	−1.0	.05	−1.20	−1.3	.10
	4	−1.58	−1.6	.02	−1.87	−1.9	.03	−2.17	−2.2	.03

The author is grateful to Dr. N. P. Fofonoff for many helpful discussions and suggestions.

DEL GROSSO, V. A. 1952. The velocity of sound in sea water at zero depth, NRL Problem S02-04, RDB Project NR 522-040.
KUWAHARA, S. 1939. Hydrographic Rev. **16** (2), 123.

RECEIVED JANUARY 14, 1959.
FISHERIES RESEARCH BOARD OF CANADA,
PACIFIC OCEANOGRAPHIC GROUP,
NANAIMO, BRITISH COLUMBIA.

A SPHERICAL WAVE EXPANSION FOR DOUBLE β-DECAY*

S. P. ROSEN

In a recent article in this journal, the spherical wave solutions of the Dirac equation for a central field and the properties of angular momentum coupling coefficients were used to derive a general formulation of the theory of single β-decay transitions of arbitrary forbiddenness (Lee-Whiting 1958). The theory of double β-decay can be formulated in a similar manner and it may be of interest to show briefly how this is done.

Consider the general nucleon–lepton interaction Hamiltonian:

$$(1)\quad H=\sum_x (\psi_p^+ O_x \psi_n)\{C_x[\psi_e^+ O_x(1+\delta_x\gamma_5)\psi_\nu]+D_x[\psi_e^+ O_x(1+\eta_x\gamma_5)\psi_{\bar\nu}]\}+\text{h.c.}$$

It has been shown (Primakoff 1952; Rosen 1957; Primakoff and Rosen 1959) that the matrix element $A(i\to f)$ for the neutrinoless double β-decay of the nucleus (A,Z) to the nucleus $(A,Z+2)$

(2)

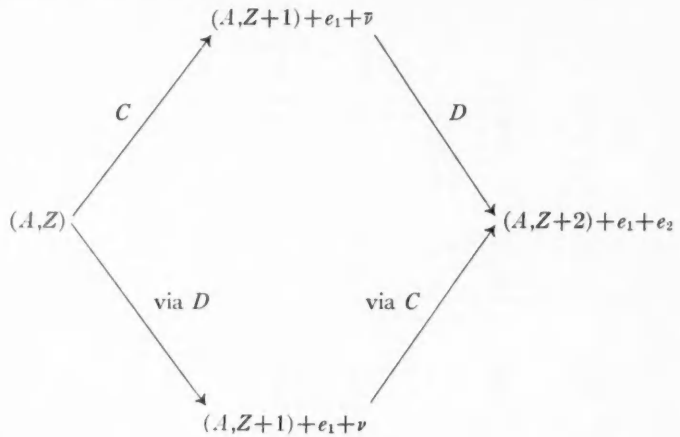

is given by

$$(3)\quad \left(\frac{2\pi}{mc}\right)^3\left(\frac{mc^2}{2\pi}\right)A(i\to f)$$

$$=(-\sqrt{3})^2\sum_{\lambda\nu} C^{01\ 1}_{\lambda,-\lambda}\,C^{01\ 1}_{\nu,-\nu}\int\Psi_f^+\Big\{\sum_{kj}\tau_k^+\tau_j^+ O_{k\lambda}O_{j\nu}$$

$$\times\Big[\psi_2^+(\mathbf{r}_k)O_{-\lambda}\Big[2i\left(\frac{\pi}{r_{kj}^3}-\frac{H_1+H_2}{r_{kj}^2}\right)\boldsymbol{\alpha}\cdot\mathbf{r}_{kj}+\frac{\pi(H_1-H_2)}{r_{kj}}\Big]$$

$$\times C(I_{\lambda\nu}+J_{\lambda\nu}\gamma_5)\tilde O_{-\nu}\psi_1^{\times}(\mathbf{r}_j)\Big]\Big\}\Psi_i d\tau$$

*This research was supported in part by the United States Air Force through the Air Force Office of Scientific Research and Development Command, under contract No. AF 18(603)-108.

where $mc^2 H_i$ $(i = 1, 2)$ are the electron energies and C is the charge conjugation operator. The forms used for the invariants O_x are

$$(4) \qquad \begin{aligned} O_S &= \beta, \qquad O_T = (\beta\boldsymbol{\delta}, \beta\boldsymbol{\alpha}), \qquad O_P = \beta\gamma_5, \\ O_V &= (1, i\boldsymbol{\alpha}), \qquad O_A = (\boldsymbol{\delta}, i\gamma_5) \end{aligned}$$

and the indices λ, ν of (3) refer to the spherical components of these operators.* If O_λ is a scalar-type operator (β, γ_5, 1, etc.), then there is only one term in the summation over λ, and the factor $(-\sqrt{3}C^{01\,1}_{\lambda,-\lambda})$ is replaced by unity; if O_λ is vector type ($\boldsymbol{\delta}$, $\boldsymbol{\alpha}$, etc.), then no such modifications are needed (similarly for O_ν). Also

$$(5) \qquad \begin{aligned} I_{\lambda\nu} &= C_\lambda D_\nu(1-\delta_\lambda\eta_\nu)+C_\nu D_\lambda(1-\delta_\nu\eta_\lambda), \\ J_{\lambda\nu} &= C_\lambda D_\nu(\delta_\lambda-\eta_\nu)+C_\nu D_\lambda(\delta_\nu-\eta_\lambda); \end{aligned}$$

Ψ_i, Ψ_f are the wave functions of the initial and final nuclei respectively; τ_k^+, τ_j^+ are the usual isotopic spin operators; $\mathbf{r}_k$, $\mathbf{r}_j$ are the position vectors of the k^{th}, j^{th} nucleons; and $\mathbf{r}_{kj} = \mathbf{r}_k - \mathbf{r}_j$.

The spherical wave function $\psi_i(\mathbf{r})$ for the i^{th} electron $(i = 1, 2)$ is written as (Spiers and Blin-Stoyle 1952)

$$(6) \qquad \psi_i(\mathbf{r}) = \psi^{m_i}_{j_i}(\mathbf{r}, \sigma_i, \beta_i) = C^{j_i l_i}_{m_i-\sigma_i,\sigma_i\,\frac{1}{2}} F^{\beta_i a_i}_{l_i}(pr)\; Y^{m_i-\sigma_i}_{l_i}(\theta, \phi) \qquad (\text{with } l_i = j_i + \tfrac{1}{2}a_i\beta_i),$$

corresponding to an electron with total angular momentum j_i, m_i and linear momentum p. Both parameters a_i, β_i take the values ± 1, and σ_i, which corresponds, in the non-relativistic limit, to the z-component of spin, is $\pm\frac{1}{2}$.

There are two types of operators acting on the nuclear states in (3):

$$(7i) \qquad O_{k\lambda}O_{j\nu}\{\bar{\psi}_2(\mathbf{r}_k)O^{\times}_{-\lambda}C[I_{\lambda\nu}+J_{\lambda\nu}\gamma_5]O^{+}_{-\nu}\psi_1(\mathbf{r}_j)\}^{\times},$$

$$(7ii) \qquad O_{k\lambda}O_{j\nu}\{\bar{\psi}_2(\mathbf{r}_k)O^{\times}_{-\lambda}\boldsymbol{\alpha}\,.\,\mathbf{r}_{kj}C[I_{\lambda\nu}+J_{\lambda\nu}\gamma_5]O^{+}_{-\nu}\psi_1(\mathbf{r}_j)\}^{\times}.$$

(Note that $\times$ means complex conjugate, $\sim$ transpose, and $+$ hermitian conjugate.) In both expressions (7), the wave functions (6) are used to form eigenfunctions of the total angular momentum J, M of the electron pair. The operators defined by

$$(8) \qquad \begin{aligned} E_{\lambda\nu} &= (O_{-\lambda}C[I_{\lambda\nu}+J_{\lambda\nu}\gamma_5]\tilde{O}_{-\nu}), \\ D_{\lambda\mu\nu} &= (O_{-\lambda}\alpha_{-\mu}C[I_{\lambda\nu}+J_{\lambda\nu}\gamma_5]\tilde{O}_{-\nu}) \end{aligned}$$

can be written as the outer products of two (2×2) matrices

$$(9) \qquad \begin{aligned} (E_{\lambda\nu}) &= (E_{\lambda\nu})^{\sigma_2\sigma_1}_{\beta_2\beta_1} = (E_{\lambda\nu})^{\sigma_2\sigma_1}\times(E_{\lambda\nu})_{\beta_2\beta_1}, \\ (D_{\lambda\mu\nu}) &= (D_{\lambda\mu\nu})^{\sigma_2\sigma_1}\times(D_{\lambda\mu\nu})_{\beta_2\beta_1} \end{aligned}$$

where each matrix acts on the variables indicated and both $(E_{\lambda\nu})_{\beta_2\beta_1}$, $(D_{\lambda\mu\nu})_{\beta_2\beta_1}$ are independent of $\lambda\mu\nu$ (see Spiers and Blin-Stoyle (1952*a*) for details).

*$A_1 = -\dfrac{1}{\sqrt{2}}(A_x + iA_y), \qquad A_0 = A_z, \qquad A_{-1} = \dfrac{1}{\sqrt{2}}(A_x - iA_y)$

$\mathbf{A}\,.\,\mathbf{B} = (-\sqrt{3})\sum_{\lambda} C^{01}_{\lambda,-\lambda}\,\frac{1}{\lambda}\,A_\lambda B_{-\lambda}.$

From (6), (8), and (9), the lepton factor of (7*i*) is equal to

$$(10)\quad \sum_{\substack{\beta_1\beta_2\\ \sigma_1\sigma_2\\ m_1+m_2=M}} C^{J}_{M\ m_1,m_2}{}^{j_1\ j_2}\, C^{j_1\ l_1}_{m_1-\sigma_1,\sigma_1}{}^{\ \ \frac{1}{2}}\, C^{j_2\ l_2}_{m_2-\sigma_2,\sigma_2}{}^{\ \ \frac{1}{2}}$$

$$\times[Y^{m_1-\sigma_1}_{l_1}(j)\ Y^{m_2-\sigma_2}_{l_2}(k)\ F^{\beta_1 a_1}_{l_1}(p_1 r_j)\ F^{\beta_2 a_2}_{l_2}(p_2 r_k)(E^{\times}_{\lambda\nu})^{\sigma_2\sigma_1}]^{\times}$$

where

$$l_i = j_i + \tfrac{1}{2}a_i\beta_i$$

and

$$Y^m_l(j) = Y^m_l(\theta_j, \phi_j).$$

By means of the relation (Spiers and Blin-Stoyle 1952*a*)

$$(11)\quad \sum_{m_1+m_2=M} C^{J\ j_1\ j_2}_{m_1,m_2}\, C^{j_1\ l_1}_{m_1-\sigma_1,\sigma_1}{}^{\ \ \frac{1}{2}}\, C^{j_2\ l_2}_{m_2-\sigma_2,\sigma_2}{}^{\ \ \frac{1}{2}}\, Y^{m_1-\sigma_1}_{l_1}(j)\ Y^{m_2-\sigma_2}_{l_2}(k)$$

$$= \sum_{LS} B^{l_1 l_2}_{j_1 j_2}(JLS)\, C^{J\ L\ \ \ S}_{(M-\sigma_1-\sigma_2),\sigma_1+\sigma_2\ \ \sigma_1\sigma_2}\, C^{S\ \frac{1}{2}\ \frac{1}{2}}\, \mathcal{Y}^{M-\sigma_1-\sigma_2}_{L:l_1 l_2}$$

and (10), the expression (7*i*) can now be written as

$$(12)\quad W^M_{(j_1a_1 j_2a_2)}(J) = \sum_{LS} W^M_{(j_1a_1 j_2a_2)}(JLS) = \sum_{LS}\Big\{\sum_{\beta_1\beta_2}[H^M_{(j_1a_1\beta_1 j_2a_2\beta_2)}(JLS)]^{\times}$$

$$\times K_{(j_1a_1\beta_1 j_2a_2\beta_2)}(JLS)\Big\}$$

where

$$(13)\quad H^M_{(j_1a_1\beta_1 j_2a_2\beta_2)}(JLS)$$

$$= \sum_{\substack{\sigma_1\sigma_2\\ \lambda\ \nu}} (-1)^{\lambda+\nu}(O_{k\lambda}O_{j\nu})^{\times}(E^{\times}_{\lambda\nu})^{\sigma_2\sigma_1}\, C^{J\ L\ \ \ S}_{(M-\sigma_1-\sigma_2),\sigma_1+\sigma_2\ \ \sigma_1\sigma_2}\, C^{S\ \frac{1}{2}\ \frac{1}{2}}\, \mathcal{Y}^{M-\sigma_1-\sigma_2}_{L:l_1 l_2},$$

$$(14)\quad K_{(j_1a_1\beta_1 j_2a_2\beta_2)}(JLS) = [B^{l_1 l_2}_{j_1 j_2}(JLS,\ F^{\beta_1 a_2}_{l_1}(p_1 r_j)\ F^{\beta_2 a_2}_{l_2}(p_2 r_k)(E^{\times}_{\lambda\nu})_{\beta_2\beta_1}]^{\times},$$

and (Blatt and Weisskopf 1952, Appendix A)

$$(15)\quad \mathcal{Y}^M_{L:l_1 l_2} = \sum_{m_1+m_2=M} C^{L\ l_1\ l_2}_{m_1\ m_2}\, Y^{m_1}_{l_1}(j)\ Y^{m_2}_{l_2}(k).$$

Now expand

$$(16)\quad (E_{\lambda\nu})^{\sigma_2\sigma_1} = \sum_T e^{\gamma}_T(\lambda\nu)(-1)^{\gamma} C^{T\ \ \frac{1}{2}\ \ \frac{1}{2}}_{-\gamma,\sigma_1,\sigma_2}(i\sqrt{2}).$$

For O_λ, O_ν scalar-type operators*

$$(17)\quad e^{\gamma}_T(\lambda\nu) = -\delta_{T,0}\delta_{\gamma,0}$$

and for O_λ, O_ν vector-type operators

$$(18)\quad e^{\gamma}_T(\lambda\nu) = (-1)^{1+\gamma}\sqrt{\frac{6}{2T+1}}\, C^{T\ 1\ 1}_{\gamma\ \lambda\ \nu}.$$

*All scalar-type operators have the same dependence on σ_1, σ_2; the differences between them are in their β_2, β_1 dependence. The same is true for vector-type operators.

Therefore, from (14), (16), (17), and (18),

$$(19)\qquad H^{M}_{(j_1a_1\beta_1 j_2a_2\beta_2)}(JLS) = i\sqrt{2}(O_kO_j)^{\times}\mathcal{Y}^{M}_{L:l_1l_2}\delta_{J,L}\delta_{S,0} \qquad \text{(scalar } O_\lambda,\ O_\nu\text{)}$$

and for vector-type O_λ, O_ν

$$= i(-1)^{L+S-J+M}\frac{2\sqrt{3}}{\sqrt{2S+1}}\left(\sum_{\lambda\nu\gamma} C^{J\ L}_{-(M+\gamma),\ \gamma}{}^{S}\, C^{S\ 1\ 1}_{\gamma\ \lambda\ \nu} O_{k\lambda}O_{j\nu}\,\mathcal{Y}^{-M-\gamma}_{L:l_1l_2}\right)^{\times}.$$

For the vector interaction ($O_k = O_j = 1$) and the axial vector ($O_k = O_j = \mathbf{\delta}$) (note that source velocity terms have been ignored),

$$(E_{\lambda\nu})_{\beta_2\beta_1} = -(\rho_\nu)_{\beta_2\beta_1}I_{\lambda\nu}.$$

In a similar way, the expression (7*ii*) can be written as

$$(20)\quad R^{M}_{(j_1a_1j_2a_2)}(J) = \sum_{PS} R^{M}_{(j_1a_1j_2a_2)}(JPS) = \sum_{PS}\left\{\sum_{\beta_1\beta_2}[T^{M}_{(j_1a_1\beta_1j_2a_2\beta_2)}(JPS)]^{\times} \times N_{(j_1a_1\beta_1j_2a_2\beta_2)}(JPS)\right\}$$

where

$$(21)\quad T^{M}_{(j_1a_1\beta_1j_2a_2\beta_2)}(JPS) = \sum_{\substack{\lambda\mu\nu\\ \sigma_1\sigma_2\\ hf}} (-1)^{1+\lambda+\mu+\nu}\sqrt{2f+1}\, C^{J\ 1\ f}_{\mu\ M-\mu}\, C^{f\ P}_{(M-\mu\ \ S}{}_{-\sigma_1-\sigma_2),\ \sigma_1+\sigma_2} \times C^{S\ \frac{1}{2}\ \frac{1}{2}}_{\sigma_1\ \sigma_2}(D^{\times}_{\lambda\mu\nu})^{\sigma_2\sigma_1}(O_{k\lambda}O_{j\nu})^{\times}$$

$$\times\left\{\sqrt{2l_2+1}\, C^{h\ l_2\ 1}_{0\ 0\ 0}\begin{bmatrix} j_2 & \frac{1}{2} & l_2 & h\\ j_1 & \frac{1}{2} & l_1 & f\\ J & S & 1 & P\end{bmatrix} r_k\,\mathcal{Y}^{M-\sigma_1-\sigma_2-\mu}_{P:l_1h}\right.$$

$$\left.+(-1)^{g}\sqrt{2l_1+1}\, C^{h\ l_1\ 1}_{0\ 0\ 0}\begin{bmatrix} j_1 & \frac{1}{2} & l_1 & h\\ j_2 & \frac{1}{2} & l_2 & f\\ J & S & 1 & P\end{bmatrix} r_j\,\mathcal{Y}^{M-\sigma_1-\sigma_2-\mu}_{P:hl_2}\right\}$$

$$(g = j_1+j_2+h+l_2+J+P+S)$$

and

$$(22)\quad N_{(j_1a_1\beta_1j_2a_2\beta_2)}(JPS) = [\sqrt{(2P+1)(2S+1)(2j_1+1)(2j_2+1)}\, F^{\beta_1a_1}_{l_1l}(p_1r_j)\, F^{\beta_2a_2}_{l_2l}(p_2r_k)\,(D^{\times}_{\lambda\mu\nu})_{\beta_2\beta_1}]^{\times}.$$

The 12-j symbol is defined in Jahn and Hope (1954). Expanding

$$(D_{\lambda\mu\nu})^{\sigma_2\sigma_1} = \sum_{T}(i\sqrt{2})d^{\gamma}_{T}(\lambda\mu\nu)(-1)^{\gamma}C^{T\ \frac{1}{2}\ \frac{1}{2}}_{-\gamma\ \sigma_1\ \sigma_2}$$

$$(23)\quad d^{\gamma}_{T}(\lambda\mu\nu) = i(-1)^{1+\gamma}\delta_{T,0}\delta_{\gamma,\mu} \qquad \text{(}O_\lambda,\ O_\nu\text{ scalar)}$$

$$= i(-1)^{\gamma}\sum_{G} D(T,G)C^{T\ 1\ G}_{\mu,\ \lambda+\nu}\, C^{G\ 1\ 1}_{\lambda\ \nu} \qquad \text{(}O_\lambda,\ O_\nu\text{ vector)}$$

where

$$D(1,G) = (1-G)\sqrt{\frac{2G+1}{3}}\,(\sqrt{2})^G$$
$$D(0,G) = -\sqrt{6}. \tag{24}$$

From (23) and (21)

$$T^M_{(j_1a_1\beta_1 j_2a_2\beta_2)}(JPS) = \sum_{f,h}(2f+1)\sqrt{\frac{2}{2P+1}}\,[Ar_k\,\mathcal{Y}^M_{P:l_1h}+Br_j\,\mathcal{Y}^M_{P:hl_2}] \times\delta_{S,1}\delta_{J,P}(O_kO_j)^{\times} \tag{25}$$
$$(O_\lambda, O_\nu \text{ scalar}).$$

(the coefficients A, B are as in equation (21))

$$= -\sqrt{6}\sum_{\substack{\lambda\nu\\ hfG}}(-1)^{M+S+P-J}(2f+1)\sqrt{(2S+1)}W(GSJf{:}1P)D(S,G) \times\{C^{J\ G\ P}_{\lambda+\nu,\ (-M-\lambda-\nu)}\,C^{G\ 1\ 1}_{\lambda\ \nu}\,O_{k\lambda}O_{j\nu}[Ar_k\,\mathcal{Y}^{-M-\lambda-\nu}_{P:l_1h}+Br_j\,\mathcal{Y}^{-M-\lambda-\nu}_{P:hl_2}]\}^{\times}$$
$$(O_\lambda, O_\nu \text{ vector}).$$

For vector and axial vector interactions

$$(D_{\lambda\mu\nu})_{\beta_2\beta_1} = (\rho_z)_{\beta_2\beta_1}I_{\lambda\nu}. \tag{26}$$

From equations (3), (7), (12), and (20) the operator appearing between Ψ_i and Ψ_f in the matrix element $A(i\to f)$ is

$$V = \sum_{kj}\tau_k^+\tau_j^+\,V^M_{(j_1a_1j_2a_2)}(J) \tag{27}$$

where

$$V^M_{(j_1a_1j_2a_2)}(J) = \sum_S V^M_{(j_1a_1j_2a_2)}(JS),$$

$$V^M_{(j_1a_1j_2a_2)}(JS) = \left[\frac{2\pi i}{r^3_{kj}}-\frac{2i(H_1+H_2)}{r^2_{kj}}\right]\sum_P R^M_{(j_1a_1j_2a_2)}(JPS) -\frac{\pi(H_1-H_2)}{r_{kj}}\sum_L W^M_{(j_1a_1j_2a_2)}(JLS). \tag{28}$$

The probability per unit time for neutrinoless double β-decay, accompanied by the emission of electrons with energies mc^2H_i $(i=1,2)$ is

$$P(H_1,H_2)dH_1dH_2 = \frac{1}{(2\pi)^5}\frac{mc^2}{2\hbar}\sum_{\substack{JM\\ j_1a_1j_2a_2}}|\int\Psi_f^+\,V\Psi_i d\tau|^2\frac{H_1}{p_1}\cdot\frac{H_2}{p_2}\delta(H_0-H_1-H_2) \times dH_1dH_2 \tag{29}$$

where $p_i^2 = H_i^2-1$ and mc^2H_0 is the energy released in the process.

The degree of forbiddenness is determined by the power of r_{kj} appearing in the denominator of V: the higher this power, the lower the degree of forbiddenness (Primakoff 1952). For low Z, the radial functions $F_l^{\beta a}(pr)$

behave roughly as $(pr)^l$ (where $l = j+\frac{1}{2}a\beta$). Therefore, from (20), (21), (22) and (12), (14) the following rules can be given to select terms with degree of forbiddenness f:

(i) for $\frac{1}{r_{kj}^n} R^M_{(j_1a_1j_2a_2)}(JPS)$ take $l_1+l_2 = f-3+n$;

(ii) for $\frac{1}{r_{kj}^m} W^M_{(j_1a_1j_2a_2)}(JLS)$ take $l_1+l_2 = f-2+m$.

In both (i) and (ii) if an operator α or γ_5 appears r times (e.g. $O_{k\lambda} = \alpha_\lambda$, $r = 1$) then f must be replaced by $(f-r)$. Notice that l_1, l_2 are always greater than, or equal to, zero.

$$T^M_{(j_1a_1j_2a_2)}(JPS) \quad \text{has factors} \quad C^{h\ l_2\ 1}_{0\ 0\ 0}\mathcal{Y}^M_{P:l_1h},\ C^{h'\ l_1\ 1}_{0\ 0\ 0}\mathcal{Y}^M_{P:h'\ l_2};$$

therefore, $h = l_2 \pm 1$, $h' = l_1 \pm 1$, and the parity is $(-1)^{l_1+l_2+1}$. Similarly the parity of $H^M_{(j_1a_1j_2a_2)}(JLS)$ is $(-1)^{l_1+l_2}$. Therefore the parity selection rules are:

for (i) the parity change is $(-1)^{f+n}$,

for (ii) the parity change is $(-1)^{f+m}$.

If α, γ_5 appear r times, f is replaced by $(f-r)$.

The values of J, M are determined by the total angular momenta (J_i, M_i), (J_f, M_f) of the initial and final nuclei.

The matrix element for two neutrino double β-decay has also been considered from this point of view, but, since there are now four leptons involved, it seems too complicated to study in detail.

Most of the above work is taken from chapter three of S. P. Rosen (1957). The author would like to thank Dr. R. J. Blin-Stoyle of the Clarendon Laboratory, Oxford, for suggesting this problem and the Department of Scientific and Industrial Research of Great Britain for a maintenance grant.

BLATT, J. M. and WEISSKOPF, V. F. 1952. Theoretical nuclear physics (John Wiley & Sons, Inc., New York).
JAHN, J. A. and HOPE, J. 1954. Phys. Rev. **93**, 318.
LEE-WHITING, G. E. 1958. Can. J. Phys. **36**, 1199.
PRIMAKOFF, H. 1952. Phys. Rev. **85**, 888.
PRIMAKOFF, H. and ROSEN, S. P. 1959. Reports on Progr. in Phys. **22** (in press).
ROSEN, S. P. 1957. Ph. D. Thesis, Oxford (unpublished).
SPIERS, J. A. and BLIN-STOYLE, R. J. 1952*a*. Proc. Phys. Soc. A, **65**, 801.
——— 1952*b*. Proc. Phys. Soc. A, **65**, 809.

RECEIVED JANUARY 26, 1959.
DEPARTMENT OF PHYSICS,
WASHINGTON UNIVERSITY,
SAINT LOUIS 5, MISSOURI.

NOTES TO CONTRIBUTORS

Canadian Journal of Physics

MANUSCRIPTS

General.—Manuscripts, in English or French, should be typewritten, double spaced, on paper 8½×11 in. **The original and one copy are to be submitted.** Tables and captions for the figures should be placed at the end of the manuscript. Every sheet of the manuscript should be numbered. Style, arrangement, spelling, and abbreviations should conform to the usage of recent numbers of this journal. Greek letters or unusual signs should be written plainly or explained by marginal notes. Characters to be set in boldface type should be indicated by a wavy line below each character. Superscripts and subscripts must be legible and carefully placed. Manuscripts and illustrations should be carefully checked before they are submitted. Authors will be charged for unnecessary deviations from the usual format and for changes made in the proof that are considered excessive or unnecessary.

Abstract.—An abstract of not more than about 200 words, indicating the scope of the work and the principal findings, is required, except in Notes.

References.—References should be listed **alphabetically by authors' names,** unnumbered, and typed after the text. The form of the citations should be that used in current issues of this journal; in references to papers in periodicals, titles should not be given and only initial page numbers are required. The names of periodicals should be abbreviated in the form given in the most recent *List of Periodicals Abstracted by Chemical Abstracts.* All citations should be checked with the original articles and each one referred to in the text by the authors' names and the year.

Tables.—Tables should be numbered in roman numerals and each table referred to in the text. Titles should always be given but should be brief; column headings should be brief and descriptive matter in the tables confined to a minimum. Vertical rules should not be used. Numerous small tables should be avoided.

ILLUSTRATIONS

General.—All figures (including each figure of the plates) should be numbered consecutively from 1 up, in arabic numerals, and each figure referred to in the text. The author's name, title of the paper, and figure number should be written in the lower left corner of the sheets on which the illustrations appear. Captions should not be written on the illustrations.

Line drawings.—Drawings should be carefully made with India ink on white drawing paper, blue tracing linen, or co-ordinate paper ruled in blue only; any co-ordinate lines that are to appear in the reproduction should be ruled in black ink. Paper ruled in green, yellow, or red should not be used. All lines must be of sufficient thickness to reproduce well. Decimal points, periods, and stippled dots must be solid black circles large enough to be reduced if necessary. Letters and numerals should be neatly made, preferably with a stencil (**do NOT use typewriting**) and be of such size that the smallest lettering will be not less than 1 mm high when the figure is reduced to a suitable size. Many drawings are made too large; originals should not be more than 2 or 3 times the size of the desired reproduction. Whenever possible two or more drawings should be grouped to reduce the number of cuts required. In such groups of drawings, or in large drawings, full use of the space available should be made; the ratio of height to width should conform to that of a journal page (4¾×7½ in.), but allowance must be made for the captions. **The original drawings and one set of clear copies (e.g. small photographs) are to be submitted.**

Photographs.—Prints should be made on glossy paper, with strong contrasts. They should be trimmed so that essential features only are shown and mounted carefully, with rubber cement, on white cardboard, with no space between those arranged in groups. In mounting, full use of the space available should be made. **Photographs are to be submitted in duplicate;** if they are to be reproduced in groups one set should be mounted, the duplicate set unmounted.

REPRINTS

A total of 50 reprints of each paper, without covers, are supplied free. Additional reprints, with or without covers, may be purchased at the time of publication.

Charges for reprints are based on the number of printed pages, which may be calculated approximately by multiplying by 0.6 the number of manuscript pages (double-spaced typewritten sheets, 8½×11 in.) and including the space occupied by illustrations. Prices and instructions for ordering reprints are sent out with the galley proof.

Contents

K. G. McNeill and R. M. Green—Measurements with a whole body counter 683

A. Kavadas and D. G. Glass—Polarization of radar echoes from aurora - - 690

S. C. Loh—The calculation of the electric potential and the capacity of a tore by means of toroidal functions - - - - - - - - - - - - 698

J. M. Dowling and B. P. Stoicheff—High resolution Raman spectroscopy of gases. XII. Rotational spectra of C_2H_4 and C_2D_4 and the structure of the ethylene molecule - - - - - - - - - - - - - - - - 703

J. P. Roalsvig, R. N. H. Haslam, L. D. Skarsgard, and E. E. Wuschke—Photo alpha reactions in silver - - - - - - - - - - - - - - 722

R. E. Burgess—Statistical theory of avalanche breakdown in silicon - - - 730

J. S. Kirkaldy—Crystal growth and thermodynamics of irreversible processes 739

W. J. King and M. W. Johns—Spins of excited states of Os^{188} - - - - - 755

Notes:

Charlotte Froese—On the calculation of the velocity of sound in sea water - 775

S. P. Rosen—A spherical wave expansion for double β-decay - - - - 780

Printed in Canada *by* University of Toronto Press